Imperial College London

PhD Thesis

Imperial College London

Department of Materials

Modelling electronic, magnetic, and optical properties of graphene nanoribbons

Nikita Tepliakov

December 13, 2024

Statement of Originality

This is to certify that this copy of my thesis, which is in partial fulfillment for the PhD degree at Imperial College London and has not been submitted for any other degree or professional qualification, embodies the results of my own course of research and has been composed by myself.

Copyright Declaration

The copyright of this thesis rests with the author. Unless otherwise indicated, its contents are licensed under a Creative Commons Attribution-Non Commercial 4.0 International Licence (CC BY-NC).

Under this licence, you may copy and redistribute the material in any medium or format. You may also create and distribute modified versions of the work. This is on the condition that: you credit the author and do not use it, or any derivative works, for a commercial purpose.

When reusing or sharing this work, ensure you make the licence terms clear to others by naming the licence and linking to the licence text. Where a work has been adapted, you should indicate that the work has been changed and describe those changes.

Please seek permission from the copyright holder for uses of this work that are not included in this licence or permitted under UK Copyright Law.

Abstract

Graphene nanoribbons—narrow strips of sp^2-bonded carbon atoms—are considered highly promising candidates for post-silicon electronics due to their diverse electronic properties. In this Thesis, I present a series of studies aimed at both elucidating established electronic properties of graphene nanoribbons and exploring novel ways to engineer new functionalities in these nanostructures. Specifically, I demonstrate that the semiconducting nature of armchair-edged graphene nanoribbons is governed by a hidden symmetry intrinsic to their crystal structure at certain widths. Furthermore, I show that the application of a transverse electric field to armchair-edged graphene nanoribbons induces a semiconductor-to-semimetal transition, leading to the emergence of Dirac points at the Fermi level. Next, I investigate the electronic properties of zigzag-edged graphene nanoribbons embedded in hexagonal boron nitride, revealing that these heterojunctions exhibit half-semimetallic behavior: they conduct for electrons of one spin while remaining insulating for electrons of the opposite spin. Finally, I explore the electronic and optical properties of graphene nanostrips with Möbius geometry, showing that these nanostructures are chiral and feature strong optical activity. Overall, the findings presented in this Thesis provide new insights into graphene nanoribbons and lay the foundation for their future applications in nanoelectronics, spintronics, and photonics.

Acknowledgements

I am deeply grateful to Arash Mostofi and Johannes Lischner for the immense support they have shown me on this journey as my supervisors. As a part of their research group, I was afforded great intellectual freedom to explore a wide range of ideas, enjoyed honest and valuable feedback, participated in fantastic discussions with the other group members, and engaged in several interdisciplinary collaborations. I feel incredibly fortunate to have worked alongside Michele Pizzochero, whose deep expertise, passion for research, and mentorship have been instrumental in shaping this work. I admire his remarkable ability to generate truly unique and innovative ideas that have often led to pivotal breakthroughs in our research. I am greatly thankful to Ivan Rukhlenko and Oleg Yazyev for shaping me as a researcher with their exceptional supervision during my bachelor's and master's degrees. Among my amazing colleagues, I want to especially thank Kemal Atalar for creating an inclusive environment in our team, Simão João for introducing me to *pastéis de nata*, Chengcheng Xiao for fueling my caffeine addiction, Jordan Edwards for saving me from wails of despair in tough times and keeping my mood up, Christopher Cheung for teaching me how to keep my eyes wide open to new possibilities, Christopher Keegan for sharing his unique perspectives and helping me explore a totally different world, and Indrajit Maity for being a bright spot in our group. It is necessary to mention an incredible officemate Lorna Barron, who I shared many coffees and sweets with and whose presence in the office was always like a breath of fresh air. I am eternally grateful to my family for their love and support and to my friends for helping me deal with the challenges on this path. Special thanks go to my friend Denis Prokopenko for his unwavering support during our parallel PhD journeys. Last but not least, I was only able to pursue this research thanks to the President's PhD Scholarship of Imperial College London.

Contents

1 Introduction to graphene nanoribbons **9**

1.1 Rise of graphene nanoribbons 9

1.1.1 Electronic properties of graphene 9

1.1.2 Electronic and magnetic properties of graphene nanoribbons 12

1.1.3 Fabrication of graphene nanoribbons 16

1.2 Modifying properties of graphene nanoribbons 19

1.2.1 Electric field control of electronic properties 19

1.2.2 Integration with hexagonal boron nitride 23

1.3 Optical properties of graphene nanoribbons 29

1.3.1 Linear absorption and emission 29

1.3.2 Chiral graphene nanostructures 31

1.4 Conclusions 37

2 Computational methods **38**

2.1 Many-body Schrödinger equation 38

2.2 Density functional theory 41

2.2.1 Hohenberg-Kohn theorem 41

2.2.2 Kohn-Sham equations 44

2.3 Solving the Kohn-Sham equations 47

2.3.1 Self-consistent calculations 47

2.3.2 Exchange-correlation functionals . . . 48
2.3.3 Frozen core approximation and pseudopotentials . . . 49
2.3.4 Planewave basis set . . . 50
2.3.5 Spin-polarised calculations . . . 52
2.3.6 External electric fields . . . 53
2.4 Tight-binding approximation . . . 54
2.4.1 Localised basis set . . . 54
2.4.2 Tight-binding Hamiltonian . . . 56
2.4.3 Solving the tight-binding Hamiltonian . . . 58
2.4.4 Mean-field Hubbard model . . . 59

3 Hidden symmetries in graphene nanoribbons 62

3.1 Graphene nanoribbons with armchair edges . . . 63
3.1.1 *Ab initio* parametrized tight binding model . . . 63
3.1.2 Energy gaps of $n=3p+2$ graphene nanoribbons . . . 65
3.1.3 Robustness of semimetallic phase in graphene . . . 68
3.2 Origin of energy gaps in graphene nanoribbons . . . 69
3.2.1 Isomorphic transformation of graphene nanoribbons . . . 69
3.2.2 Hidden symmetry of rectangular quantum box . . . 72
3.2.3 Wave functions of degenerate states . . . 73
3.3 Strain engineering of armchair graphene nanoribbons . . . 76
3.3.1 Energy gap tuning and Dirac semimetallicity . . . 76
3.3.2 Topological phase transitions and end states . . . 78
3.4 Conclusions . . . 80

4 Graphene nanoribbons in an electric field 81

4.1 Electric route to Dirac fermions . . . 82

4.2 Role of width and chemical composition 86
4.3 Chemical route to Dirac fermions 90
4.4 Conclusions 92

5 Graphene nanoribbon/hexagonal boron nitride heterojunctions 93

5.1 Electronic structure of ZGNR/hBN heterojunctions 94
5.2 Origin of half-semimetallicity in ZGNR/hBN heterojunctions 99
5.3 Mean-field Hubbard model 101
5.4 Doping of ZGNR/hBN heterojunctions 107
5.5 Conclusions 108

6 Möbius graphene nanostrips for chiral nanophotonics 110

6.1 Electronic properties of Möbius graphene nanostrips 111
6.1.1 Coordinate transformation method 111
6.1.2 Topological properties of Möbius nanostrips 113
6.2 Optical properties of Möbius graphene nanostrips 114
6.2.1 Measures of optical activity 114
6.2.2 Transition matrix elements 115
6.2.3 Relative strength of optical activity 119
6.2.4 Optical spectra 120
6.3 Conclusions 124

Summary and Outlook 125

Chapter 1

Introduction to graphene nanoribbons

1.1 Rise of graphene nanoribbons

1.1.1 Electronic properties of graphene

Graphene — a single layer of carbon atoms arranged in a hexagonal crystal lattice — was studied theoretically long before its discovery by Geim and Novoselov in 2004 [1, 2]. In 1947, Wallace calculated electronic properties of graphite using the tight binding approximation [3]. Wallace discovered that a single layer of hexagonally packed C atoms serves as a zero-gap semiconductor in a sense that it does not have an energy gap, but requires electrons to be promoted to the conduction band in order to achieve conducting properties. It was revealed that graphite layers have exceptional conductivity in the in-plane direction, several orders of magnitude greater than the conductivity in the direction perpendicular to the stacked graphite layers.

Later theoretical works brought this discovery to the form that is much better known nowadays. In a seminal study that combined the tight-binding approximation with the first-principles calculations, the band structure of monolayer graphene shown in Fig. 1.1 was obtained [4]. The most striking feature observed in this band dispersion is the presence of a band crossing at the Fermi level of graphene. Low energy electrons and holes in graphene have a linear energy dispersion with momentum, thus behaving similar to relativistic particles. The motion of electrons in graphene is indeed described by the Dirac equation and the band crossing is called a Dirac point. However, the velocity of the charge carriers in

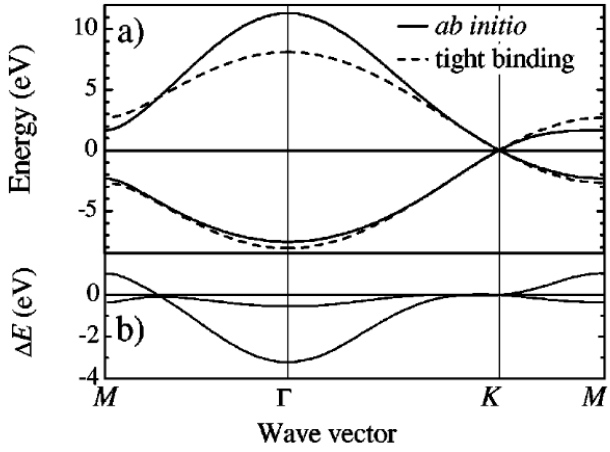


Figure 1.1: (a) Ab initio and nearest-neighbour tight-binding band structures of monolayer graphene. (b) Difference ΔE between the ab initio and tight-binding band structures. Reprinted with permission from *Phys. Rev. B* **66**, 035412 (2002) [4]. Copyright 2002 American Physical Society.

graphene, $v_{\mathrm{F}} = 10^6$ m/s, is two orders of magnitude lower than the actual speed of light. Another remarkable observation in Figure 1.1 is an exceptional match between the ab initio and tight-binding results in the region of energies around the Fermi level of graphene. This property makes the simple tight-binding approximation, which accounts only for the interactions between the nearest neighbours in the hexagonal crystal lattice of graphene, instrumental for studying the low-energy physics in graphene and graphene nanostructures.

These theoretical advances sparked a clear interest in the experimental fabrication of graphene. In the first confirmed successful attempt, Geim and Novoselov used mechanical exfoliation (repeated peeling) to reduce graphite to atomically-thin films of first multilayer and then monolayer graphene [1, 2]. The experimental characterization of monolayer graphene revealed a range of unique electronic properties stemming from the quasi-relativistic behaviour of charge carriers in graphene. It was found that graphene's conductivity never falls below a minimum value that corresponds to the quantum unit of conductance, $\sigma = 2e^2/h$, even when the concentration of charge carriers tends to zero.

The integer quantum Hall effect in graphene was found to be anomalous — the plateaus of conductivity were observed at half-integer filling factors, $\sigma_{xy} = 2\sigma_0(N + 1/2)$, where N is an integer, instead of expected integer filling factors, $\sigma_{xy} = 2\sigma_0 N$. Both scenarios are shown in Fig. 1.2. This anomalous nature of the quantum Hall effect was attributed to the presence of both electron-like and hole-like states at the Fermi level of graphene, which stems from

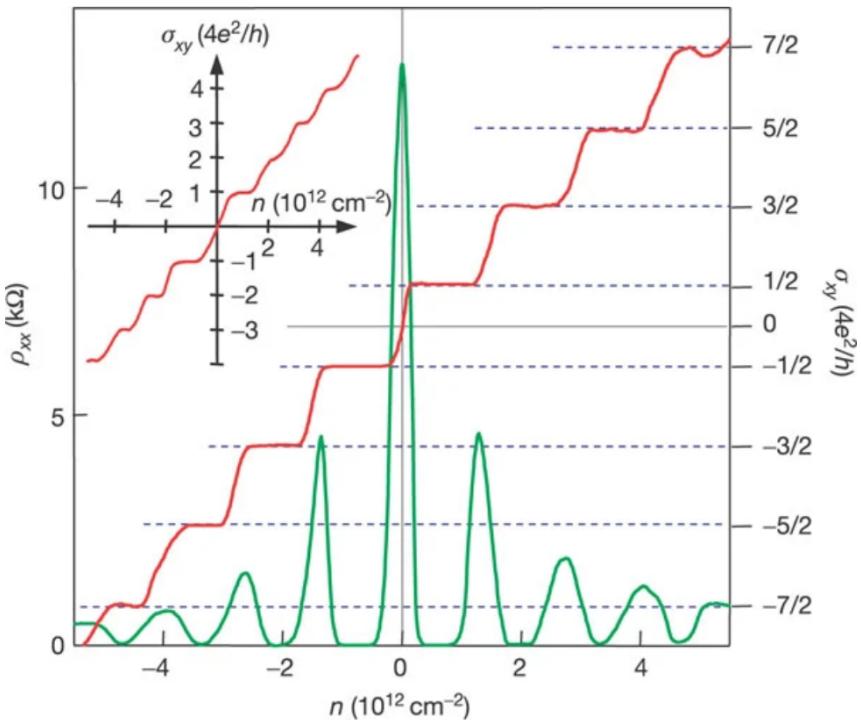


Figure 1.2: Hall conductivity σ_{xy} and longitudinal resistivity ρ_{xx} of graphene as a function of the charge carrier concentration at $B = 14$ T and $T = 4$ K. Inset shows σ_{xy} in two-layer graphene, in which the quantization sequence is normal and occurs at integer filling factors ν. The latter shows that the half-integer quantum Hall effect is exclusive to monolayer graphene. Reprinted with permission from *Nature* **438**, 197–200 (2005) [2]. Copyright 2005 Springer Nature.

the massless Dirac nature of the charge carriers in this material. These observations highlight monolayer graphene as a unique system for studying relativistic physics without relying on high energies.

Excellent mechanical stability, atomic flatness, and high carrier mobility in the in-plane direction make graphene a highly attractive material base for electronic devices, particularly as a replacement of silicon in field effect transistors [5]. Conventional logic devices, however, rely on the ability to turn the electric current through a material on and off, whereas graphene always has non-zero conductance due to the unique quasi-relativistic properties of Dirac fermions. It is therefore desirable to find a way to induce an energy gap in graphene while maintaining its excellent electronic properties. It was shown previously that monolayer graphene acquires an energy gap when placed on a substrate of hexagonal boron nitride [6], whereas an energy gap in bilayer graphene can be induced by applying a potential difference between the two layers [7]. A totally different approach relies on reducing graphene to vari-

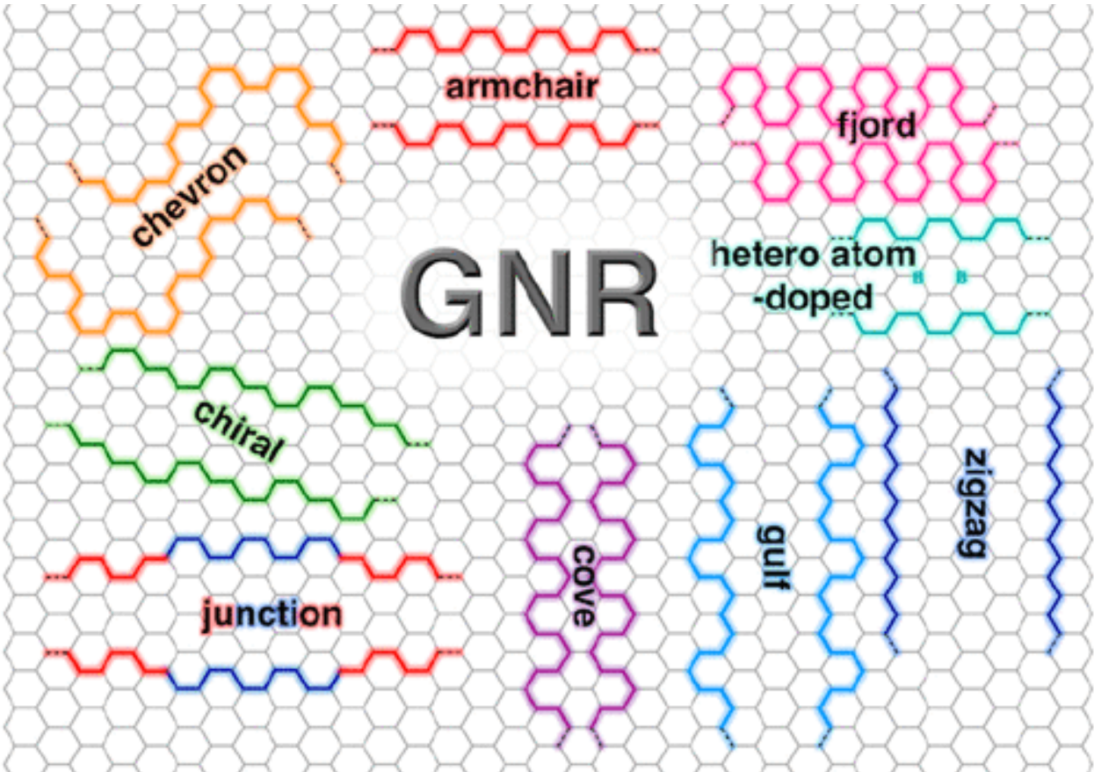


Figure 1.3: Different edge geometries in graphene nanoribbons. Reprinted with permission from *J. Org. Chem.* **85**, 4–33 (2019) [8]. Copyright 2019 American Chemical Society.

ous nanostructures of lower dimensionality, in which the quantum confinement of the charge carriers contributes to opening of an energy gap.

1.1.2 Electronic and magnetic properties of graphene nanoribbons

Graphene nanoribbons (GNRs) are narrow one-dimensional strips of graphene, typically with widths ranging from just a few atoms to tens of nanometers and lengths extending up to micrometers. Quantum confinement of the charge carriers in the transverse direction of GNRs generally leads to an energy gap, whose size depends on the width of the nanoribbon. The electronic properties of GNRs are also known to be largely dependent on the geometry of their edges, which exist in a huge variety [8], as shown in Fig. 1.3. The two most basic types of graphene nanoribbons are armchair-edged GNRs (AGNRs) and zigzag-edged GNRs (ZGNRs), which are both obtained by cutting uniform strips in the two different periodicity directions of monolayer graphene.

The earliest theoretical works on the topic of GNRs precede the experimental discovery of

graphene itself. In their seminal papers, Fujita et al. studied graphene nanoribbons (which they called 'graphite ribbons') with armchair and zigzag edges [9, 10]. Their study relied on the tight-binding approximation for π-electrons, which had earlier proven useful for monolayer graphene (see Fig. 1.1). It was found that AGNRs are semiconducting, and their energy gaps are exactly at the Γ point of the Brillouin zone. In sharp contrast, ZGNRs were found to be metallic. Their valence and conduction bands are degenerate at $|k| = \pi/a$, regardless of the nanoribbon width. As the size of the nanoribbon increases, the energy bands around the Fermi level become flatter, within $2\pi/3a \leq |k| \leq \pi/a$.

After the experimental discovery of graphene in 2004, computational studies of graphene nanoribbons regained their popularity. Studies relying on the Dirac equation and the simplest tight-binding approximation for graphene analysed the dependence of the energy gaps of graphene nanoribbons, both AGNRs and ZGNRs, on their width [11, 12]. It was observed that AGNRs feature a highly unusual bandgap dependence on their width. It was predicted that AGNRs with $n = 3p$ and $n = 3p+1$ atoms across their unit cell, where p is an integer, are semiconductors, whereas AGNRs with $n = 3p + 2$ atoms across the unit cell are semimetals, featuring a Dirac point just like monolayer graphene, as shown in Fig. 1.4. ZGNRs, on the other hand, were predicted to be metals with zero-energy states localised at the edges.

The presence of flat bands at the Fermi level in ZGNRs creates an instability that should result in either spontaneous magnetisation or the lattice distortion due to electron-phonon interactions. Fujita et al. used the tight-binding model with the so-called U-term, which describes electron-electron repulsion, to show that due to this instability the edges of ZGNRs become magnetised [9]. The magnetic moments at the two edges are equal in magnitude and opposite in sign. This magnetic phase is called an antiferromagnet, as opposed to ferromagnets which have non-zero magnetic moments on average. It was demonstrated that this antiferromagnetic ordering of magnetic moments can be observed in graphene nanoribbons with mixed armchair/zigzag edges, given that the ratio of zigzag elements is larger than a certain critical value, dependent on the overall width of the ribbon.

Further studies analysed the effect of the nearest-neighbour Coulomb interaction (the so-called V-term) on the electronic properties of ZGNRs [13]. While inclusion of the U-term only gives rise to the spin-polarised state, in which the edges of the nanoribbon have opposite magnetization, the interplay between the U and V terms can give rise to the charge-polarised

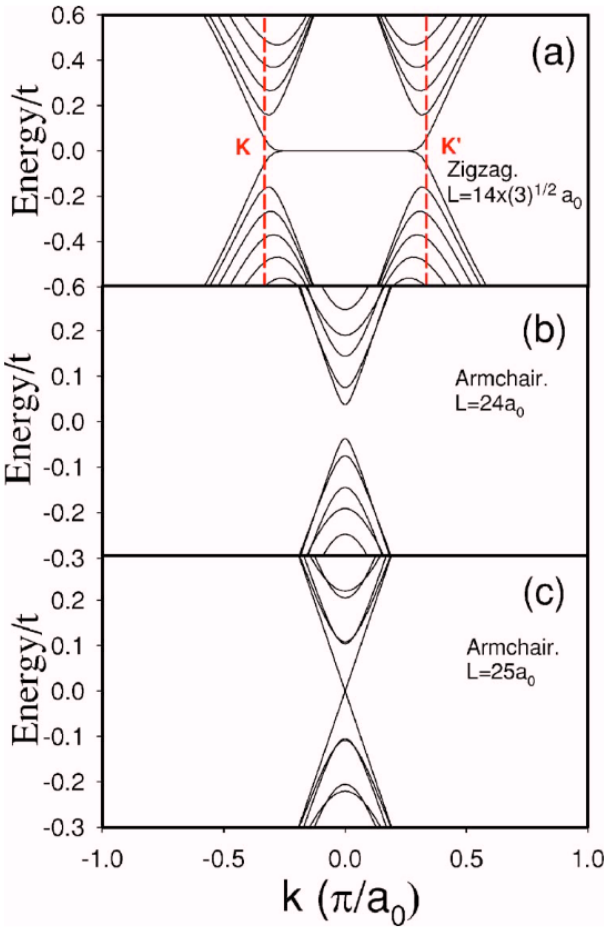


Figure 1.4: Energy bands of (a) ZGNR, (b) semiconducting AGNR, and (c) metallic AGNR. Reprinted with permission from *Phys. Rev. B* **73**, 235411 (2006) [11]. Copyright 2006 American Physical Society.

state. In this state, the edges of the nanoribbon have opposite charges, so there is a constant dipole moment aligned across the nanoribbon. If V is small compared to U, which is the case for graphene nanoribbons, then the spin-polarised state is lower in energy than the charge-polarised state. However, the application of an external electric field across the nanoribbon can stabilise the charge-polarised state. In strong electric fields, ZGNRs are thus expected to lose their magnetic properties.

In a subsequent computational study, Son et al. used first principles calculations and tight-binding modelling to calculate the energy gaps of graphene nanoribbons, obtaining a completely different result from the previous studies [14]. They found that all graphene nanoribbons, both AGNRs and ZGNRs, are semiconductors regardless of their width. In the case of $n = 3p + 2$ AGNRs, the energy gap is predicted to be zero only at the simplest possible

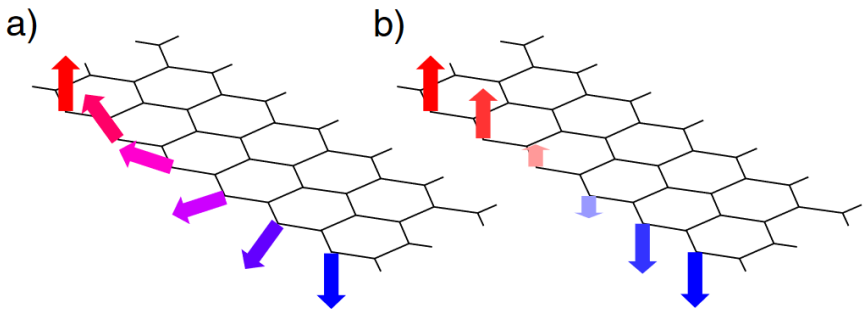


Figure 1.5: (a) Transverse and (b) longitudinal spin fluctuations at zigzag graphene edges. Reprinted with permission from *Phys. Rev. Lett* **100**, 047209 (2008) [16]. Copyright 2008 American Physical Society.

level of theory. Inclusion of the long-range hopping interactions or the edge effects in the tight binding model Hamiltonian for $n = 3p + 2$ AGNRs reproduces the energy gaps of these nanoribbons observed in the first-principles calculations. The origins of this behaviour have remained unclear since this original study. In Chapter 3 of this thesis, I reveal that the energy gap opening in $n = 3p+2$ AGNRs stems from the breaking of a previously unidentified hidden symmetry, inherent to these nanoribbons.

Son et al. also showed that all ZGNRs are semiconducting, as, similar to the previous predictions [9], the electron-electron interaction between the localised edge states drives a transition to an antiferromagnetic phase. A subsequent study relying on the tight binding modelling analysed the effect of charge doping on the magnetic state of ZGNRs [15]. It was revealed that the excess charge can drive a transition to a ferromagnetic phase, in which the spins at the two edges of the nanoribbon are aligned parallel to each other. In addition to that, the distribution of charge across the nanoribbon becomes asymmetric due to the symmetry breaking.

While the theory predicts that the edges of ZGNRs are spin-polarised, in practice such polarisation can be significantly weakened by finite-temperature fluctuations. Yazyev et al. used first-principles calculations to analyse magnetic correlations in zigzag graphene edges [16]. They considered the energetics of transverse and longitudinal spin fluctuations, shown in Fig. 1.5, revealing that at room temperatures, the characteristic length of magnetic ordering in zigzag graphene edges equal approximately 1 nm, which is insufficient for practical applications of magnetism in ZGNRs. They also proposed several approaches to enhance the magnetic anisotropy of graphene edges, which can potentially increase the range of magnetic

correlations in ZGNRs.

Some graphene nanoribbons have also been shown to possess non-trivial topological properties [17]. In particular, AGNRs with n atoms across their unit cell are topologically trivial if n is even and topologically non-trivial if n is odd. In the latter case, AGNRs, as 1D topological insulators, feature topologically protected 0D end states, which are localised at the two ends of a nanoribbon [18]. In Chapter 3, I reveal the formation of such topologically protected states in graphene nanoribbons exposed to tensile strain.

1.1.3 Fabrication of graphene nanoribbons

Graphene nanoribbons can be fabricated using either top-down approaches, that rely on reducing a larger material, usually monolayer graphene, to GNRs, or bottom-up methods that grow graphene nanoribbons from smaller precursors. On average, top-down approaches are characterised by the relative ease of fabrication of large quantities of GNRs, whereas the bottom-up methods allow more precise control over the shape and the edge geometry of the produced nanoribbons. The first experimental realisation of graphene nanoribbons was achieved in 2007 by Han et al., who used lithographic patterning [19]. In this top-down fabrication method, a graphene monolayer is first obtained via mechanical exfoliation and placed on a Si substrate. Graphene is then partially covered by a protective etch mask to define graphene nanoribbons of width 10–100 nm, and the unprotected parts of the monolayer are removed by exposure to an oxygen plasma. The electronic structure measurements performed on the fabricated GNRs confirmed the strong dependence of their band gap on the width of the nanoribbon.

The key problem with the above approach is the roughness of the edges of the obtained nanoribbons. In order to mediate this, Li et al. developed another top-down approach based on chemical cutting to produce GNRs of sub-10 nm widths and with smooth edges [20]. In their method, graphite is first exfoliated at high temperatures and then dispersed in a supernatant solution that is subsequently treated via sonication. This process results in a variety of differently shaped graphene fragments, some of which were identified as GNRs by atomic force microscopy. Experimental characterisation of the fabricated nanoribbons revealed that all obtained GNRs are semiconductors, which makes them clearly distinct from carbon nanotubes, some of which are metallic.

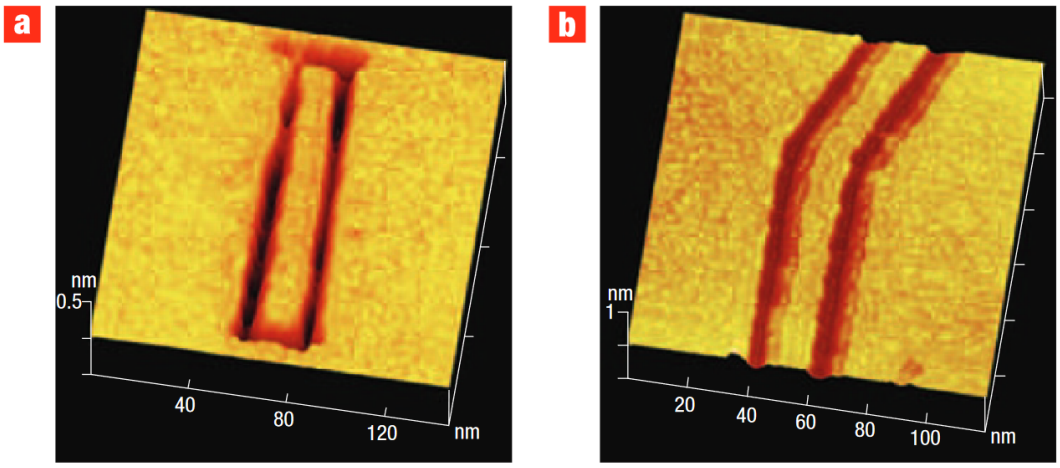


Figure 1.6: Graphene nanoribbons obtained via scanning tunneling microscopy (STM) lithography. (a) A 3D STM image of a 10-nm-wide and 120-nm-long graphene nanoribbon. (b) An 8-nm-wide 30° GNR bent junction connecting an armchair and a zigzag ribbon. Reprinted with permission from *Nature Nanotech.* **3**, 397–401 (2008) [21]. Copyright 2008 Springer Nature.

Another top-down fabrication method was reported by Tapasztó et al. who adapted scatting tunnelling microscopy (STM) to this end [21]. While STM is normally used for imaging purposes, application of high bias voltages can significantly modify the surface of the material being probed. STM lithography can thus be used to etch GNRs of any desired geometry from a graphene monolayer with atomic precision. As shown in Figure 1.6, this approach allows fabrication of both straight GNRs and bent junctions that combine armchair- and zigzag-edged GNRs in the same structure. The lateral dimensions of GNRs fabricated via STM lithography are in the sub-10 nm range, resulting in their relatively large band gaps compared to wider GNRs obtained from lithographic patterning and chemical cutting. This is a clear advantage of this method, since narrow GNRs with wider energy gaps are better suited for applications in field effect transistors [22]. A natural drawback of STM lithography is that it is not possible to produce large quantities of GNRs with method.

In another top-down fabrication method, GNRs are obtained by unzipping carbon nanotubes [23, 24]. In one of the first reported experimental works, multiwalled carbon nanotubes are covered with a protective mask, that leaves only a narrow strip on the outer surface of a nanotube exposed [24]. The subsequent plasma etching cuts through this longitudinal strip, resulting in a single-layer or even multilayer graphene nanoribbon folded around the inner carbon nanotube. The nanoribbon can then be unfolded and transferred

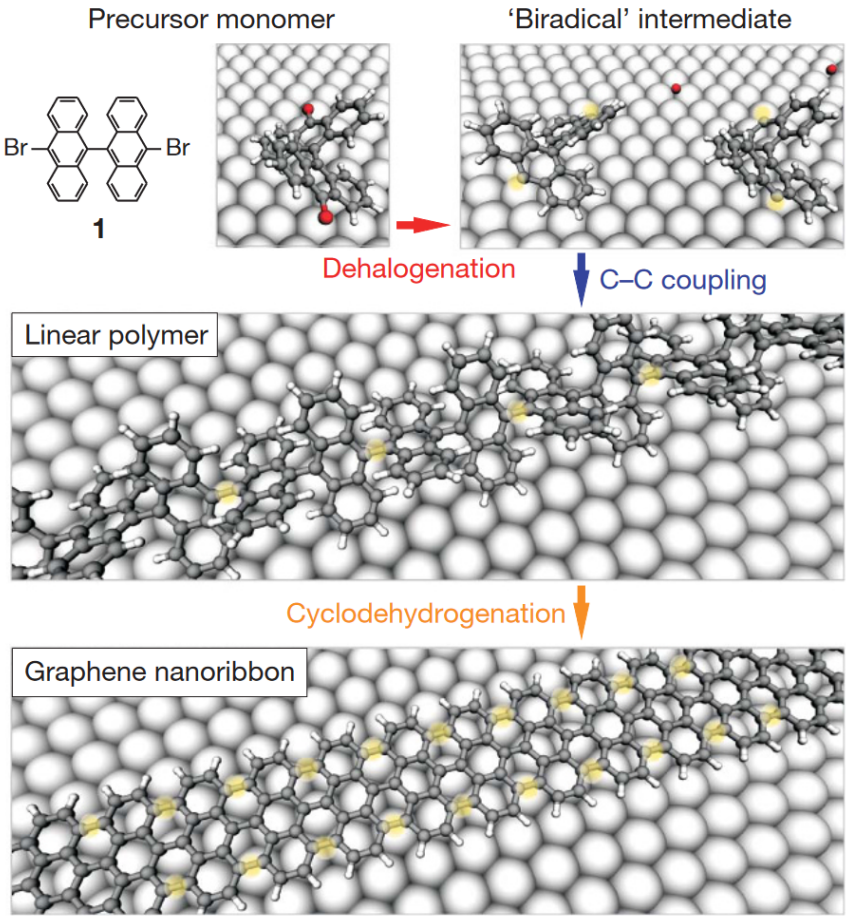


Figure 1.7: Illustration of basic steps for surface-supported GNR synthesis, using the example of 10,10'-dibromo-9,9'-bianthryl monomers as precursors. Grey, white, and red spheres correspond to C, H, and Br atoms. Reprinted with permission from *Nature* **466**, 470–473 (2010) [25]. Copyright 2010 Springer Nature.

to a Si substrate. Another approach relies on the oxidation of alkenes to first form a hole or a tear inside a wall of a carbon nanotube, which grows in size upon further exposure to the oxidising agent, until the nanotube opens into a nanoribbon [23]. Fabrication of GNRs via unzipping requires access to high-quality carbon nanotubes, but this method is capable of producing large quantities of uniform GNRs with well defined edges.

In 2010, Cai et al. published their seminal study with the first bottom-up fabrication of GNRs [25]. In this approach, GNRs are built from molecular precursors, specifically aromatic molecules containing halogen atoms. As illustrated in Fig. 1.7, the precursors are heated on a substrate, which removes halogen groups from the precursors and causes them to fuse together, forming a polymerised chain of aromatic building blocks. Further thermal treatment

converts this polymerised chain into a flat graphene nanoribbon. This fabrication method allows one to obtain very precise and narrow GNRs, since their dimensions are strictly defined by the structure of the molecular precursors used in the synthesis. The study by Cai et al. reported fabrication of armchair-edged GNRs with just $n = 7$ atoms across the nanoribbon, which is a significantly smaller width than any reported previously. By tailoring the structure of the molecular precursors, it is also possible to fabricate complex interconnected patterns, such as junctions of three GNRs connected at 120° to each other. In another study, a similar bottom-up fabrication method was used to obtain zigzag-edged GNRs for the first time [26]. Measurements performed on the obtained ZGNRs confirmed the existence of edge-localised states, predicted by previous theoretical studies.

Another bottom-up fabrication method is chemical vapor deposition (CVD), which is often used to produce large sheets of monolayer graphene [27]. In one of the first experimental reports on this method, CVD was used to produce large quantities of mostly multilayer GNRs of various dimensions [28]. In the reported approach, a mixture of carbon-containing precursors is first turned into an aerosol by sonication and then heated and sprayed onto a substrate. This approach was later improved by using a highly anisotropic Cu surface to guide the formation of oriented GNRs during the CVD process [29]. Similarly to the previously described surface-assisted bottom-up fabrication of GNRs, it is possible to control the dimensions and edge geometry of GNRs obtained through CVD by choosing specific aromatic molecules as chemical precursors for the synthesis process [30].

1.2 Modifying properties of graphene nanoribbons

1.2.1 Electric field control of electronic properties

One of the most efficient ways to tune electronic properties of materials in real time is the application of an external electric field. Since the discovery of graphene, a considerable effort has been directed towards modelling the response of various graphene nanostructures to electric fields [7, 31, 32]. These studies have led to a discovery of a diverse range of novel electronic phases in graphene nanostructures and become instrumental in designing electronic devices based on graphene. Before proceeding to exploring the existing studies on graphene nanoribbons in an electric field, it is instructive to first discuss the general principles

behind electric-field driven modification of electronic properties.

A convenient demonstration of the electric field effect is the application of homogeneous electric field to a charged particle confined in a one-dimensional quantum well [33]. The wavefunctions and energies of a charged particle localised in a potential well of dimensions $[-a/2, a/2]$ are given by

$$\psi_n(x) = \sqrt{\frac{2}{a}} \begin{cases} \cos\left(\frac{\pi n x}{a}\right), & n \text{ is odd} \\ \sin\left(\frac{\pi n x}{a}\right), & n \text{ is even} \end{cases} \tag{1.1}$$

$$E_n = \frac{\hbar^2 \pi^2}{2ma^2} n^2, \tag{1.2}$$

where $n = 1, 2, 3, \ldots$ is the quantum number. Notably, the quantum states with odd n are even with respect to reflection $x \to -x$, while the states with even n are odd. The potential energy of the confined particle in the external electric field is given by

$$V(x) = -qFx, \tag{1.3}$$

where q is the charge of the particle and F is the electric field strength. This potential is odd with respect to reflection $x \to -x$ and thus couples the quantum states of opposite parities in the quantum well. In a general form, the perturbation matrix elements are equal to

$$V_{nk} = \int_0^a \psi_n(x) V(x) \psi_k(x) dx = qF B_{nk} a, \tag{1.4}$$

where

$$B_{nk} = (-1)^{(n+k-1)/2} \frac{8nk}{(n^2 - k^2)^2 \pi^2} \tag{1.5}$$

if n and k are of opposite parities and $V_{nk} = 0$ otherwise. The strength of electric field effect is well quantified by the ratio of the perturbation matrix elements to the energy spacing between the quantum states of the system:

$$\frac{V_{nk}}{E_n - E_k} = \frac{2meF}{\hbar^2 \pi^2} \frac{B_{nk}}{n^2 - k^2} a^3. \tag{1.6}$$

The most important result of this simple analysis is that the relative strength of the electric field effect scales as $\propto a^3$ with the characteristic length of quantum confinement. The effect of external electric is thus significantly amplified if the external electric field is aligned parallel to the largest confining (i.e., non-periodic) dimension of the nanostructures.

It thus becomes evident that in the case of graphene nanoribbons (GNRs), the most pronounced modification of electronic properties is achieved if the external electric field is directed perpendicular to the periodic direction of the nanoribbon, along its width. Application

of the electric field perpendicular to the atomic plane of the graphene nanoribbon leads to a negligible electric field effect, since GNRs are only one-atom thick, and the electric field effect in this case originates only from the inherent polarisability of atomic orbitals. However, in the case of bilayer and multilayer GNRs, it should be possible to modify their electronic properties by applying an out-of-plane electric field. The spacing between the two layers of graphene is large enough to host noticeable re-distribution of electronic density under an applied out-of-plane electric field.

Arguably the first study in this direction was the study of zigzag graphene nanoribbons in a transverse homogeneous electric field [34]. Using first-principles calculations, the authors revealed the emergence of half-metallic behaviour in ZGNRs in strong electric fields. The existence of this electronic phase was theorised for a long time [35]. In a half-metal, the band structure for one-electron spin is insulating, whereas the band structure for the other electron spin is conducting, as shown in Fig. 1.8(c). The discovery of half-metallicity in graphene nanoribbons has a potential to revolutionise their device applications, leading to spintronic devices in which the information is stored and processed via electron spin [36]. The emergence of the half-metallic phase in ZGNRs in a transverse electric field was attributed to the energy shifts of the edge states, induced by the potential difference between the edges of the nanoribbon.

The electric field effect was also analyzed in graphene nanoribbons with armchair edges. Among the first works in this direction, extended Hückel theory revealed that the energy gap of AGNRs reduces upon application of a transverse electric field [37]. This behaviour was found to be qualitatively similar in all three families of AGNRs. A later study, that relied on *ab initio* calculations, analyzed the effect of a transverse electric field on AGNRs whose edges were doped with B atoms on one side and N atoms on the other side [38]. Since B and N atoms have different electronegativities from carbon, they become charged in these systems and generate a built-in electric field. The interplay between this intrinsic field and the applied gate voltage allows engineering topological properties of AGNRs by closing and re-opening their energy gaps. For examples, it is possible to induce topologically protected end states in B,N-codoped ANGRs by applying an external electric field of sufficient strength. In Chapter 4 of this dissertation, I study the electric field effect in AGNRs and reveal the origin of the band gap closing in these nanoribbons under the influence of a strong external or internal electric field.

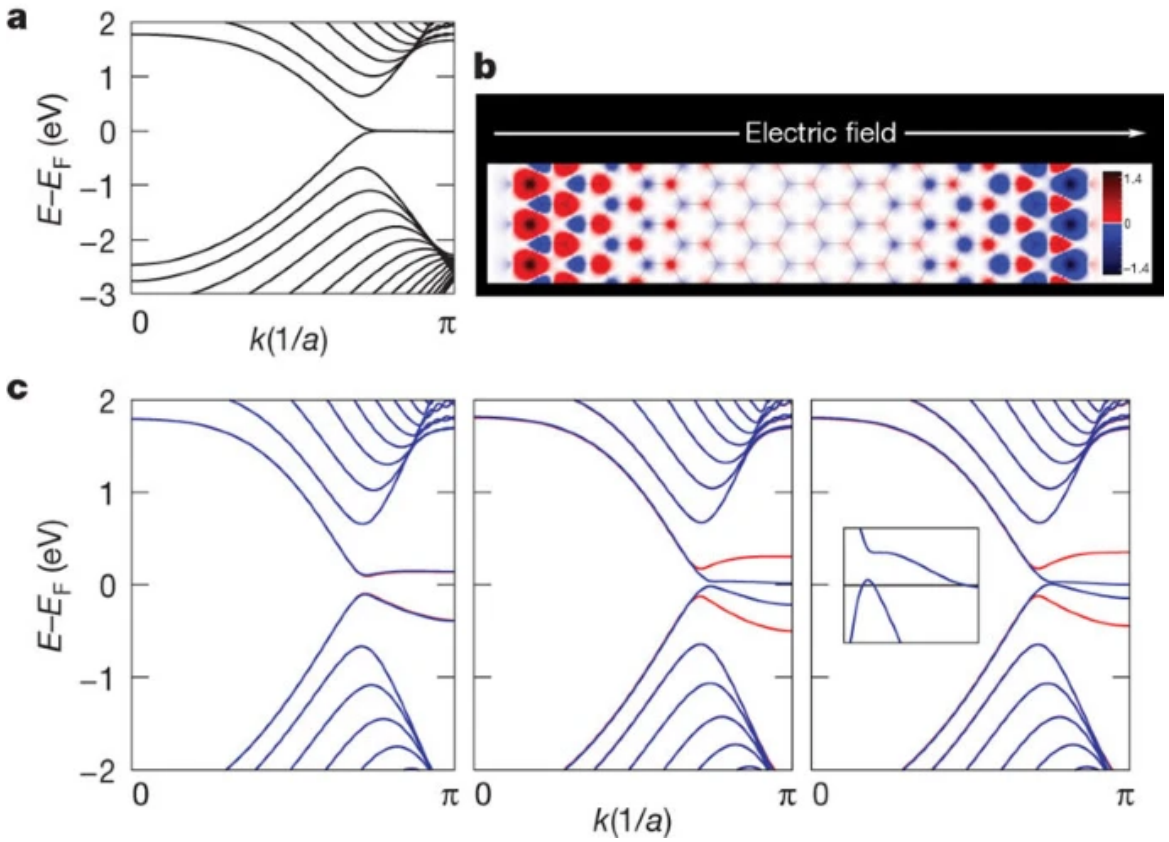


Figure 1.8: (a) The spin-unpolarized band structure of a 16-ZGNR. (b) The spatial distribution of the charge difference between α-spin and β-spin for the ground state when there is no external field. (c) From left to right, the spin-resolved band structures of a 16-ZGNR with $E_{\text{ext}} = 0.0$, 0.05 and 0.1 V/Å, respectively. The red and blue lines denote bands of α-spin and β-spin states. Reprinted with permission from *Nature* **444**, 347–349 (2006) [25]. Copyright 2006 Springer Nature.

In another paper, a tight-binding model for π-electrons was used to analyse the electric field effect in a subclass of chevron graphene nanoribbons [39]. Such nanoribbons have unique "jagged" edges instead of continuous edges as in the case of AGNRs and ZGNRs. The application of a transverse electric field in these systems induces band gap modifications, which are more pronounced in jagged graphene nanoribbons of larger widths. Notably, the application of an electric field induces the formation of flat conduction and valence bands. These energy bands are associated with strongly localized electrons and holes, which become trapped in the jagged parts of the edges due to the electric potential. While it was not discussed by the authors of this study, we could argue that the existence of such flat bands makes it possible to induce magnetism in chevron graphene nanoribbons by applying a transverse electric field and doping them with electrons or holes. Research in this direction is continuing at the moment of writing this thesis.

Just like graphene, GNRs can be stacked on top of each other to form bilayer or multilayer graphene nanoribbons. In the case of multilayer structures, noticeable electronic structure modification can be also observed upon application of an out-of-plane electric field, which induces re-distribution of electron density between the layers of the material. One of the first studies in this direction used a very simple two-leg ladder model to analyze the variation of the band gap of Bernal-stacked bilayer graphene nanoribbons with the strength of an out-of-plane external electric field [40]. It was revealed that the electric field increases the band gap of narrow bilayer GNRs and decreases the band gap of wide graphene nanoribbons.

Further tight-binding and first-principles studies analysed few-layer graphene nanoribbons in both transverse and out-of-plane electric fields [41–44]. It was observed that strong electric fields are capable of closing the energy gap of multilayer graphene nanoribbons, thus driving a metal-to-semiconductor phase transition. Alternatively, electric fields are capable of opening an energy gap in ABC-stacked trilayer and other multilayer graphene nanoribbons lacking a gap in their pristine state. The changes in the band structure of bilayer graphene nanoribbons were found to be very similar to the electric-field driven modification of the electronic properties of bilayer graphene [7]. Overall, it was revealed that the properties of multilayer graphene nanoribbons and their response to electric fields is extremely dependent on the interlayer stacking and interactions.

1.2.2 Integration with hexagonal boron nitride

Hexagonal boron nitride (hBN) is a two-dimensional material consisting of B and N atoms packed in a hexagonal crystal lattice, similar to that of graphene. Each boron atom in hBN is neighboured by three nitrogen atoms, and vice versa. A pair of B and N atoms has the same number of valence electrons as two C atoms, making the bonding pattern in hBN very similar to that in monolayer graphene. In both two-dimensional lattices, atoms are held together by strong σ-bonds enabled by the sp^2-hybridization of the valence orbitals in the in-plane direction, whereas the electronic properties are mainly determined by the π-bonding of the p_z-orbitals that are perpendicular to the bonding direction. The difference in electronegativities of boron and nitrogen atoms results in hBN being an insulator with a wide band gap of around 6 eV [45].

Owing to the strong ionic bonding in the in-plane direction, hBN is a highly inert mate-

rial, making it an excellent substrate for various other two-dimensional structures [45]. The lattice constants of graphene and hBN match quite closely (2.46 Å versus 2.51 Å), making it possible to integrate the two materials in heterostructures without inducing a particularly strong mechanical stress in either of the layers. If used as a substrate, hBN can open an energy gap in monolayer graphene by inducing a difference of onsite energies between its two sublattices, so that electrons and holes of graphene effectively acquire non-zero mass [6]. It is also possible to construct various heterostructures consisting of alternating graphene and hBN layers stacked on top of each other [46].

Due to the close similarity of their lattice constants, graphene and hBN can also be integrated laterally to form in-plane heterojunctions [47]. The first experimental realisation of such heterojunctions was reported in 2010 by Ci et al., who fabricated hybridized layers of graphene and hBN by combining B-, C-, and N-containing precursors in the CVD method [48]. This resulted in a monolayer consisting of distinct patches of graphene and hBN. The measured electronic properties of this new material as a whole were found to be qualitatively different from the properties of pristine graphene or hBN. The main drawback of this fabrication method is the lack of precise control over the graphene-hBN interfaces in the hybridized system.

In 2012, Levendorf et al. reported an improved fabrication approach that allows control over the shape of the hBN regions embedded in the graphene layer [49]. In their method, a film of monolayer graphene is first grown on a copper substrate using CVD. A protective layer of photoresist is then applied to the copper substrate, while the unwanted patches of graphene are removed via etching. Finally, a layer of hBN was grown using the same CVD approach, filling in the gaps in the graphene layer. Conductance measurements confirmed that the regions of hBN in the resulting heterojunction were laterally insulating, while the graphene patches remained conducting. It was thus successfully demonstrated that it is possible to combine conducting and insulating materials within the same monolayer.

This fabrication method was further advanced by Liu et al. in 2013, who achieved precise control over the shape and geometry of graphene/hBN interfaces with the resolution of fine elements as small as 100 nm [50]. In their approach, an hBN layer is first grown on a copper substrate using CVD and then partially etched at the regions defined by a laser-cut mask. Graphene is grown from precursors in the etched regions of hBN. Finally, the copper

substrate is washed away, resulting in a monolayer consisting of hBN and graphene patches stitched together with high precision.

In their seminal study, Sutter et al. used real-time microscopy to track the formation of graphene-hBN interfaces in hybridized layers fabricated on a metal substrate using CVD [51]. They revealed that the growing hBN monolayer in the hybridised graphene-hBN heterojunction becomes doped with C atoms owing to the incorporation of C adatoms from the metal substrate. By eliminating these adatoms from the metal surface with careful chemical etching, the authors managed to achieve atomically sharp graphene/hBN interfaces in these in-plane heterojunctions.

In 2013, Gao et al. reported precise fabrication of graphene/hBN interfaces with a specific type of graphene edges, either armchair or zigzag [52]. They also used density functional theory calculations to determine the formation energies of both types of interfaces and revealed that zigzag graphene edges are more energetically favourable at the interfaces with hBN. This result is of crucial importance for the present work, since Chapter 5 of this dissertation is focussed entirely on studying the unique electronic phenomena arising at the interfaces between zigzag-edged graphene nanoribbons and hBN.

In 2017, Chen et al. reported the first fabrication of narrow graphene nanoribbons embedded in hBN [54]. In their approach, a sheet of hBN is first grown on a quartz substrate. The hBN sheet is then bombarded with Ni nanoparticles, creating narrow trenches in the monolayer. These trenches are subsequently filled with graphene nanoribbons grown from precursors. Wang et al. later advanced this approach by achieving chirality control over graphene nanoribbons grown in the hBN layer [53]. They demonstrated that depending on the type of nanoparticles used to create trenches in the hBN layer, GNRs grown in these trenches have either armchair or zigzag edges, as shown in 1.9. They also performed conductance measurements on both AGNRs and ZGNRs embedded in hBN, revealing non-zero conductance at the Fermi level of ZGNR/hBN heterojunctions.

When ZGNRs are embedded in a sheet of hBN, their edges are terminated in such a way, that all C atoms on one edge of the nanoribbon are bonded with B atoms, while all C atoms on other edge are terminated with N atoms. Due to the difference of electronegativies of boron and nitrogen, one can intuitively expect this to create a built-in transverse electric field in ZGNR/hBN heterojunctions. As was demonstrated by Son et al., a strong enough

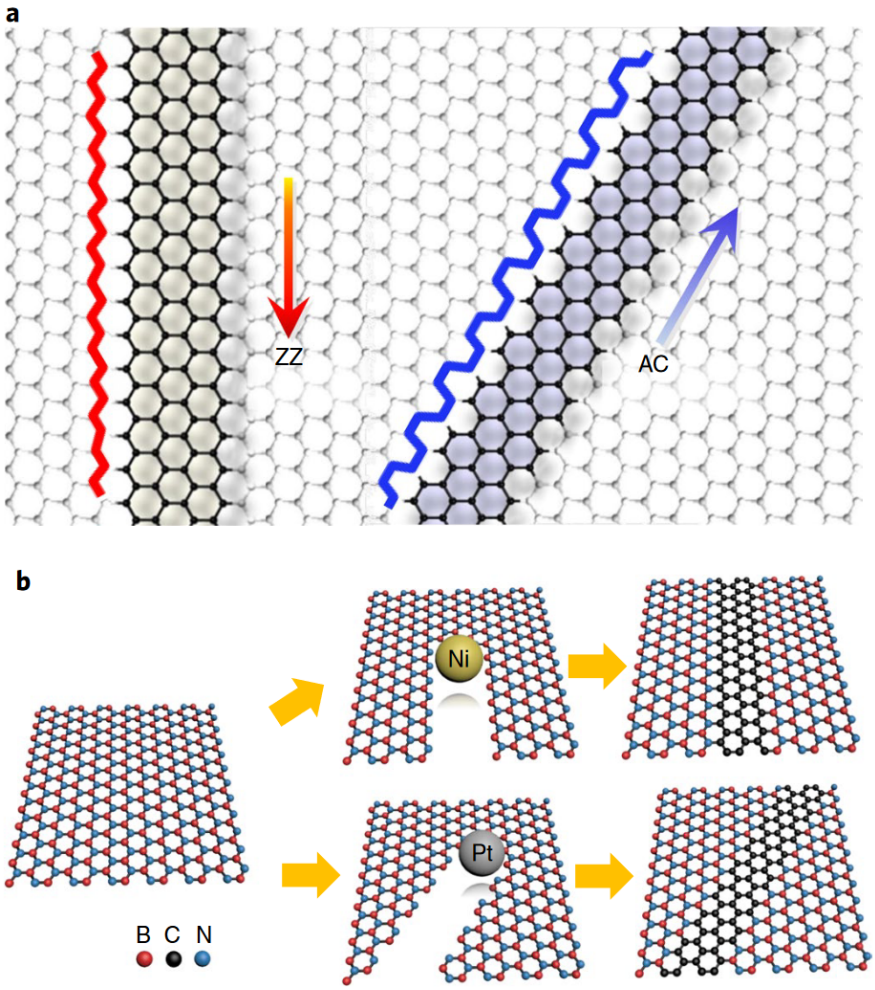


Figure 1.9: (a) Sketch of ZGNR and AGNR embedded in hBN. (b) Synthetic strategy to orient GNRs with crystallographic edge orientations. Different particles cut nano-trenches with different edge topologies in the hBN layer. The edge-specific nano-trenches are used to define the growth and the dimensions of GNRs along the zigzag (top) or armchair (bottom) direction. Reprinted with permission from *Nature Mater.* **20**, 202–207 (2021) [53]. Copyright 2021 Springer Nature.

transverse external electric field can induce half-semimetallicity in ZGNRs [34], indicating that ZGNR/hBN heterojunctions may also be half-metallic. This assumption is somewhat supported by the experimental observation of non-zero conductance at the Fermi level of the system.

The properties of graphene/hBN interfaces at the computational level were addressed even before the experimental realisation of such nanostructures. In 2009, Ding et al. used first principles calculations to analyse the stability and electronic properties of graphene nanoribbons at the interface with narrow strips of hBN [55]. It was found that both AGNRs and ZGNRs remain stable and planar when embedded in hBN. While all AGNRs embedded in hBN

are semiconductors, ZGNR can acquire half-semimetallicity at certain widths. The formation of this half-semimetallic phase was later explained by spin-asymmetric screening arising from the interplay of edge magnetism in graphene nanoribbons and charge polarity in the strips of hBN [56]. Similar conclusions were made in a later study that relied on the tight binding Hamiltonian in the mean-field approximation [57].

In another computational study, electronic properties of the single ZGNR/hBN interfaces, shown in Fig. 1.10, were studied using first-principles calculations [58]. The outer edges of both graphene and hBN nanoribbons are dihydrogenated in this structure. It was revealed that depending on the width of the graphene and hBN nanoribbons in these hybrid structures, they can be either semiconducting, half metallic, or metallic. The formation of the half-metallic phase was attributed to the localised states at the dihydrogenated outer edges of the two nanoribbons.

Through detailed first-principles calculations, Zeng et al. showed that orientationally misaligned interfaces between graphene nanoribbons and hBN may be even more favourable for experimental realisation [59]. A small lattice mismatch between graphene and hBN induces mechanical stress in graphene nanoribbons embedded in large sheets of hBN, which is especially strong in wider graphene nanoribbons. Orientational misalignment eliminates this mechanical stress and can also make the half-metallic phase more robust due to the enhanced superexchange interaction between the localised edge states of the graphene nanoribbon [60].

Due to the computational limitations of that time, many of these theoretical studies had to consider narrow one-dimensional strips of hBN instead of large two-dimensional lattices. This fact might have affected the results obtained in those studies, since many of them found the half-metallic phase to be dependent on the width of the hBN nanoribbons. The recent experimental fabrication of graphene nanoribbons embedded in hBN [53, 54] highlights the importance of new computational studies on this topic, using improved computational powers and new methodologies. In Chapter 5 of this dissertation, I thoroughly explore the electronic and magnetic properties of zigzag graphene nanoribbons embedded in large, fully two-dimensional sheets of hexagonal boron nitride. I show that such ZGNR/hBN heterojunctions are half-semimetallic, as the semiconducting behavior in one spin orientation is accompanied by a Dirac semimetallic behavior in the other, while preserving the intrinsic antiferromag-

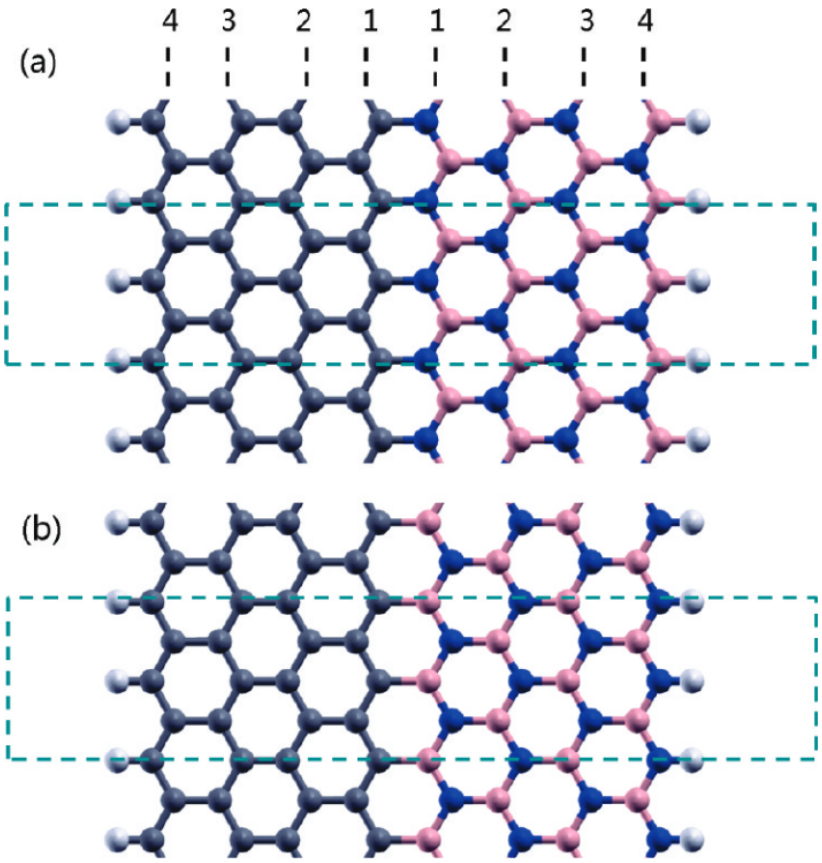


Figure 1.10: Atomic structures of hybrid graphene/hBN nanoribbons, in which the edge carbon atoms of the graphene nanoribbon are terminated by (a) boron and (b) nitrogen atoms. Black, pink, and blue spheres denote C, B, and N atoms, respectively, whereas white spheres denote H_2 pairs (not distinguishable in the top-down view). Reprinted with permission from *J. Phys. Chem. C* **115**, 9442–9450 (2011) [58]. Copyright 2011 American Chemical Society.

netism of ZGNRs. I attribute the origin of this half-semimetallic phase to the charge transfer at the interfaces between the magnetic edges of the nanoribbon and the hexagonal boron nitride. I also show that charge doping can further modulate the electronic structure of the heterojunctions by enforcing a *ferrimagnetic* ground state and enabling precise control over the spatial localization of magnetic moments. Overall, ZGNR/hBN heterojunctions realise one-dimensional conducting channels of spin-polarized Dirac fermions embedded within a two-dimensional insulator, opening new avenues for the exploration of spintronic devices based on graphene.

1.3 Optical properties of graphene nanoribbons

1.3.1 Linear absorption and emission

Due to its linear band structure around the Fermi level, monolayer graphene is characterised by a uniform absorption intensity in a broad spectral range [61], which makes it less suitable for various optical applications where wavelength-selectivity is preferred. Graphene nanoribbons, on the other hand, are naturally expected to have rich features in their optical spectra, arising from the size-quantization of their energy bands. Early theoretical studies relied on the simplest tight-binding approximation to identify the selection rules of optical transitions in GNRs and obtain their absorption spectra [62–65]. According to the findings of these studies, the absorption peaks in the optical spectrum of GNRs naturally resemble the density of states of a 1D electron gas. The tight-binding models in these studies, however, did not include the electron-electron repulsion terms in the Hamiltonian, making their results somewhat less reliable for zigzag graphene nanoribbons, which have flat energy bands at the Fermi level.

Barone et al. later used ab initio simulations to obtain the absorption spectra of graphene nanoribbons with chiral edges as a part of a larger first-principles study on the electronic properties of GNRs and their stability [66]. It was found that the width of the nanoribbon plays a crucial role in determining the positions of the absorption peaks in the spectrum, as the bandgap of the nanoribbon changes dramatically with its width. It was also found that the termination of the nanoribbon's edges with H atoms leads to a shift of the absorption peaks compared to GNRs with bare edges. This indicates that the optical spectra can be used to probe the width and edge termination of graphene nanoribbons in experiments.

The above studies used approaches developed for calculating ground-state electronic properties of graphene nanoribbons and could, therefore, miss important physics arising from the excitation of electrons upon optical absorption. A later study corrected this by using the GW approximation to calculate the energies of excited states in AGNRs, thus obtaining their correct optical absorption spectra [67]. The results of these GW calculations for an AGNR with 10 atoms across the unit cell are presented in Fig. 1.11. It was found that the reduced dimensionality of AGNRs significantly enhances the electron-hole interaction, leading to huge exciton binding energies in the range 0.8–1.4 eV for AGNRs with width of around 1.2 nm.

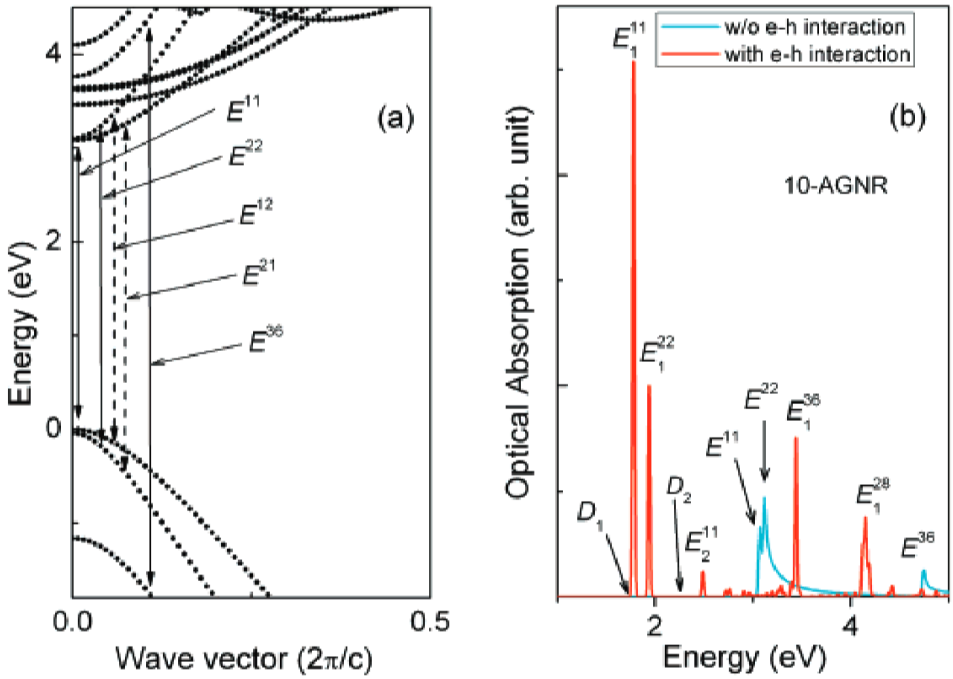


Figure 1.11: (a) Band structure of an armchair graphene nanoribbon with 10 atoms across the nanoribbon (10-AGNR). (b) Optical spectra of this nanoribbon, calculated with and without taking into account electron-hole interactions. Reprinted with permission from *Nano Lett.* **7**, 3112–3115 (2007) [67]. Copyright 2007 American Chemical Society.

This results in a red shift of the absorption peaks, while the band-edge absorption is dramatically enhanced due to the transfer of oscillatory strength from the motion of electron in the periodic direction of the nanoribbon to the excitonic transitions. Similar results were later obtained in a theoretical study on the many-body effects in AGNRs [68].

The first experimental characterisation of the optical properties of GNRs was reported much later than the first theoretical studies owing to the challenges in isolating GNRs for optical measurements. In 2013, Chernov et al. fabricated GNRs encapsulated into single-wall carbon nanotubes (CNTs) and measured their absorption, photoluminescence, and Raman spectra [69]. It was demonstrated that GNRs produce an optical signal that is distinct from the absorption and emission of CNTs. As was previously theorised, the authors of this experimental study demonstrated that optical characterisation of GNRs is a promising way of identifying their structure and the geometry of their edges. The key problem with this approach is the difficulty of differentiating the absorption features of CNTs encapsulating GNRs from the spectral peaks of GNRs themselves. In 2015, Lim et al. managed to overcome this issue by functionalising the surface of the carbon nanotubes [70]. This disrupted the π-

conjugated network of the CNTs and moved their absorption peaks away from the spectral region corresponding to the absorption and photoluminescence of GNRs.

Other studies reported measurements of absorption in armchair graphene nanoribbons on a metal substrate [71]. It was found that unlike graphene, which has wavelength-independent absorption, GNRs feature sharp absorption peaks, whose positions depend on the nanoribbon's width. GNRs placed on a metal substrate were found to lack any emission due to the photoluminescence quenching by the metallic surface. The authors of a different study used laser irradiation to induce photoluminescence in GNRs on a metal substrate, which resulted from the formation of sp^3-hybridised defects in the planar geometry of graphene nanoribbons [72, 73]. Ensuing advancements of the fabrication methods made it easier to obtain photoluminescent GNRs via bottom-up approaches [74, 75].

Overall, despite some important advancements in the optical studies of GNRs, this field is somewhat shadowed by the ongoing research on their electronic and magnetic properties. Applications of GNRs in photonic devices are rarely discussed, and the optical measurements are usually viewed as a way of characterising the geometry of graphene nanoribbons in experiments. Other carbon-based nanostructures, such as carbon dots, remain more attractive for optical applications due to their much more robust photoluminescence properties and the ease of fabrication [76]. In an endeavor to change this situation, Chapter 6 of this thesis suggests twisted graphene nanoribbons for applications in chiral nanophotonics.

1.3.2 Chiral graphene nanostructures

Chiral objects are defined by their lack of mirror symmetry. Two mirror images of a chiral object, called enantiomers, cannot be superimposed on each other by any translations or rotations in space. Chiral nanostructures, in particular, have attracted a great deal of attention from material scientists due to their promising applications. The key property of chiral materials is the optical activity — differential interaction with the opposite circular polarisations of light. More specific examples of optical activity in chiral nanostructures are circular dichroism (CD), the difference of absorption rates for the left- and right-circularly polarised radiation, and circularly polarised luminescence (CPL), the difference of emission intensities for two circular polarisations. One of the most important measures of optical activity is the dissymmetry factor (or g-factor), which is a dimensionless quantity defined as the ratio of CD

to linear absorption of a material. The g-factors of typical chiral nanoparticles and molecules lie in the range of 10^{-4}–10^{-3} [77].

Applications of chiral nanostructures include devices specialising in emission or detection of circularly polarised radiation, such as circularly polarised light-emitting diodes [78, 79]. Chiral nanomaterials can also be used as enantioselective sensors for chiral molecules or catalysts for chiral synthesis [80, 81]. The interaction of numerous chiral drug molecules with the human body depends drastically on whether the left- or right-handed enantiomer of the molecule is used. It is therefore necessary to be able to detect the chirality of the molecules or favour the formation of a specific enantiomer during chemical synthesis. Chiral nanostructures can assist with both of these tasks by selectively binding to chiral molecules of specific handedness, depending on the chirality of the nanostructures themselves [82, 83]. Chiral nanostructures can also be used in spintronic devices due to the chirality-induced spin-selectivity of electric currents in chiral materials [84, 85].

Regardless of a particular application, it is highly desirable to have access to chiral nanomaterials with the strongest possible optical activity. Graphene, given its unique electronic and optical properties, has been a focus of attention as a base material for various chiral nanostructures [86]. As one of the most notable examples, chiral graphene quantum dots (GQDs) can be fabricated by functionalising the edges of small flakes of monolayer graphene with chiral ligand molecules [87, 88]. These chiral molecules cause GQDs to twist, with the direction of this twist being determined by the chirality of the ligands. The measured CD and g-factor spectra of chiral GQDs fabricated by Suzuki et al. and the theorised atomic structure of these nanoparticles are shown in Figure 1.12. It is seen that the CD signal of chiral GQDs is mostly observed in the ultraviolet spectral range, with the g-factors being relatively small, i.e., of the order of 10^{-4}.

A theoretical study by Tepliakov et al. proposed chiral graphene quantum dots made from twisted bilayer graphene [89]. The chirality of these twisted bilayer graphene quantum dots (TBGQDs), shown in Figure 1.13, stems from the intrinsic rotation of the two graphene layers with respect to each other [90]. Compared to the previous example of chiral GQDs, the planar geometry of graphene layers is not distorted in TBGQDs, resulting in a large oscillatory strength of the optical transitions polarised in the in-plane directions of the quantum dots [91, 92]. As a result, TBGQDs were predicted to have dissymmetry factors of the order of 10^{-2},

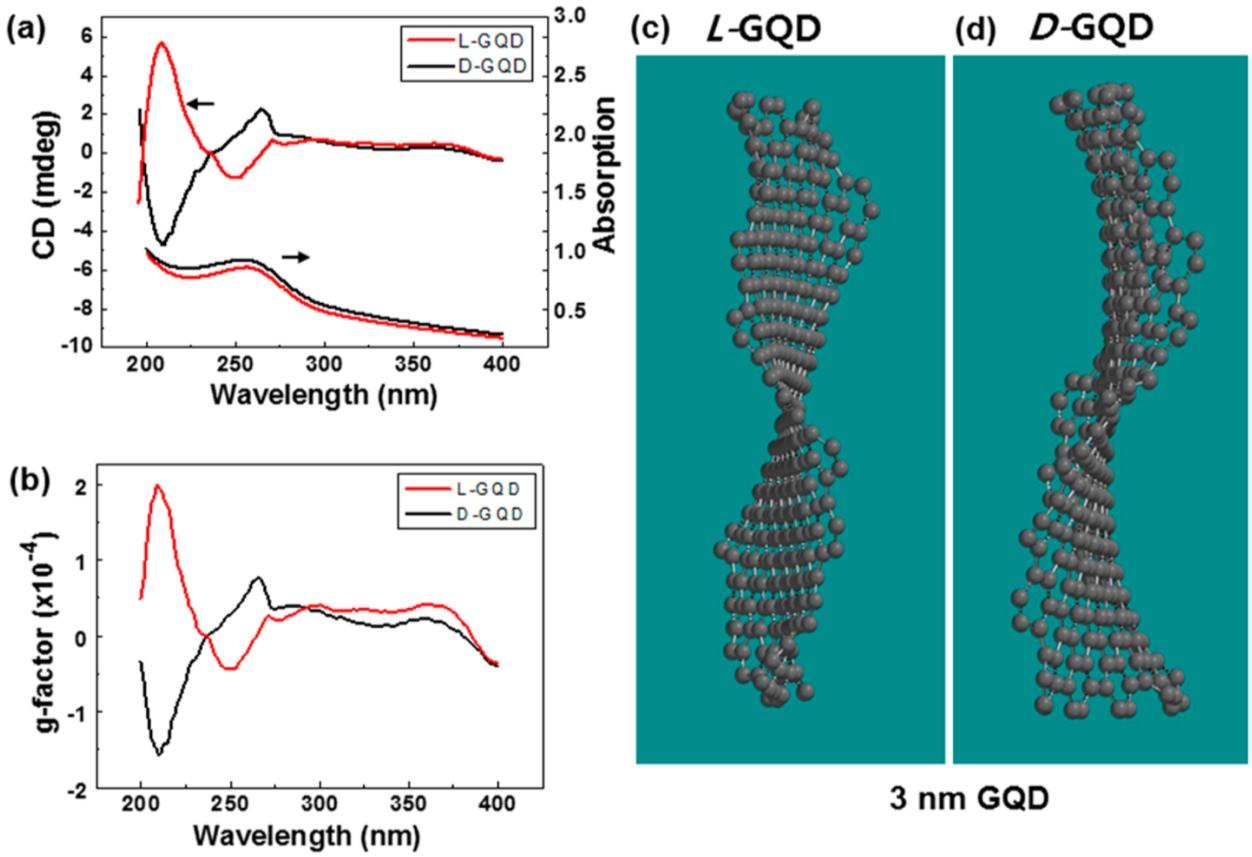


Figure 1.12: (a) Circular dichroism and (b) g-factor spectra of two enantiomers of chiral graphene quantum dots (GQDs). (c, d) Theorised geometry of chiral GQDs of two opposite chiralities. The chiral ligands, functionalising the quantum dots, are removed for clarity. Reprinted with permission from *ACS Nano* **10**, 1744–1755 (2016) [88]. Copyright 2016 American Chemical Society.

greatly exceeding the dissymetry factors of twisted monolayer GQDs.

Carbon nanotubes (CNTs) of certain crystallographic orientation are intrinsically chiral due to the helical rotation of atoms around the axis of the nanotube. A 2006 theoretical study calculated CD spectra of CNTs of various spatial dimensions and crystallographic orientations [93]. Experimental characterization of chiral optical properties of these nanostructures posed a challenge due to the challenges in isolating CNTs of specific crystallographic orientation. Wei et al. used advanced chromatographic techniques to isolate CNTs of specific chirality and measured their circular dichroism spectra as a function of the chirality index of the nanotubes [94]. Another experimental study of isolated CNTs revealed strong extrinsic chirality in this nanostructures — if the incident circularly polarised radiation is aligned at a certain angle with respect to the axis of the nanoribbon, the interplay between the intrinsic chirality of the CNTs and the circular polarisation of the light leads to giant dissymmetry factors of the order

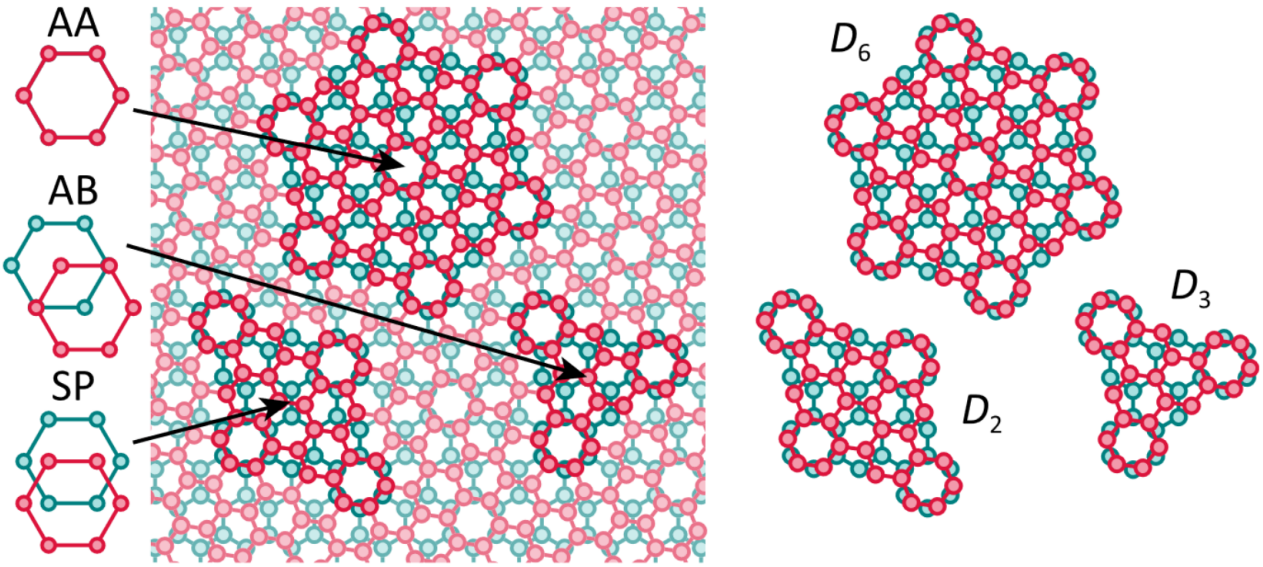


Figure 1.13: Two-dimensional lattice of twisted bilayer graphene for an interlayer twist angle of 21.8° and three quantum dots (QDs) corresponding to the dihedral point symmetry groups D6, D3, and D2. The symmetries of the QDs are determined by the stackings of the two layers at the QD center, which resemble the AA, AB, and SP stackings in bilayer graphene shown on the left. Reprinted with permission from *J. Phys. Chem. C* **124**, 22704–22710 (2020) [89]. Copyright 2020 American Chemical Society.

of 0.1 to 1 [95].

Graphene nanoribbons, while achiral in their planar geometry, can be made chiral by twisting [96]. Twisted GNRs are synthesised in a bottom-up fashion from organic precursors that, unlike in the conventional synthesis of planar GNRs, contain various additional atoms that cause organics precursors to rotate with respect to each other, so that the nanoribbons obtained by this method are twisted around their longitudinal axis, as shown in Fig. 1.14. Mahlmeister et al. used this approach to obtain twisted GNRs of specific chiral orientation and measured their circular dichroism. Depending on the type of precursors used, the opposite ends of the twisted nanoribbon can connect, thus forming a closed loop. Fabrication of such chiral nanostructures was reported by Fan et al., who also demonstrated that these chiral nanoribbons feature strong optical activity with the dissymmetry factors reaching 0.01 [97].

A particularly striking example of chirality in graphene nanoribbons was reported by Segawa et al. [98]. In their approach, Möbius graphene nanobelts are synthesized in a bottom-up fashion starting from nanoribbons made of carbon, bromine, and hydrogen and functionalized with oxygen-containing groups. The geometry of these nanoribbons forces

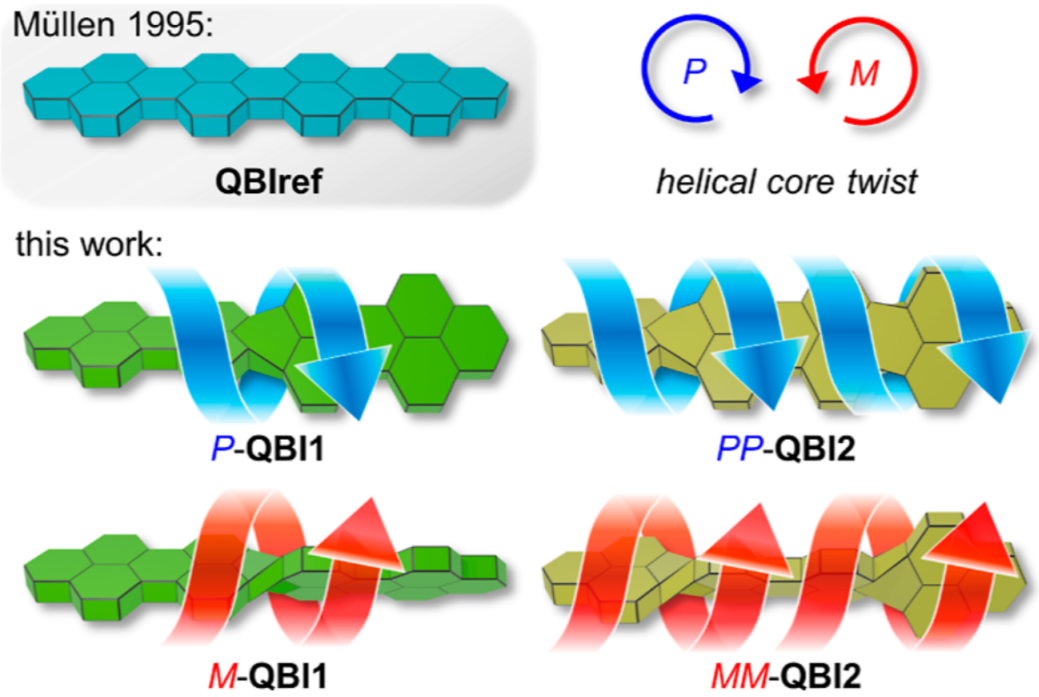


Figure 1.14: Schematic representation of planar quaterrylene bisimides (QBIs) reported by Müllen in 1995 and twisted QBIs, representing twisted graphene nanoribbons. Reprinted with permission from *J. Am. Chem. Soc.* **144**, 10507–10514 (2022) [96]. Copyright 2022 American Chemical Society.

them to twist along their axis and simultaneously bend, forming a loop. Given a right length of the nanoribbon, its opposite ends are rotated by 180° with respect to each other, thus resulting in a Möbius nanostrip. The spectroscopic studies revealed strong optical activity of the fabricated Möbius graphene nanostrips, with the dissymmetry factors ranging between 10^{-3} and 10^{-2}. As shown in Fig. 1.15, these nanostructures have rich spectral features.

The shape of the Möbius nanostrip is not only chiral but also topologically nontrivial due to it being a non-orientable surface, leading to a range of unique electronic properties of such structures. Beugeling et al. developed a general theory of a Möbius band and demonstrated that that its lack of orientability prevents a global definition of pseudovectors, including magnetic field [99]. It was argued that because of this, Möbius structures cannot host the quantum Hall effect, while the quantum spin Hall effect can still be observed in this geometry. The following theoretical studies confirmed that Möbius bands indeed feature the quantum spin Hall effect, induced by the curvature of the strip [100]. Another study revealed the presence of topological Floquet states in Möbius bands, induced by irradiation with circularly polarised light [101].

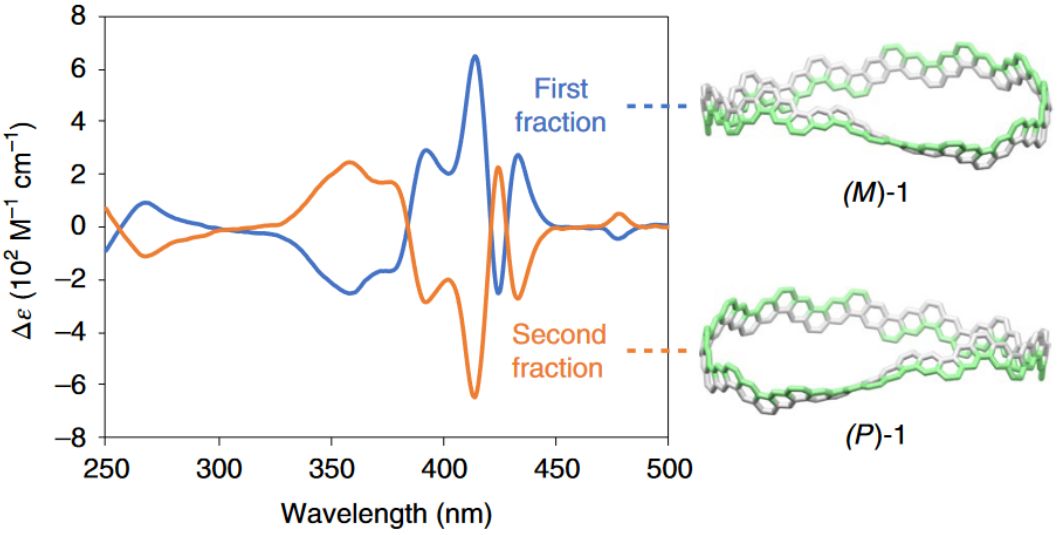


Figure 1.15: Circular dichroism ($\Delta\varepsilon$) spectra of two enantiomers of Möbius carbon nanobelts with their tentative atomic structures. Functional groups at the edges of the nanobelts are omitted for clarity. Reprinted with permission from *Nature Synth.* **1**, 535–541 (2022) [98]. Copyright 2022 Springer Nature.

The unique topology of the Möbius band also leads to unique magnetic properties of graphene nanostrips with such shapes. It was discussed previously that zigzag graphene nanoribbons are antiferromagnetic, with the two edges of the nanoribbon hosting magnetic momemnts of equal magnitude and opposite sign. The Möbius strip, however, has only a single edge. Several theoretical studies demonstrated that this unique feature makes Möbius graphene nanostrips with zigzag edges ferromagnetic at half-filling [102, 103]. Another theoretical study addressed the optical properties of graphene nanostrips of Möbius geometry, obtaining their absorption spectra [104]. This study, however, did not analyse the circular optical properties of twisted graphene nanostrips.

It is natural to wonder how the topologically nontrivial geometry of Möbius graphene nanostrips affects their optical activity, a question that has not been assessed in previous theoretical studies, which focussed almost entirely on the electronic, magnetic, and topological properties of Möbius bands. In Chapter 6 of this thesis, I employ advanced theoretical methods to simulate the optical absorption and circular dichroism spectra of Möbius graphene nanostrips of various geometries. Motivated by the recent fabrication of these peculiar nanostructures, I confirm various experimental findings of Segawa et al. [98], such as the large dissymmetry factors of Möbius graphene nanostrips of small dimensions. Overall, this

highlights twisted graphene nanostrips of Möbius shape as highly promising nanostructures for chiral optical applications.

1.4 Conclusions

Over the past two decades, graphene nanoribbons have emerged as a highly promising material for next-generation electronic and spintronic devices, thanks to their high charge carrier mobility, exceptional mechanical stability, tunable energy gaps, and intrinsic magnetic properties. Advances in fabrication techniques now allow for the reliable production of GNRs with varying sizes and shapes. Furthermore, their electronic properties can be significantly tailored by applying external electric fields or integrating them with other two-dimensional materials, such as hexagonal boron nitride. Despite these advances, there are still gaps in our understanding of the electronic behaviour of GNRs, and there is an increasing demand to engineer new functionalities in these nanostructures. This thesis addresses both of these challenges.

The subsequent chapters are organized as follows: Chapter 2 reviews the theoretical methods employed to compute the electronic and magnetic properties of GNRs. Chapter 3 provides a novel interpretation of the previously reported bandgap dependence in armchair graphene nanoribbons (AGNRs), revealing that a hidden symmetry governs their electronic structure. In Chapter 4, I demonstrate that strong transverse electric fields can induce a semimetallic phase in AGNRs and provide an explanation for this transition. Chapter 5 presents an in-depth theoretical study of the electronic and magnetic properties of zigzag graphene nanoribbons (ZGNRs) embedded in hexagonal boron nitride. Finally, Chapter 6 explores the potential of chiral graphene nanostrips of Möbius geometry for applications in chiral nanophotonics.

Chapter 2

Computational methods

2.1 Many-body Schrödinger equation

The theoretical investigation of graphene nanoribbons reported in the following chapters of this thesis relies heavily on two common computational methods: density functional theory and the tight-binding approximation. It is therefore necessary to provide an overview of these methods, focussing on their particular advantages and disadvantages in the modelling of graphene nanoribbons. It should be noted that the following sections do not form an exhaustive explanation of either density functional theory or the tight-binding approximation, but rather should be viewed as an introduction to these two methods and a guide to the main parameters that are at the disposal of someone using them. This chapter draws heavily on the fantastic book about density functional theory authored by Feliciano Giustino [105].

Generally, stationary quantum states of an arbitrary system are obtained by solving the Schrödinger equation of the form

$$\hat{H}\Psi = E\Psi, \tag{2.1}$$

where $\hat{H}$ is the Hamiltonian operator, Ψ is the wavefunction, and E is the energy of the quantum state. Common materials, including graphene nanoribbons, are Coulomb systems that are mostly driven by electrostatic interactions. A general Hamiltonian describing a system of

N electrons and M nuclei is given by

$$\hat{H} = -\sum_{i=1}^{N} \frac{\hbar^2}{2m_\mathrm{e}} \nabla_i^2 - \sum_{I=1}^{M} \frac{\hbar^2}{2M_\mathrm{I}} \nabla_I^2 + \sum_{i=1}^{N} \sum_{j=i+1}^{N} \frac{e^2}{|\mathbf{r}_i - \mathbf{r}_j|} + \sum_{I=1}^{M} \sum_{J=I+1}^{M} \frac{e^2 Z_I Z_J}{|\mathbf{R}_I - \mathbf{R}_J|} - \sum_{i=1}^{N} \sum_{J=1}^{M} \frac{e^2 Z_J}{|\mathbf{r}_i - \mathbf{R}_J|}, \quad (2.2)$$

where $\hbar$ is the reduced Planck constant, m_e is the free-electron mass, M_I is the mass of the Ith nucleus, e is the elementary charge, eZ_I is the charge of the Ith nucleus, Z_I is the atomic number, ∇_i (∇_I) is the nabla operator for the ith electron (Ith nucleus), and $\mathbf{r}_i$ ($\mathbf{R}_I$) is the coordinate of the ith electron (Ith nucleus). The first two operators in this Hamiltonian describe the kinetic energy of all electrons and all nuclei. The next two operators are the positive energies of repulsion between pairs of electrons and pairs of nuclei. Note that the CGS unit system is used, hence the factors of $1/(4\pi\varepsilon_0)$ are absent in these Coulomb terms. The final operator is the negative attraction energy between electrons and nuclei. Hamiltonian (2.2) captures all important interactions in non-relativistic materials. In the case of materials composed of heavy atomic species, it is also important to account for various relativistic effects, such as the spin of electrons, and solve the Dirac equation instead of the Schrödinger equation. Graphene, however, is well described using non-relativistic quantum mechanics.

Before we proceed, it is convenient to introduce the so-called atomic units, which will be used throughout this chapter. In these units, all distances are measured in Bohr radii,

$$a_0 = \frac{\hbar^2}{m_\mathrm{e} e^2}, \quad (2.3)$$

energies are measured in Hartree units,

$$E_\mathrm{Ha} = \frac{e^2}{a_0}, \quad (2.4)$$

and masses are measured in m_e. In atomic units, the Hamiltonian in Eq. (2.2) takes the following form:

$$\hat{H} = -\sum_{i} \frac{\nabla_i^2}{2} - \sum_{I} \frac{\nabla_I^2}{2M_\mathrm{I}} + \frac{1}{2} \sum_{i,j \neq i} \frac{1}{|\mathbf{r}_i - \mathbf{r}_j|} + \frac{1}{2} \sum_{I,J \neq I} \frac{Z_I Z_J}{|\mathbf{R}_I - \mathbf{R}_J|} - \sum_{i,J} \frac{Z_J}{|\mathbf{r}_i - \mathbf{R}_J|}. \quad (2.5)$$

From this point on, it will be assumed that indices i and j (I and J) always run over all electrons (nuclei). Factors of $1/2$ are introduced in the operators describing the repulsion of pairs of electrons and pairs of nuclei to compensate for the double counting of each pair in

the summations. It is worth noting that the only parameters in Hamiltonian (2.5) that are external to electrons are the nuclei masses M_I, atomic numbers Z_I, and radii $\mathbf{R}_I$. The rest of the Hamiltonian describes a general system of N interacting electrons.

Most electronic properties of materials can be calculated using a very important assumption that the nuclei of the atoms are fixed in space, which constitutes the *clamped nuclei approximation*. This assumption is valid due to the fact that the typical masses of nuclei are orders of magnitude larger than those of electrons. The kinetic energy associated with the motion of nuclei is thus much smaller than the kinetic energy of electrons, especially at low temperatures. In this thesis, all electronic properties of graphene nanoribbons are assessed at zero temperature, so we will adopt the clamped nuclei approximation from now on. The Hamiltonian written in the atomic units then takes the form

$$\hat{H} = -\sum_i \frac{\nabla_i^2}{2} - \sum_{i,J} \frac{Z_J}{|\mathbf{r}_i - \mathbf{R}_J|} + \frac{1}{2}\sum_{i,j\neq i} \frac{1}{|\mathbf{r}_i - \mathbf{r}_j|}, \tag{2.6}$$

where we also omitted the term describing the repulsion between nuclei, since this term is now constant. The energy E of the system should now be viewed as the actual energy of the system minus the Coulomb repulsion energy of the nuclei. We can re-write this Hamiltonian in a slightly more convenient form by defining the external potential originating from the nuclei of atoms as

$$V_{\mathrm{n}}(\mathbf{r}) = -\sum_J \frac{Z_J}{|\mathbf{r} - \mathbf{R}_J|}. \tag{2.7}$$

We then obtain the following Hamiltonian describing a system of N electrons in the electric field of nuclei:

$$\hat{H} = -\sum_i \frac{\nabla_i^2}{2} + \sum_i V_{\mathrm{n}}(\mathbf{r}_i) + \frac{1}{2}\sum_{i,j\neq i} \frac{1}{|\mathbf{r}_i - \mathbf{r}_j|}. \tag{2.8}$$

The first two terms in this Hamiltonian represent the sums of the kinetic energies of individual electrons and the potential energies of their attraction to the nuclei of the material. If we define a single-electron Hamiltonian as

$$\hat{H}_0(\mathbf{r}) = -\frac{\nabla^2}{2} + V_{\mathrm{n}}(\mathbf{r}), \tag{2.9}$$

the Hamiltonian of the system of N electrons can be re-written as

$$\hat{H} = \sum_i \hat{H}_0(\mathbf{r}_i) + \frac{1}{2}\sum_{i,j\neq i} \frac{1}{|\mathbf{r}_i - \mathbf{r}_j|}. \tag{2.10}$$

If this expression did not involve the electron-electron repulsion term, the time-independent Schrödinger equation could be easily solved as a system of N independent electrons in the

electric field of atomic nuclei. Due to the electron-electron repulsion term in the Hamiltonian, however, the motion of all electrons becomes correlated and it is not possible to describe the material using single-electron wavefunctions. The potential energy of electron-electron repulsion is comparable to the other terms in the Hamiltonian, so it cannot be ignored or treated as a perturbation. This mean that the Schrödinger equation with Hamiltonian (2.8) needs to be solved simultaneously for all N electrons.

The many-body Schrödinger equation can in principle be solved, which would yield a set of wavefunctions $\Psi(\mathbf{r}_1, \mathbf{r}_2, \ldots, \mathbf{r}_N)$, which depend on the coordinates of all N electrons of the material. In practice, numerical treatment of this problem is extremely complicated due to very high dimensionality of the many-body wavefunction for any large N. In the words of Paul Dirac [106]:

> "The underlying physical laws necessary for the mathematical theory of a large part of physics and the whole of chemistry are thus completely known, and the difficulty is only that the exact application of these laws leads to equations much too complicated to be soluble."

Numerous computational methods have been developed to facilitate the solution of the many-body Schrödinger equation by adopting various levels of simplifications.

2.2 Density functional theory

2.2.1 Hohenberg-Kohn theorem

Density functional theory (DFT) is the most successful version of a number of attempts to derive a rigorous density-based approach to the problem of many-body electronic systems. Instead of describing the state of a quantum system by its wavefunctions $\Psi(\mathbf{r}_1, \mathbf{r}_2, \ldots, \mathbf{r}_N)$, dependent on the individual coordinates of all electrons, it focuses on the electron density, defined as

$$\rho(\mathbf{r}) = N \int |\Psi(\mathbf{r}, \mathbf{r}_2, \ldots, \mathbf{r}_N)|^2 \, \mathrm{d}\mathbf{r}_2 \ldots \mathrm{d}\mathbf{r}_N. \tag{2.11}$$

If $\Psi(\mathbf{r}_1, \mathbf{r}_2, \ldots, \mathbf{r}_N)$ is properly normalised, then the electron density obeys

$$\int \rho(\mathbf{r}) \, \mathrm{d}\mathbf{r} = N. \tag{2.12}$$

Unlike the many-body wavefunction, the electron density depends only on one spatial coordinate $\mathbf{r}$, greatly simplifying computations involving it. The physical meaning of the electron density is also straightforward: up to the charge of electron, $\rho(\mathbf{r})$ is the density of electric charge that can be physically measured in materials via, for example, scanning tunnelling microscopy.

The key premise of DFT is the Hohenberg-Kohn theorem, which states that the energy of *the ground state* of a material, E_0, can be calculated exactly if the electron density in the ground state, $\rho_0(\mathbf{r})$, is known. In other words, the ground-state energy is a *functional* of the ground-state electron density:

$$E_0 = F[\rho_0]. \tag{2.13}$$

This is a highly nontrivial statement as in general, the energy of an arbitrary quantum state is calculated using the exact many-body wavefunction of said state. Only in the case of the ground state is it possible to prove rigorously that its electron density is sufficient to calculate its energy.

The proof of the Hohenberg-Kohn theorem goes as follows. First we note that the energy of any quantum state can be calculated exactly knowing the many-body wavefunction of that state,

$$E = \langle \Psi | \hat{H} | \Psi \rangle, \tag{2.14}$$

so there is a unique mapping of the form $\Psi \to E$. The wavefunction of any energy eigenstate is a solution to the Schrödinger equation with a given external potential V_n [see Eq. (2.7)]. The exact form of V_n thus determines the many-body wavefunction of the system in a unique way, $V \to \Psi$.

We shall now prove that the ground-state electron density ρ_0 of the system determines uniquely the external potential V_n. For this, we shall first assume the opposite to be true, that is, that two different external potentials V_n and V_n' can lead to the same ground-state electron density ρ_0. For the sake of convenience, we denote

$$\hat{T} = -\sum_i \frac{\nabla_i^2}{2} \tag{2.15}$$

and

$$\hat{W} = \frac{1}{2} \sum_{i,j \neq i} \frac{1}{|\mathbf{r}_i - \mathbf{r}_j|} \tag{2.16}$$

and define the Hamiltonians for the two external potentials as

$$\hat{H} = \hat{T} + \hat{W} + V_{\mathrm{n}}(\mathbf{r}), \tag{2.17a}$$

$$\hat{H}' = \hat{T} + \hat{W} + V'_{\mathrm{n}}(\mathbf{r}). \tag{2.17b}$$

We also denote the ground-state many-body wavefunctions corresponding to the two external potentials V_{n} and V'_{n} as Ψ_0 and Ψ'_0, respectively. The ground-state energies in the two cases are then equal to

$$E_0 = \langle\Psi_0|\hat{H}|\Psi_0\rangle = \langle\Psi_0|\hat{T} + \hat{W}|\Psi_0\rangle + \int V_{\mathrm{n}}(\mathbf{r})\rho_0(\mathbf{r})\mathrm{d}\mathbf{r}, \tag{2.18a}$$

$$E'_0 = \langle\Psi'_0|\hat{H}'|\Psi'_0\rangle = \langle\Psi'_0|\hat{T} + \hat{W}|\Psi'_0\rangle + \int V'_{\mathrm{n}}(\mathbf{r})\rho_0(\mathbf{r})\mathrm{d}\mathbf{r}, \tag{2.18b}$$

where we used Eq. (2.11) to replace the summation over all electrons with the integration over the electron density.

Since Ψ_0 is not the ground state of $\hat{H}'$ and, similarly, Ψ'_0 is not the ground state of $\hat{H}$, we have strict inequalities

$$\langle\Psi_0|\hat{H}'|\Psi_0\rangle > E'_0, \tag{2.19a}$$

$$\langle\Psi'_0|\hat{H}|\Psi'_0\rangle > E_0. \tag{2.19b}$$

By combining Eqs. (2.17) and (2.18), we obtain

$$\langle\Psi_0|\hat{T} + \hat{W}|\Psi_0\rangle + \int V'_n(\mathbf{r})\rho_0(\mathbf{r})\mathrm{d}\mathbf{r} > \langle\Psi'_0|\hat{T} + \hat{W}|\Psi'_0\rangle + \int V'_n(\mathbf{r})\rho_0(\mathbf{r})\mathrm{d}\mathbf{r}, \tag{2.20a}$$

$$\langle\Psi'_0|\hat{T} + \hat{W}|\Psi'_0\rangle + \int V_{\mathrm{n}}(\mathbf{r})\rho_0(\mathbf{r})\mathrm{d}\mathbf{r} > \langle\Psi_0|\hat{T} + \hat{W}|\Psi_0\rangle + \int V_{\mathrm{n}}(\mathbf{r})\rho_0(\mathbf{r})\mathrm{d}\mathbf{r}. \tag{2.20b}$$

We then add up the two inequalities and get rid of the terms involving $\hat{T}$ and $\hat{W}$, yielding

$$\int [V_{\mathrm{n}}(\mathbf{r}) + V'_n(\mathbf{r})]\rho_0(\mathbf{r})\mathrm{d}\mathbf{r} > \int [V_{\mathrm{n}}(\mathbf{r}) + V'_n(\mathbf{r})]\rho_0(\mathbf{r})\mathrm{d}\mathbf{r} \tag{2.21}$$

or $0 > 0$. This is a clear contradiction, meaning that the initial assumption that two different external potentials can result in the same ground-state electron density is incorrect.

We have thus shown that the electron density of the ground state has a unique correspondence with the external potential of the system, $\rho_0 \to V_{\mathrm{n}}$. By combining all of the above statements together, we find that

$$\rho_0 \to V_{\mathrm{n}} \to \Psi_0 \to E_0. \tag{2.22}$$

Therefore, the ground-state electron density ρ_0 has a unique mapping to the energy of the ground state E_0. Note that the proof of the Hohenberg-Kohn theorem relies on the fact that the ground state of a given system has the lowest energy compared to all other states [see Eqs. (2.19)]. Energies of excited states cannot be determined from knowing the electron density ρ_0 alone and require the many-body wavefunctions Ψ. Several extensions of classical DFT such as the time-dependent DFT and many-body perturbation methods have been developed to address this problem. They often rely on the solution provided by DFT as a starting point for obtaining reasonable approximations of the wavefunctions of the excited states.

Even though traditional DFT can only be used to compute ground-state energies of materials, this is sufficient for many practical purposes. In particular, DFT can be used to compute formation energies of molecules and crystals by comparing their ground-state energies to the energies of isolated atoms. DFT is also used to determine the most stable configuration of a material, which is achieved by adjusting the atomic positions and the lattice parameters of periodic materials until the lowest ground-state energy is achieved. It is also possible to assess the vibrational and elastic properties of materials by tracking the changes in their ground-state energy upon the displacement of atoms from their equilibrium positions.

Most importantly, the studies reported in this thesis rely on DFT in the calculations of the band structures of graphene nanoribbons. The knowledge of the band structures provides important insights into the conduction properties of graphene nanoribbons: whether they are insulating or conducting, how they respond to external electric fields, and how their conductivity changes upon the application of lattice strain. While it is not possible to use DFT to assess optical excitations of materials, the last chapter of this thesis relies on reasonable semi-empirical approximations to calculate the optical spectra of graphene nanoribbons.

2.2.2 Kohn-Sham equations

It was thus established that the ground-state energy of a material is a functional of the ground-state electron density, $E = F[\rho]$. However, the exact form of this functional is still unknown. Modern DFT relies on a series of very useful approximations to express the ground-state energy as a functional of ρ. A good starting point is the Hartree-Fock approximation, which states that all electrons in the system are *independent*. In that case, it would be very

tempting to write the many-body wavefunction as a product of single-electron wavefunctions:

$$\Psi(\mathbf{r}_1, \mathbf{r}_2, \ldots, \mathbf{r}_N) = \phi_1(\mathbf{r}_1)\phi_2(\mathbf{r}_2)\ldots\phi_N(\mathbf{r}_N), \tag{2.23}$$

where $\phi_i(\mathbf{r})$ is the single-electron wavefunction corresponding to the ith electron. However, according to the Pauli exclusion principle, all electrons are indistinguishable, and the many-body wavefunction should change sign upon the exchange of any two electrons, e.g., $\Psi(\mathbf{r}_1, \mathbf{r}_2, \ldots, \mathbf{r}_N) = -\Psi(\mathbf{r}_2, \mathbf{r}_1, \ldots, \mathbf{r}_N)$. To satisfy this requirement, the many-body wavefunction is approximated by the Slater determinant:

$$\Psi(\mathbf{r}_1, \mathbf{r}_2, \ldots, \mathbf{r}_N) = \frac{1}{\sqrt{N!}} \begin{vmatrix} \phi_1(\mathbf{r}_1) & \phi_1(\mathbf{r}_2) & \ldots & \phi_1(\mathbf{r}_N) \\ \phi_2(\mathbf{r}_1) & \phi_2(\mathbf{r}_2) & \ldots & \phi_2(\mathbf{r}_N) \\ \vdots & \vdots & \ddots & \vdots \\ \phi_N(\mathbf{r}_1) & \phi_N(\mathbf{r}_2) & \ldots & \phi_N(\mathbf{r}_N) \end{vmatrix}. \tag{2.24}$$

The electron density of such a many-body state is calculated by adding the probability densities of all individual electrons:

$$\rho(\mathbf{r}) = \sum_i |\phi_i(\mathbf{r})|^2. \tag{2.25}$$

The total energy of the system is found by evaluating $\langle\Psi|\hat{H}|\Psi\rangle$, where $\hat{H}$ is the same Hamiltonian as in Eq. (2.8). After some extensive algebra, this leads to:

$$E = -\sum_i \int \phi_i^*(\mathbf{r})\frac{\nabla_i^2}{2}\phi_i(\mathbf{r})\,\mathrm{d}\mathbf{r} + \int V_\mathrm{n}(\mathbf{r})\rho(\mathbf{r})\mathrm{d}\mathbf{r} + \frac{1}{2}\int V_\mathrm{H}(\mathbf{r})\rho(\mathbf{r})\mathrm{d}\mathbf{r} + \frac{1}{2}\sum_i \iint \phi_i^*(\mathbf{r})V_\mathrm{X}(\mathbf{r},\mathbf{r}')\phi_i(\mathbf{r}')\,\mathrm{d}\mathbf{r}\,\mathrm{d}\mathbf{r}'. \tag{2.26}$$

It is seen that the electron-electron repulsion term found in Eq. (2.8) has been transformed into two different contributions. The first of the two new terms in Eq. (2.26) corresponds to the energy of electrons in the so-called Hartree potential, which is obtained from the classical Poisson equation of the form

$$\nabla^2 V_\mathrm{H}(\mathbf{r}) = -\rho(\mathbf{r}). \tag{2.27}$$

The solution to this equation is

$$V_\mathrm{H}(\mathbf{r}) = \int \frac{\rho(\mathbf{r}')}{|\mathbf{r}-\mathbf{r}'|}\,\mathrm{d}\mathbf{r}'. \tag{2.28}$$

In simpler terms, the Hartree potential describes the mean electrostatic field produced by the total electron density at each coordinate $\mathbf{r}$. This potential, commonly introduced within the

mean-field approximation, quantifies the repulsion of each electron from the average density of all other electrons. The last term in Eq. (2.26) is the exchange energy with the corresponding potential given by

$$V_{\mathrm{X}}(\mathbf{r},\mathbf{r}') = -\sum_j \frac{\phi_j^*(\mathbf{r}')\phi_j(\mathbf{r})}{|\mathbf{r}-\mathbf{r}'|}. \tag{2.29}$$

This potential describes the energy of exchanging two electrons in space and appears exclusively due to the quantum nature of electrons, captured by the Slater determinant in Eq. (2.24).

The expression for the total energy of the many-body system that was obtained in Eq. (2.26) has two critical issues. First, the exchange interaction $V_{\mathrm{X}}(\mathbf{r},\mathbf{r}')$ is *non-local*, in the sense that the energy of an electron in this potential depends not only on the value of the potential at the electron's position but on the values of the potential in the entire space. This makes the computation of the exchange energy of many-body systems extremely difficult. The second problem is that the total energy in Eq. (2.26) was calculated with the assumption that electrons are independent, which is not truly the case. It is intuitive that due to the Coulomb repulsion, the probability of finding an electron at some point in space decreases if another electron is found nearby, $|\Psi(\mathbf{r}_1,\mathbf{r}_2)|^2 < |\phi_1(\mathbf{r}_1)\phi_2(\mathbf{r}_2)|^2$. In other terms, the motion of electrons is *correlated*. There is thus a difference between the true energy of the many-body system and the energy calculated using Eq. (2.26), which is called the correlation energy.

For the above reasons, the total energy of the many-body system in DFT is commonly written as

$$E = -\sum_i \int \phi_i^*(\mathbf{r})\frac{\nabla_i^2}{2}\phi_i(\mathbf{r})\,\mathrm{d}\mathbf{r} + \int V_{\mathrm{n}}(\mathbf{r})\rho(\mathbf{r})\mathrm{d}\mathbf{r} + \frac{1}{2}\int V_{\mathrm{H}}(\mathbf{r})\rho(\mathbf{r})\mathrm{d}\mathbf{r} + E_{\mathrm{xc}}[\rho], \tag{2.30}$$

where $E_{\mathrm{xc}}[\rho]$ is some unknown functional corresponding to the exchange and correlation energies of electrons. In simple terms, the exchange-correlation functional $E_{\mathrm{xc}}[\rho]$ is the remainder that arises from assuming that electrons are independent and ignoring the quantum exchange.

The question is now how to find the ground-state electron density ρ_0. By definition, this is exactly the electron density that minimises the total energy of the system $E = F[\rho]$ and can thus be found using the variational principle as

$$\left.\frac{\delta F}{\delta \rho}\right|_{\rho_0} = 0. \tag{2.31}$$

Applying this variational principle to Eq. (2.30) yields the following set of single-electron equations:

$$\left[-\frac{1}{2}\nabla^2 + V_{\mathrm{n}}(\mathbf{r}) + V_{\mathrm{H}}(\mathbf{r}) + V_{\mathrm{xc}}(\mathbf{r})\right]\phi_i(\mathbf{r}) = \varepsilon_i\phi_i(\mathbf{r}), \tag{2.32}$$

where the exchange-correlation potential is given by

$$V_{\mathrm{xc}}(\mathbf{r}) = \left.\frac{\delta E_{\mathrm{xc}}}{\delta\rho}\right|_{\rho_0(\mathbf{r})}. \tag{2.33}$$

Equations (2.32) are called the Kohn-Sham equations. Their solution yields a set of the Kohn-Sham wavefunctions $\phi_i(\mathbf{r})$ and the corresponding energies ε_i. The total energy of the system can be then found as the sum of single-electron energies:

$$E = \varepsilon_1 + \varepsilon_2 + \cdots + \varepsilon_N. \tag{2.34}$$

It is important to understand that the Kohn-Sham states do not describe actual isolated electrons. They are auxiliary functions that are used to facilitate the solution of the many-body Schrödinger equation. However, they can often be interpreted as effective single-electron states that mimic the behaviour of electrons in the presence of an effective potential.

2.3 Solving the Kohn-Sham equations

2.3.1 Self-consistent calculations

The Kohn-Sham equations (2.32) form the foundational framework of density functional theory. These equations offer a pathway to theoretically derive single-electron wavefunctions, $\phi_i(\mathbf{r})$, and determine essential properties like the total energy E and electron density $\rho(\mathbf{r})$ for a given material. However, the practical implementation of DFT within computational codes involves various considerations, including the selection of appropriate exchange-correlation functionals and representations of Kohn-Sham wavefunctions. This section aims to provide a brief overview of these practical aspects of DFT, explaining the rationale behind the computational methods employed in the subsequent chapters.

However, we first need to comment on a general computational approach that is used in DFT calculations. We note that both the Hartree potential $V_{\mathrm{H}}(\mathbf{r})$ and the exchange-correlation potential $V_{\mathrm{xc}}(\mathbf{r})$ depend on the electron density $\rho(\mathbf{r})$, which, in turn, is determined by the

Kohn-Sham wavefunctions $\phi_i(\mathbf{r})$. The Kohn-Sham equations (2.32) thus need to be solved in a self-consistent manner. This means that if we use the wavefunctions $\phi_i(\mathbf{r})$ to calculate the electron density $\rho(\mathbf{r})$ and use it determine the Hartree and exchange-correlation potentials, the resulting Kohn-Sham equations should produce the same Kohn-Sham wavefunctions $\phi_i(\mathbf{r})$.

In practice, self-consistent calculations proceed as follows: the positions of the nuclei are specified, typically based on experimental crystal structures obtained via X-ray diffraction. An initial approximation of the electron density $\rho(\mathbf{r})$ is then chosen, often assuming electrons are localized in atomic orbitals of non-interacting atoms. This initial electron density is used to compute the Hartree and exchange-correlation potentials, and the Kohn-Sham equations are solved. The resulting wavefunctions are used to update the electron density, which is compared to the initial guess. This process iterates until the difference between successive electron densities becomes smaller than a predefined tolerance threshold, indicating self-consistency.

2.3.2 Exchange-correlation functionals

One of the main roadblocks in DFT is the fact that the exact form of the exchange-correlation functional $E_{\mathrm{xc}}[\rho]$ is not known. A practical question is thus how to approximate $E_{\mathrm{xc}}[\rho]$ in a way that is both easy to compute and sufficiently accurate. The simplest approach is the local density approximation (LDA), which assumes that the exchange-correlation energy of a small volume $\mathrm{d}\mathbf{r}$, characterised by the electron density $\rho(\mathbf{r})$, is equal to the exchange-correlation energy density of a homogeneous electron gas (HEG) of the same density, $\epsilon_{\mathrm{xc}}^{\mathrm{HEG}}[\rho(\mathbf{r})]$, times the number of electrons in the unit volume, $\rho(\mathbf{r})\mathrm{d}\mathbf{r}$. The exchange-correlation energy of the entire material is then found by adding up the individual contributions from unit volumes:

$$E_{\mathrm{xc}}[\rho] = \int \rho(\mathbf{r})\epsilon_{\mathrm{xc}}^{\mathrm{HEG}}[\rho(\mathbf{r})]\,\mathrm{d}\mathbf{r}. \tag{2.35}$$

Importantly, the LDA assumes that the exchange-correlation energy density at a given point in space depends only on the local electron density at that point. The advantage of this approximation is that both the exchange and correlation energies of the HEG can be computed very accurately, leading to explicit expressions for $E_{\mathrm{xc}}[\rho]$. The LDA is capable of providing reasonable predictions for lattice constants and elastic properties of materials, but can underestimate their band gaps. It is also not well suited for describing strongly correlated systems.

The generalised gradient approximation (GGA) extends the idea behind the LDA by taking into account the gradient, $\nabla\rho(\mathbf{r})$, of the electron density at each point. The exchange-correlation energy of the system is then given by

$$E_{\mathrm{xc}}[\rho] = \int \rho(\mathbf{r})\epsilon_{\mathrm{xc}}[\rho(\mathbf{r}), \nabla\rho(\mathbf{r})]\,\mathrm{d}\mathbf{r}, \tag{2.36}$$

where the exact form of the exchange-correlation energy density $\epsilon_{\mathrm{xc}}[\rho(\mathbf{r}), \nabla\rho(\mathbf{r})]$ depends on a particular GGA functional. GGA functionals give good results for a wide range of materials, including metals, semiconductors, and insulators. As in the case of the LDA, the GGA tends to underestimate band gaps. A common GGA functional is the Perdew-Burke-Ernzerhof (PBE) exchange-correlation functional, which provides a good trade-off between computational costs and the accuracy of predictions for solids [107]. For these reasons, the DFT calculations reported in the following chapters rely on the PBE exchange-correlation functional to produce the key results of this thesis.

2.3.3 Frozen core approximation and pseudopotentials

In chemistry, it is widely known that chemical bonding occurs primarily through the outermost electrons of atoms, while the inner atomic orbitals remain relatively unaffected by neighboring atoms. In electronic structure calculations, this insight allows us to simplify our approach by focusing solely on the valence electrons of constituent species, leaving the core electrons unchanged from their isolated atomic states. For instance, when calculating the electronic band structures of graphene nanoribbons, it is possible to achieve remarkable accuracy by considering only the $2s$ and $2p$ orbitals of carbon, while treating the $1s$ electrons as a part of the atomic nucleus. This simplification, known as the *frozen core approximation*, significantly reduces the computational costs of DFT calculations, making DFT widely applicable across materials science.

The process of removing core electrons from the Kohn-Sham equations requires careful consideration. Valence electrons, if they are characterised by principal quantum numbers $n \geq 2$, which is the case in all atoms other than H and He, exhibit rapid oscillations near the nucleus in order to achieve zero overlap with the core electron wavefunctions. Capturing these oscillatory behaviors in DFT calculations would require sampling the Kohn-Sham states on a very dense grid of real-space points, leading to high computational costs. To address

this challenge, a common approach involves replacing the actual wavefunctions of valence electrons with *pseudized* counterparts characterised by a cutoff radius r_{c}. These pseudized wavefunctions match the true wavefunctions for $r \geq r_{\mathrm{c}}$ but are smoothly tapered towards the nucleus for $r < r_{\mathrm{c}}$. In practice, core electrons are considered together with the nucleus as a part of an ionic core, whose charge is smaller than the charge of the nucleus due to screening. The actual Coulomb potential of the atomic nucleus is replaced with a *pseudopotential*, constructed in a such way that it mimics some of the scattering properties of the original nucleus [108]. The pseudopotential is carefully tailored to ensure that the Kohn-Sham equations yield accurate energies and pseudized wavefunctions for the valence electrons.

2.3.4 Planewave basis set

The final part to address is how to solve the Kohn-Sham equations (2.32) and obtain the set of single-electron wavefunctions $\phi_i(\mathbf{r})$ and energies ε_i for a given material. For convenience, we re-write the Kohn-Sham equations in a short form as

$$\left[-\frac{1}{2}\nabla^2 + V(\mathbf{r})\right]\phi_i(\mathbf{r}) = \varepsilon_i\phi_i(\mathbf{r}), \tag{2.37}$$

where

$$V(\mathbf{r}) = V_{\mathrm{n}}(\mathbf{r}) + V_{\mathrm{H}}(\mathbf{r}) + V_{\mathrm{xc}}(\mathbf{r}) \tag{2.38}$$

is the sum of the external potential energy due to the electric field of nuclei, $V_{\mathrm{n}}(\mathbf{r})$, the Hartree potential due to the classical electron-electron repulsion, $V_{\mathrm{H}}(\mathbf{r})$, and the potential due to the quantum exchange and correlation, $V_{\mathrm{xc}}(\mathbf{r})$.

In the context of periodic materials, the Bloch theorem is a fundamental concept used to describe the behavior of electrons within a crystal lattice. According to the Bloch theorem, the Kohn-Sham wavefunctions can be expressed as a product of a plane wave factor and a periodic Bloch amplitude:

$$\phi_{i\mathbf{k}}(\mathbf{r}) = e^{i\mathbf{k}\cdot\mathbf{r}}u_{i\mathbf{k}}(\mathbf{r}), \tag{2.39}$$

where i labels energy bands (not to be confused with the imaginary unit in the exponent), $\mathbf{k}$ is the wavevector of the electron, and $u_{i\mathbf{k}}(\mathbf{r})$ is the Bloch amplitude, which shares the same periodicity as the crystal lattice. Substituting Eq. (2.39) into the Kohn-Sham equations (2.37), we arrive at a set of equations that involve the adjusted kinetic energy operator and the

effective potential acting on the Bloch amplitude:

$$\left[-\frac{1}{2}(\nabla + i\mathbf{k})^2 + V(\mathbf{r})\right] u_{i\mathbf{k}}(\mathbf{r}) = u_{i\mathbf{k}}(\mathbf{r}). \tag{2.40}$$

These equations must be solved for all values of electron wavevector $\mathbf{k}$. Owing to the periodicity of the material, we can focus on the $\mathbf{k}$-values in the first Brillouin zone (BZ), which is the unit cell of the material in the reciprocal space. In practical calculations, $u_{i\mathbf{k}}(\mathbf{r})$ are computed on a discrete grid of $\mathbf{k}$-points sampled within the BZ of the material. The density of $\mathbf{k}$-points is increased until convergence of the physical properties of interest is achieved.

A natural way to further exploit the periodicity of crystalline materials is to represent the Bloch amplitude $u_{i\mathbf{k}}(\mathbf{r})$ as a superposition of the planewaves:

$$u_{i\mathbf{k}}(\mathbf{r}) = \sum_{\mathbf{G}} c_{i\mathbf{k}}(\mathbf{G}) \exp\left(i\mathbf{G}\cdot\mathbf{r}\right), \tag{2.41}$$

where the summation is performed over all reciprocal lattice vectors $\mathbf{G}$. For an arbitrary crystal lattice vector $\mathbf{R}$, we have $e^{i\mathbf{G}\cdot\mathbf{R}} = 1$, ensuring the periodicity of the Bloch amplitude defined by Eq. (2.41). The planewave representation thus automatically takes into account the periodicity of the crystal. In theory, the sum in Eq. (2.41) contains an infinite number of planewaves and reproduces the Kohn-Sham wavefunction exactly. In practice, the number of planewaves needs to be restricted to ensure that the problem can be treated numerically. The total number of planewaves $N_{\mathbf{G}}$ included in the sum controls the resulting resolution of the Kohn-Sham wavefunction in real space as $\Delta r \sim a/N_{\mathbf{G}}^{1/3}$, where a is the periodic length of the crystal. The planewaves are typically selected based on the *planewave kinetic energy cutoff*. We only include the planewaves with such $\mathbf{G}$ that

$$\frac{|\mathbf{G}|^2}{2} \leq E_{\text{cut}}, \tag{2.42}$$

where E_{cut} is the cutoff energy. Substituting the plane-wave representation into Eq. (2.40), we arrive at the following set of equations for $c_{i\mathbf{k}}(\mathbf{G})$:

$$\frac{|\mathbf{G}+\mathbf{k}|^2}{2} c_{i\mathbf{k}}(\mathbf{G}) + \sum_{\mathbf{G}'} v(\mathbf{G}-\mathbf{G}') c_{i\mathbf{k}}(\mathbf{G}') = \varepsilon_{i\mathbf{k}} c_{i\mathbf{k}}(\mathbf{G}), \tag{2.43}$$

where

$$v(\mathbf{G}) = \frac{1}{a^3}\int \exp\left(-i\mathbf{G}\cdot\mathbf{r}\right) V(\mathbf{r})\,\mathrm{d}\mathbf{r}. \tag{2.44}$$

The Kohn-Sham equations are thus solved in the reciprocal space for coefficients $c_i(\mathbf{G})$, which can then be used to restore the real-space representation of the Kohn-Sham wavefunctions.

It is essential to recognise that DFT in the planewave representation is designed for materials exhibiting periodicity in all three spatial dimensions. However, graphene nanoribbons, while extending infinitely in one direction, possess finite width and thickness, which poses some challenge for their computational modelling with DFT. It is still possible to employ a planewave basis set by defining a sufficiently large bounding box in the two non-periodic dimensions of the nanoribbon. This effectively transforms the system into a periodic array of repeated graphene nanoribbons. Given an adequate separation in these non-periodic directions, this approach yields accurate results, effectively replicating the electronic states of an isolated graphene nanoribbon. DFT calculations utilising planewave representations are supported by various computational tools, offering a robust framework for studying periodic materials. In particular, the first-principles calculations reported in Chapter 3 of this thesis rely on the open-source computational package `Quantum ESPRESSO` [109, 110].

2.3.5 Spin-polarised calculations

In the preceding chapter, we discussed the magnetic phases arising in certain graphene nanoribbons from an imbalance in the densities of spin-up and spin-down electrons. Spin, being a relativistic quantity, should ideally be described through the Dirac equation rather than the Schrödinger equation, which has been our primary focus thus far. However, graphene, composed of lightweight carbon atoms, exhibits negligible relativistic effects, rendering the Schrödinger equation adequate for most purposes. For instance, the energy associated with spin-orbit coupling in monolayer graphene is on the order of μeV, which can be safely ignored in most practical considerations.

The magnetization observed in graphene nanostructures primarily originates from electron-electron repulsion between spin-polarized electron densities. This magnetization can be effectively probed through spin-polarized DFT calculations. A straightforward approach involves introducing two sets of Kohn-Sham states, each corresponding to opposite spin orientations, denoted as $\phi_{i\sigma}(\mathbf{r})$, with corresponding spin-dependent energies $\varepsilon_{i\sigma}$. In the absence of spin-orbit coupling or other relativistic effects, energy bands associated with different spin directions are coupled through the Hartree and exchange-correlation potentials. The electron

densities for spin-up and spin-down states, defined as

$$\rho_\sigma(\mathbf{r}) = \sum_i |\phi_{i\sigma}(\mathbf{r})|^2, \tag{2.45}$$

can be different, producing magnetic moments. This local magnetization is conveniently described by the spin density, defined as the difference between spin-up and spin-down electron densities:

$$\Delta\rho(\mathbf{r}) = \rho_\uparrow(\mathbf{r}) - \rho_\downarrow(\mathbf{r}). \tag{2.46}$$

The key to performing spin-polarised DFT calculations is the choice of an exchange-correlation functional explicitly accounting for the spin polarisation of electrons, such as the local spin density approximation (LSDA).

2.3.6 External electric fields

Later chapters will focus on the effects of external electric fields on graphene nanoribbons. An external electric field, denoted as $\mathbf{F}$, can be introduced into DFT calculations as a perturbative potential of the form:

$$V_{\text{ext}}(\mathbf{r}) = \mathbf{F} \cdot \mathbf{r}. \tag{2.47}$$

One challenge with this potential is its non-periodicity. When the external field is applied along finite directions of the graphene nanoribbon (i.e., across the nanoribbon or perpendicular to its plane), a straightforward workaround is to introduce a sawtooth potential, depicted in Figure 2.1. Within the nanoribbon region, this potential increases linearly as described by Eq. (2.47). Meanwhile, in the vacuum regions between periodic copies of the nanoribbon, the potential rapidly decreases to ensure periodicity across the supercells.

An issue that may arise with this approach is the formation of potential wells in the vacuum regions between supercells. In the presence of a strong electric field, electrons from the graphene nanoribbon may tunnel into these potential wells. This phenomenon is particularly problematic in DFT calculations using plane wave basis sets, as plane waves are defined not only within the material volume but across the entire supercell. To mitigate electron tunneling, it is crucial to increase the size of the supercell for strong electric fields. However, this inevitably extends computational time. To address this challenge, the DFT calculations in Chapters 4 and 5 of this thesis utilise localised basis sets, implemented in the `SIESTA` com-

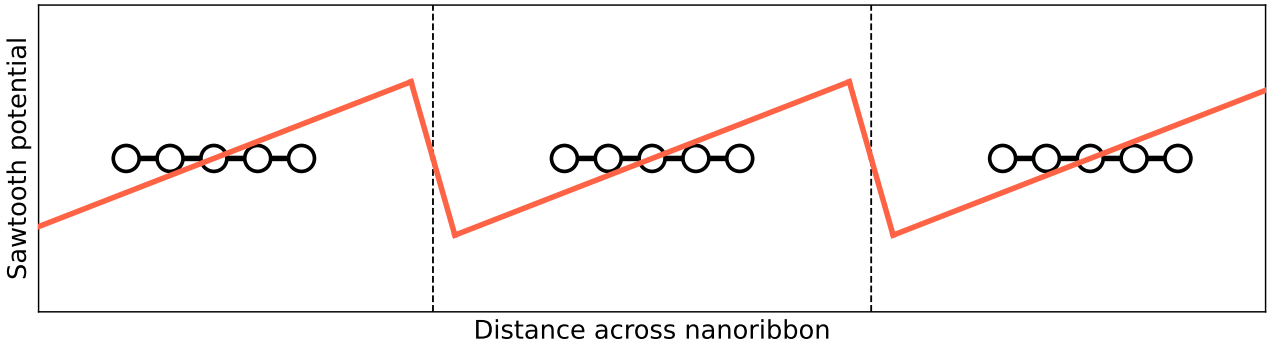


Figure 2.1: Sawtooth potential (the red line) used in DFT calculations to model the effect of an external electric field. The dashed vertical lines show the boundaries of supercells. The supercells contain periodic copies of graphene nanoribbons, shown in their cross-section.

putational package [111]. The theory behind localised basis functions will be discussed in detail in the following section.

2.4 Tight-binding approximation

2.4.1 Localised basis set

While density functional theory calculations provide highly accurate results for the ground-state properties of materials, they are computationally expensive and can also suffer from poor interpretability. In a sense, *ab initio* calculations are not much different from measurements performed on real materials and can be viewed as experiments *in silico*. Various semi-empirical methods have been developed in order to simplify electronic structure calculations and gain insights into the physics behind the observed phenomena. In the case of graphene nanostructures, the most popular such method is the tight-binding approximation for π-electrons.

Tight-binding models and various other semi-empirical approaches rely on the usage of localised basis sets, which are well suited for describing materials with strongly localised electrons. In these approximations, electrons are assumed to be tightly bound (hence the name of the approximation) to specific atomic sites. The interaction between atoms occurs mainly in the form of electrons hopping between neighbouring lattice sites. The usage of localised basis sets relies on the fact that the solution of the Kohn-Sham equations for isolated

atoms is known. The Kohn-Sham wavefunctions are then written as linear combinations of atomic-like orbitals (LCAO):

$$\phi_i(\mathbf{r}) = \sum_{\nu,\mathbf{R}} c_{i\nu\mathbf{R}}\varphi_{\nu\mathbf{R}}(\mathbf{r}), \tag{2.48}$$

where $\varphi_{\nu\mathbf{R}}(\mathbf{r}) = \varphi_\nu(\mathbf{r}-\mathbf{R})$ is the wavefunction of the νth atomic orbital in an isolated atom at position $\mathbf{R}$.

In general, this expansion spans multiple atomic orbitals on each atom, allowing researchers to tailor the basis set according to their specific needs. DFT calculations using a localised basis set typically incorporate all valence orbitals of constituent atoms, along with certain excited states. Semi-empirical approximations, on the other hand, focus on a smaller subset of atomic orbitals capable of reproducing the desired material properties accurately. The low-energy excitations in graphene arise predominantly from the p_z-electrons of carbon atoms. Hence, in the tight-binding approximation for graphene, it suffices to include only the p_z-orbitals in the LCAO expansion.

By substituting Eq. (2.48) into the Kohn-Sham equations, we obtain

$$\sum_{\nu,\mathbf{R}} c_{i\nu\mathbf{R}}\left[-\frac{\nabla^2}{2} + V(\mathbf{r})\right]\varphi_{\nu\mathbf{R}}(\mathbf{r}) = \varepsilon_i \sum_{\nu,\mathbf{R}} c_{i\nu\mathbf{R}}\varphi_{\nu\mathbf{R}}. \tag{2.49}$$

We then multiply both parts of this equation by $\varphi^*_{\mu\mathbf{R}'}(\mathbf{r})$ and perform integration, obtaining

$$\sum_{\nu}(H_{\mu\mathbf{R}';\nu\mathbf{R}} - \varepsilon_i S_{\mu\mathbf{R}';\nu\mathbf{R}})c_{i\nu\mathbf{R}} = 0, \tag{2.50}$$

where

$$H_{\mu\mathbf{R}';\nu\mathbf{R}} = \int \varphi^*_{\mu\mathbf{R}'}(\mathbf{r})\left[-\frac{\nabla^2}{2} + V(\mathbf{r})\right]\varphi_{\nu\mathbf{R}}(\mathbf{r})\,\mathrm{d}\mathbf{r} \tag{2.51}$$

are the matrix elements of the Hamiltonian and

$$S_{\mu\mathbf{R}';\nu\mathbf{R}} = \int \varphi^*_{\mu\mathbf{R}'}(\mathbf{r})\varphi_{\nu\mathbf{R}}(\mathbf{r})\,\mathrm{d}\mathbf{r} \tag{2.52}$$

is the overlap matrix.

A series of simplifications can be made to Eq. (2.50) to facilitate its solution. First, we assume that the overlap between different atomic orbitals is zero:

$$S_{\mu\mathbf{R}';\nu\mathbf{R}} = \delta_{\mu\nu}\delta_{\mathbf{R}\mathbf{R}'}. \tag{2.53}$$

This approximation is justified if the atomic orbitals have a small overlap. This is the case, for example, for the p_z-orbitals in graphene, which are directed perpendicular to the direction

of chemical bonding. The approximation of negligible overlap is also justified if functions $\varphi_{\nu\mathbf{R}}(\mathbf{r})$ are processed to be orthogonal to each other. An example of such orthogonalised orbitals is the set of projected Wannier functions, defined as:

$$w_{\nu\mathbf{R}}(\mathbf{r}) = \frac{1}{\sqrt{N}} \sum_{\mathbf{k}} \phi_{\mathbf{k}}(\mathbf{r}) e^{-i\mathbf{k}\cdot\mathbf{R}}, \tag{2.54}$$

where N is the number of lattice sites in the crystal and $\phi_{\mathbf{k}}(\mathbf{r})$ are the Kohn-Sham wavefunctions. Functions (2.54) are localised at specific lattice sites just like atomic orbitals, but have oscillatory tails, ensuring zero overlap between the Wannier functions at different lattice sites. The latter can be easily proven by direct evaluation of the overlap integral:

$$\begin{aligned} S_{\mu\mathbf{R};\nu\mathbf{R}'} = \int w^*_{\mu\mathbf{R}}(\mathbf{r}) w_{\nu\mathbf{R}'}(\mathbf{r})\,\mathrm{d}\mathbf{r} &= \frac{1}{N} \sum_{\mathbf{k},\mathbf{k}'} e^{i\mathbf{k}\cdot\mathbf{R}} e^{-i\mathbf{k}'\cdot\mathbf{R}'} \int \phi^*_{\mathbf{k}}(\mathbf{r}) \phi_{\mathbf{k}'}(\mathbf{r})\,\mathrm{d}\mathbf{r} \\ &= \frac{1}{N} \sum_{\mathbf{k},\mathbf{k}'} e^{i\mathbf{k}\cdot\mathbf{R}} e^{-i\mathbf{k}'\cdot\mathbf{R}'} \delta_{\mathbf{k},\mathbf{k}'} = \frac{1}{N} \sum_{\mathbf{k}} e^{i\mathbf{k}\cdot(\mathbf{R}-\mathbf{R}')} = \delta_{\mathbf{R}\mathbf{R}'}. \end{aligned} \tag{2.55}$$

For this reason, Wannier functions represent a promising basis set for tight-binding calculations, which is why they are used in Chapter 3 of this thesis. With the assumption that the overlap between the atomic orbitals on different lattice sites is negligible, Eq. (2.50) simplifies to

$$\sum_{\nu,\mathbf{R}'} H_{\mu\mathbf{R};\nu\mathbf{R}'} c_{i\nu\mathbf{R}'} = \varepsilon_i c_{i\mu\mathbf{R}}, \tag{2.56}$$

which is just an eigenvalue problem solved by diagonalising the Hamiltonian matrix $H_{\mu\mathbf{R};\nu\mathbf{R}'}$.

2.4.2 Tight-binding Hamiltonian

Instead of evaluating the matrix elements of the Hamiltonian $H_{\mu\mathbf{R};\nu\mathbf{R}'}$ from the first principles, we adopt a semi-empirical approach and fit $H_{\mu\mathbf{R};\nu\mathbf{R}'}$ to either experimental or theoretical data. For instance, the diagonal elements of the Hamiltonian matrix are assumed to be equal to the energy levels of atomic orbitals in isolated atoms, $H_{\mu\mathbf{R};\mu\mathbf{R}} = \varepsilon_\mu$. These energies are known, for example, from ionization experiments. If all orbitals in the tight-binding Hamiltonian are the same, which is the case for the p_z-electrons in graphene, we can simply set $H_{\mu\mathbf{R};\mu\mathbf{R}} = 0$.

In order to approximate non-diagonal components of the Hamiltonian $H_{\mu\mathbf{R};\nu\mathbf{R}'}$, we note that atomic orbitals are strongly localised around the corresponding atoms, so it is fair to assume that the largest matrix elements $H_{\mu\mathbf{R};\nu\mathbf{R}'}$ are observed for the atoms that are close each other. It is not too uncommon to completely disregard the interactions between all atoms

but the nearest neighbours. This nearest-neighbour tight-binding approximation is capable of reproducing the key electronic properties of graphene, despite its apparent simplicity. In order to reproduce finer features of the electronic structure, it is however necessary to account for interactions between atoms that are further apart from each other, as will be demonstrated in Chapter 3 of this thesis.

A very simple approximation of the Hamiltonian matrix elements $H_{\mu\mathbf{R};\nu\mathbf{R}'}$ is provided by the Hückel method, in which the hopping integrals are proportional to the spatial overlap between the interacting orbitals:

$$H_{\mu\mathbf{R};\nu\mathbf{R}'} = \frac{\varepsilon_\mu + \varepsilon_\nu}{2} S_{\mu\mathbf{R};\nu\mathbf{R}'}. \tag{2.57}$$

Direct calculations show that the overlap between the p_z-orbitals on neighbouring atoms in graphene is equal roughly to 0.25. The energies of p_z-orbitals in isolated carbon atoms, estimated from the ionization experiments, are equal to -11.26 eV. Equation (2.57) then yields the nearest-neighbour hopping integral of $H_{\mu\mathbf{R};\nu\mathbf{R}'} = -2.82$ eV. This is a surprisingly good estimate of the actual nearest-neighbour hopping in graphene. For example, the fitting of the hopping integral directly to DFT calculations results in $H_{\mu\mathbf{R};\nu\mathbf{R}'} = -2.75$ eV.

Another approach was developed by Slater and Koster, who used symmetry rules to derive a series of analytical expressions, describing the interaction between various atomic orbitals as a function of the distance between the interacting atoms and the relative orientation of the orbitals [112]. In the case of p_z-orbitals in monolayer graphene, the Slater-Koster approximation gives the following interaction matrix elements: :

$$H_{\mu\mathbf{R};\nu\mathbf{R}'} = t \exp\left[-\gamma\left(\frac{|\mathbf{R}-\mathbf{R}'|}{a} - 1\right)\right], \tag{2.58}$$

where t is the hopping integral, corresponding to the interaction between nearest neighbours in graphene, γ is the rate of spatial decay, and a is the distance between nearest neighbours. This expression, in particular, can be used to model the effect of external strain on graphene, as it takes into account the variation of the hopping integrals with the interatomic separation.

It is relatively easy to include an external electric field in the tight-binding Hamiltonian. An external electric potential $V_{\text{ext}}(\mathbf{r})$ (which is not necessarily linear) modifies the onsite energies of atomic orbitals as:

$$H_{\mu\mathbf{R};\mu\mathbf{R}} = \varepsilon_\mu + V_{\text{ext}}(\mathbf{R}). \tag{2.59}$$

This expression assumes that the electric field does not polarise atoms themselves in a significant manner.

2.4.3 Solving the tight-binding Hamiltonian

A general tight-binding Hamiltonian, describing a system with multiple atomic orbitals per unit cell, can be conveniently written in the second quantization formalism as

$$\hat{H} = \sum_{\mu,\mathbf{R}} \varepsilon_\mu \hat{c}^\dagger_{\mu\mathbf{R}} \hat{c}_{\mu\mathbf{R}} + \sum_{\mu,\mathbf{R}} \sum_{\nu,\mathbf{R}'} t_{\mu\mathbf{R};\nu\mathbf{R}'} \hat{c}^\dagger_{\mu\mathbf{R}} \hat{c}_{\nu\mathbf{R}'}, \tag{2.60}$$

where μ and ν label atomic orbitals of the atoms in the unit cell of the system, $\mathbf{R}$ and $\mathbf{R}'$ label lattice sites, $c^\dagger_{\mu\mathbf{R}}$ and $\hat{c}_{\mu\mathbf{R}}$ are the creation and annihilation operators for the electron in atomic orbital of type μ at site $\mathbf{R}$, ε_μ is the onsite energy of atomic orbital μ, and $t_{\mu\mathbf{R};\nu\mathbf{R}'}$ is the hopping integral between atomic orbitals μ and ν at sites $\mathbf{R}$ and $\mathbf{R}'$. We take advantage of the periodicity and express the creation and annihilation operators for electrons on specific lattice sites as Fourier series,

$$\hat{c}^\dagger_{\mu\mathbf{R}} = \frac{1}{\sqrt{N}} \sum_{\mathbf{k}} e^{-i\mathbf{k}\cdot\mathbf{R}} \hat{c}^\dagger_{\mu\mathbf{k}}, \tag{2.61}$$

$$\hat{c}_{\mu\mathbf{R}} = \frac{1}{\sqrt{N}} \sum_{\mathbf{k}} e^{i\mathbf{k}\cdot\mathbf{R}} \hat{c}_{\mu\mathbf{k}}, \tag{2.62}$$

where N is the number of unit cells in the material and $\hat{c}^\dagger_{\mu\mathbf{k}}$ and $\hat{c}_{\mu\mathbf{k}}$ are the creation and annihilation operators for the Bloch waves propagating through the μth atomic orbitals. Substituting these expressions into the tight-binding Hamiltonian, we obtain

$$\hat{H} = \sum_{\mu,\mathbf{k}} \varepsilon_\mu \hat{c}^\dagger_{\mu\mathbf{k}} \hat{c}_{\mu\mathbf{k}} + \sum_{\mu,\nu,\mathbf{k}} \sum_{\mathbf{R}'-\mathbf{R}} t_{\mu\mathbf{R};\nu\mathbf{R}'} e^{i\mathbf{k}\cdot(\mathbf{R}'-\mathbf{R})} \hat{c}^\dagger_{\mu\mathbf{k}} \hat{c}_{\nu\mathbf{k}}. \tag{2.63}$$

In deriving the above equation, we have taken into account the well known identity

$$\frac{1}{N} \sum_{\mathbf{R}} e^{i(\mathbf{k}-\mathbf{k}')\cdot\mathbf{R}} = \delta_{\mathbf{k}\mathbf{k}'}. \tag{2.64}$$

It is seen that the Hamiltonian of the entire system is split into the sum of the contributions coming from individual $\mathbf{k}$-points:

$$\hat{H} = \sum_{\mathbf{k}} \hat{H}(\mathbf{k}). \tag{2.65}$$

The matrix elements of the Hamiltonian at individual $\mathbf{k}$-points, $H_{\mu\nu}(\mathbf{k}) = \langle\mu|\hat{H}(\mathbf{k})|\nu\rangle$, are given by

$$H_{\mu\nu}(\mathbf{k}) = \varepsilon_\mu \delta_{\mu\nu} + \sum_{\mathbf{R}'-\mathbf{R}} t_{\mu\mathbf{R};\nu\mathbf{R}'} e^{i\mathbf{k}\cdot(\mathbf{R}'-\mathbf{R})}. \tag{2.66}$$

This expression allows one to construct the tight-binding Hamiltonian for an arbitrary system, given that the hopping integrals between different atomic orbitals are known. The number of terms in the sum is finite (and often small) if only the interaction between certain neighbours is considered.

At each **k**-point, the Hamiltonian (2.66) is a matrix of size $M \times M$ where M is the number of unique orbitals per unit cell. Matrix $H(\mathbf{k})$ has to be diagonalised at each **k**-point, producing a set of M energy bands $\varepsilon_i(\mathbf{k})$ and M corresponding eigenvectors $c_{i\mu}(\mathbf{k})$, where i is the index of the energy band. The tight-binding method often provides very good predictions for the energy bands $\varepsilon_i(\mathbf{k})$ if these bands originate predominantly from the orbitals included in the tight-binding model and can also be used to model total energies of materials as functions of the atomic positions. Various other physical quantities can be calculated from the tight-binding energy bands, such as the density of states:

$$f(E) = \sum_{i,\mathbf{k}} \delta(\varepsilon_i(\mathbf{k}) - E), \tag{2.67}$$

where the Dirac delta functions $\delta(x)$ can be replaced with finite-width peaks for the purposes of numerical calculations. The Fermi energy of the system with N electrons is computed by solving an implicit equation

$$N = 2 \int_{-\infty}^{E_\mathrm{F}} f(E)\,\mathrm{d}E, \tag{2.68}$$

where the factor of 2 appears because each quantum state is doubly degenerate with respect to the electron spin for spin-unpolarised systems. The eigenvectors $c_{i\mu}(\mathbf{k})$ of the tight-binding Hamiltonian also hold important physical meaning. The number of electrons occupying orbital ϕ_μ is given by the sum of the form

$$\langle \hat{\rho}_\mu \rangle = \sum_{i,\mathbf{k}} |c_{i\mu}(\mathbf{k})|^2\, \Theta[E_\mathrm{F} - \varepsilon_i(\mathbf{k})], \tag{2.69}$$

where $\Theta(x)$ is the Heaviside step function that is equal to one if $x > 0$ and to zero otherwise, ensuring that the sum runs only over the occupied states. Note, however, that $\langle \hat{\rho}_\mu \rangle$ describes only the electron density coming from the atomic orbitals included in the tight-binding model.

2.4.4 Mean-field Hubbard model

As was discussed before, some graphene nanoribbons feature magnetism that arises from the spin-polarised electron densities. It is possible to capture this effect by introducing spin-

polarisation in the tight-binding Hamiltonian. The basis set of the tight-binding model is then doubled, as each atomic orbital can host two electrons with opposite spins. The hopping between atomic orbitals with different spins can be assumed to be zero, as the probabilities of spin-flip interactions are relatively small. Energy bands and eigenvectors are now labeled $\varepsilon_{\sigma i}(\mathbf{k})$ and $c_{\sigma i\mu}(\mathbf{k})$ to differentiate eigenstates arising from the sets of atomic orbitals with opposite spin orientations σ.

It is also necessary to introduce some form of electron-electron interaction to ensure that the electron densities of opposite spin can interact. The simplest approach was suggested by Hubbard, who introduced a term corresponding to repulsion of two electrons localised at the same lattice site. The tight-binding Hamiltonian then acquires an additional term of the form

$$\hat{H}' = U \sum_{\mu} \hat{\rho}_{\mu\uparrow} \hat{\rho}_{\mu\downarrow}, \tag{2.70}$$

where U is the energy of repulsion between two electrons occupying the same atomic orbital and

$$\hat{\rho}_{\mu\sigma} = \hat{c}^{\dagger}_{\mu\sigma} \hat{c}_{\mu\sigma} \tag{2.71}$$

is the electron density of spin σ occupying atomic orbital μ. The numerical treatment of this Hamiltonian is complicated due the fact that it depends on the densities of both spin-up and spin-down electrons. This is circumvented in the mean field approximations, which simplifies the Hubbard Hamiltonian to

$$\hat{H}' \approx U \sum_{\mu} [\hat{\rho}_{\mu\uparrow} \langle \rho_{\mu\downarrow} \rangle + \langle \rho_{\mu\uparrow} \rangle \hat{\rho}_{\mu\downarrow}], \tag{2.72}$$

where $\langle \rho_{\mu\sigma} \rangle$ is the average density of spin-σ electrons occupying atomic orgital μ.

It is seen that the mean-field Hubbard Hamiltonian simply modifies the onsite energy of spin-up (spin-down) electrons in atomic orbital μ by $U\langle \rho_{\mu\downarrow} \rangle$ ($U\langle \rho_{\mu\uparrow} \rangle$). The two sets of atomic orbitals corresponding to opposite spin orientations remain uncoupled, so that the tight-binding Hamiltonian can be diagonalised separately for spin-up and spin-down states. After the diagonalisation, the density of states of the system is given by

$$f(E) = \sum_{\sigma, i, \mathbf{k}} \delta(\varepsilon_{\sigma i}(\mathbf{k}) - E), \tag{2.73}$$

and the Fermi energy is determined as

$$N = \int_{-\infty}^{E_{\mathrm{F}}} f(E)\, \mathrm{d}E, \tag{2.74}$$

where the factor of 2 is no longer needed, as the spin is included explicitly. The number of spin-σ electrons occupying orbital μ is given by

$$\langle \hat{\rho}_{\sigma\mu} \rangle = \sum_{i,\mathbf{k}} |c_{\sigma i\mu}(\mathbf{k})|^2 \, \Theta[E_{\mathrm{F}} - \varepsilon_{\sigma i}(\mathbf{k})], \tag{2.75}$$

Similar to the Kohn-Sham equations, the mean-field Hubbard Hamiltonian has to be diagonalised self-consistently. The electron densities of spin-up and spin-down electrons are calculated knowing the eigenstates of the Hamiltonian. At the same time, these electron densities are needed to calculate the diagonal elements of the Hamiltonian, whose diagonalisation produces the eigenstates. The mean-field Hubbard Hamiltonian is thus solved iteratively. An initial electron density is specified, the matrix elements of the Hamiltonian are calculated, and the eigenstates are obtained. The electron density is then recalculated and compared to the initial guess. This process continues until the difference between the electron densities at two consecutive steps becomes smaller than the specified tolerance threshold.

The magnetization on each atomic orbital in the unit cell is conveniently characterised by the difference between the spin-up and spin-down electron densities:

$$M_\mu = \frac{\langle \hat{\rho}_{\uparrow\mu} \rangle - \langle \hat{\rho}_{\downarrow\mu} \rangle}{2}, \tag{2.76}$$

where the factor of $1/2$ stands for electron spin. The total spin of the unit cell is given by

$$S = \sum_\mu M_\mu. \tag{2.77}$$

In order to ensure that the self-consistent solution is able to converge at the correct distribution of spin-polarised electron densities, it is important to break the initial symmetry of the electronic structure with respect to spin. For example, if it is known that the material is ferromagnetic ($S \neq 0$), it is necessary to make the initial spin-up and spin-down densities different. Alternatively, if the material is antiferromagnetic, meaning that the total magnetization is zero, $S = 0$, but separate regions of the material are magnetized, it is crucial to ensure that the initial electron densities vary within the unit cell. Equipped with the most relevant *ab initio* and semi-empirical methods, we now proceed to unravel electronic properties of graphene nanoribbons.

Chapter 3

Hidden symmetries in graphene nanoribbons

Armchair graphene nanoribbons are a highly promising class of semiconductors for all-carbon nanocircuitry. In this Chapter, I present a new perspective on their electronic structure from simple model Hamiltonians and *ab initio* calculations. I focus on a specific set of nanoribbons of width $n = 3p + 2$, where n is the number of carbon atoms across the nanoribbon axis and p is a positive integer. I demonstrate that the energy-gap opening in these nanoribbons originates from the breaking of a previously unidentified hidden symmetry by long-ranged hopping of π-electrons and structural distortions occurring at the edges. This hidden symmetry can be restored or manipulated through the application of in-plane lattice strain, which enables continuous energy-gap tuning, the emergence of Dirac points at the Fermi level, and topological quantum phase transitions. In this way, I establish an original interpretation of the semiconducting character of armchair graphene nanoribbons and offer guidelines for rationally designing their electronic structure.

This Chapter draws heavily upon a research paper co-authored by me and published in *Physical Review Letters*:

> **N. V. Tepliakov**, J. Lischner, E. Kaxiras, A. A. Mostofi, M. Pizzochero. Unveiling and Manipulating Hidden Symmetries in Graphene Nanoribbons. *Phys. Rev. Lett.* **130**, 026401 (2023). [Online]

Substantial portions of text included in this chapter were written collaboratively by all contributing authors. I contributed to the work by conceiving the original idea, conducting calculations, preparing figures, and leading the writing process.

3.1 Graphene nanoribbons with armchair edges

3.1.1 *Ab initio* parametrized tight binding model

Armchair graphene nanoribbons (AGNRs) are a class of one-dimensional graphene nanostructures whose crystal structure is shown in Fig. 3.1. It is commonly known that graphene nanoribbons with armchair-type edges are semiconducting and non-magnetic, greatly simplifying the description of their electronic properties with semi-analytical models. The low-energy band structure of AGNRs is typically described using the tight-binding Hamiltonian for the p_z-electrons [113], which has the form

$$\hat{\mathcal{H}} = \left(\sum_{\langle i,j \rangle} t_1 + \sum_{\langle\langle i,j \rangle\rangle} t_2 + \sum_{\langle\langle\langle i,j \rangle\rangle\rangle} t_3 \right) (\hat{c}_i^\dagger \hat{c}_j + \text{h.c.}), \tag{3.1}$$

where t_1, t_2, and t_3 are the first, second, and third nearest-neighbor hopping interactions, respectively, $c_i^\dagger$ and $\hat{c}_i$ are the creation and annihilation operators for a p_z-electron at site i, and indices $\langle i,j \rangle$, $\langle\langle i,j \rangle\rangle$, and $\langle\langle\langle i,j \rangle\rangle\rangle$ indicate the summation over those atomic sites which are the first, second, and third nearest neighbours.

To accurately quantify the hopping interactions between p_z-orbitals in armchair graphene nanoribbons, we perform first-principles calculations in the density-functional theory (DFT) formalism, as implemented in the Quantum ESPRESSO package [109, 110]. We rely on the generalized-gradient approximation of Perdew, Burke, and Ernzerhof [115]. We set the wavefunction (charge density) cutoff to 80 Ry (360 Ry), and sample the Brillouin zone with 12 and 24 k-points in the geometry optimization and band structure calculations, respectively. We introduce a vacuum region 15 Å thick in the non-periodic directions to avoid artificial interactions between periodic replicas.

The resulting first-principles calculations are subsequently used to construct Wannier functions by projecting the Bloch states onto the p_z-orbitals of carbon atoms, taking advantage of the Wannier90 package [116]. In order to disentangle the energy bands arising from the p_z-

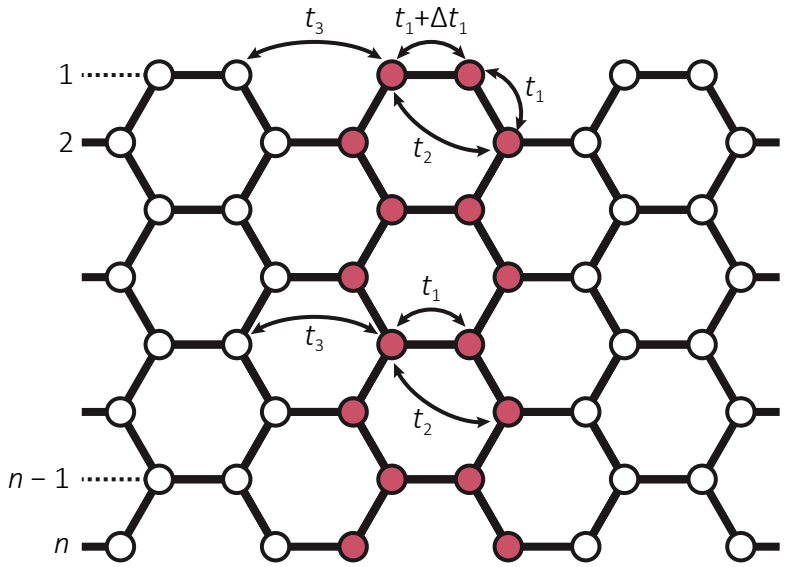


Figure 3.1: Crystal structure of armchair graphene nanoribbons (AGNRs) with n carbon atoms in the lateral direction. Also illustrated are the first, second, and third nearest-neighbor hopping parameters t_1, t_2, and t_3, respectively, as well as the change of the first-nearest neighbor hopping parameter at the edges of the nanoribbon, Δt_1 due to a structural distortion. Reprinted with permission from *Phys. Rev. Lett.* 2023, 130, 026401 [114]. Copyright 2023 American Physical Society.

orbitals, we consider an outer energy window, which contains *all* the bands originating from the p_z-orbitals, and an inner frozen window, in which the energy bands are contributed *only* by the p_z-orbitals. In Fig. 3.2(a), we compare the band structure of a representative armchair graphene nanoribbon obtained from first-principles and Wannier calculations. It is seen that the DFT and Wannierized band structures show a perfect agreement in the considered energy range.

From the real-space Wannier representation, we find that the bulk values of hopping parameters in armchair graphene nanoribbons are $t_1 = -2.88$ eV, $t_2 = 0.22$ eV, and $t_3 = -0.25$ eV. Importantly, t_1 changes by $\Delta t_1 = -0.20$ eV at the edges of the nanoribbon because of the shortening of the interatomic distance between carbon atoms at the edges by $\sim$4% as a result of a lattice relaxation [14]. This is a well-known phenomenon arising from the finite width of graphene nanoribbons compared to infinite sheets of graphene. Fig. 3.2(b) shows the band structure of a representative armchair graphene nanoribbon obtained using the tight-binding Hamiltonian with these values of the hopping parameters. It is found that the tight-binding model with three hopping interactions and modification of the first nearest-neighbour hopping at the edges is in excellent agreement with the first-principles result at

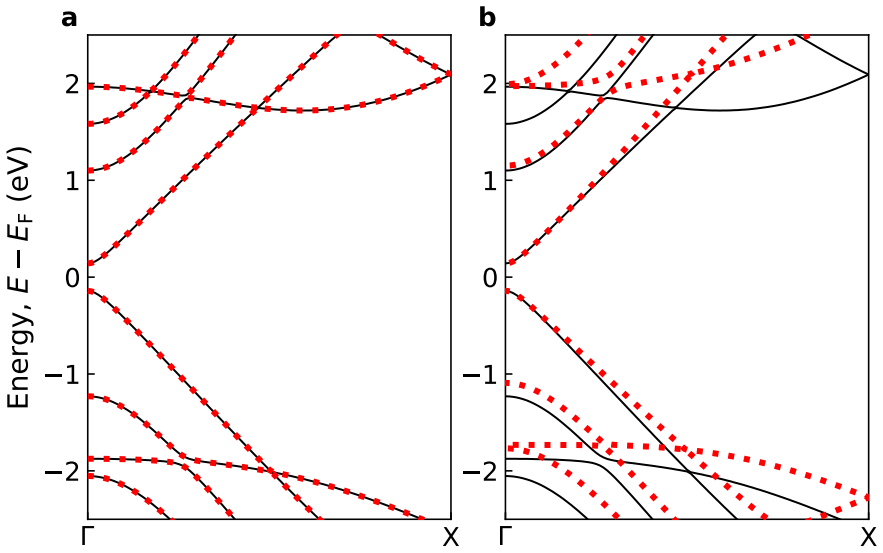


Figure 3.2: Band structure of an armchair graphene nanoribbon of width $n = 8$. Black solid lines correspond to the first-principles calculations whereas the red dots are the energy bands originating from the p_z-orbitals, as obtained (a) through Wannierization of first-principles calculations and (b) tight-binding Hamiltonian with parameters $t_1 = -2.88$ eV, $t_2 = 0.22$ eV, $t_3 = -0.25$ eV, and $\Delta t_1 = -0.20$ eV. Reprinted with permission from *Phys. Rev. Lett.* 2023, 130, 026401 [114]. Copyright 2023 American Physical Society.

low energies. This *ab initio*-parameterized tight-binding Hamiltonian allows us to effectively disentangle the contribution of each hopping interaction to the resulting electronic structure.

3.1.2 Energy gaps of $n=3p+2$ graphene nanoribbons

For completeness, in Fig. 3.3 we start by recalling the dependence of the energy gaps of AGNRs, E_g, on their width, which was previously assessed in numerous theoretical and experimental studies. The width of AGNRs is conveniently quantified by the number of carbon atoms across the nanoribbon axis, n. Nanoribbons can be grouped according to their width, depending on whether $n = 3p$, $3p + 1$, or $3p + 2$, where p is a positive integer [14]. First, we consider only nearest-neighbor hopping interactions t_1 and ignore the shortening of the bond lengths at the edges of the nanoribbon. The energy gaps predicted by this simplistic first nearest-neighbour tight-binding model are plotted in Fig. 3.3(a). For $n = 3p + 2$, AGNRs are gapless and possess a zero-energy Dirac point, while for $n = 3p$ or $n = 3p + 1$ they exhibit a direct energy gap located at the center of the Brillouin zone, the magnitude of which scales

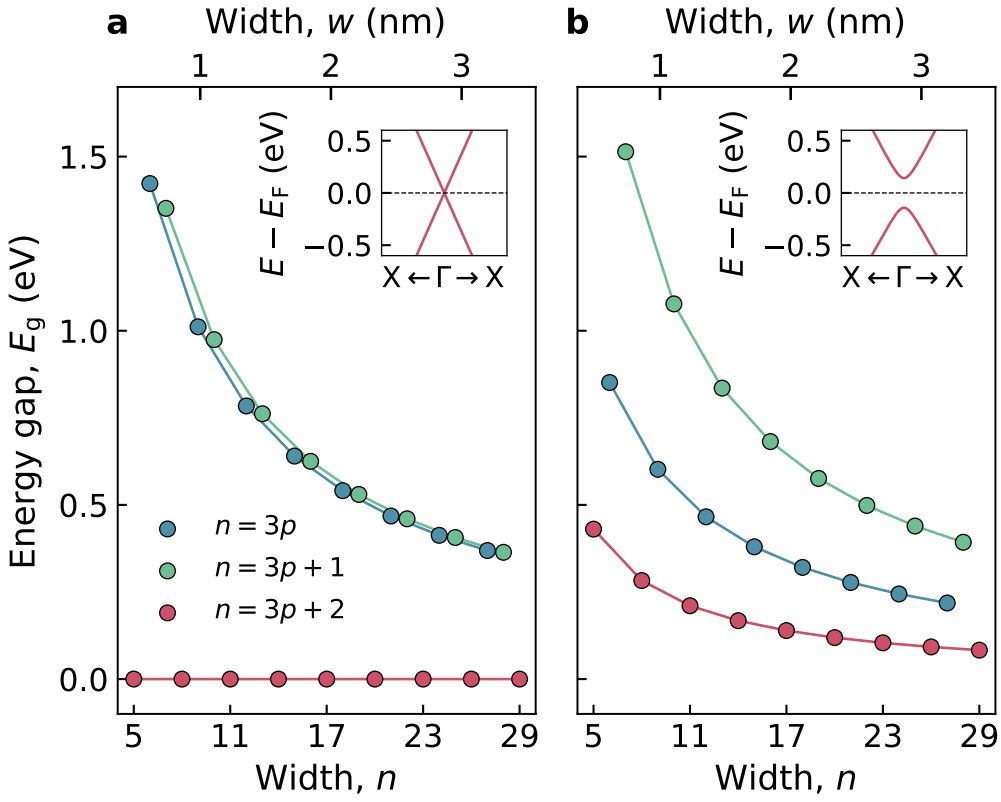


Figure 3.3: Evolution of the energy gap, E_g, of nanoribbons of increasing width n obtained using the tight-binding Hamiltonian in Eq. (3.1) when (a) t_2, t_3, and Δt_1 are ignored, and (b) t_2, t_3, and Δt_1 are included. The insets show the band structures in the vicinity of the Γ point for the representative width $n = 8$. Reprinted with permission from *Phys. Rev. Lett.* 2023, 130, 026401 [114]. Copyright 2023 American Physical Society.

inversely with the width. Next, we account for both the farther nearest-neighbor hopping interactions, t_2 and t_3, and the shortening of the bond lengths at the edges, which results in a local increase in magnitude of the first nearest-neighbor hopping interaction by Δt_1. The resulting width-dependence of the energy gaps is shown in Fig. 3.3(b). It is found that the more complete tight-binding approximation predicts non-zero width-dependent energy gaps for AGNRs with $n = 3p + 2$ too, unlike the simple tight-binding model containing only the nearest-neighbour hoppings. These results are in agreement with earlier theoretical works that used first-principles calculations [14, 117].

It is thus seen that the second and third nearest-neighbor hopping interactions t_2 and t_3, as well as the structural distortions at the edges of the nanoribbon, are key to open the energy gap in armchair graphene nanoribbons of width $n = 3p + 2$. In order to quantify the relative importance of these two mechanisms in the energy-gap opening, we perform two distinct

calculations:

1. We ignore the structural distortion at the edges, but account for hopping interactions up to t_3;

2. We ignore the third nearest-neighbor hopping interactions t_3, but account for the structural distortion at the edges through the corresponding local change in the hopping interaction Δt_1.

The result of these calculations are shown in Fig. 3.4. Our analysis reveals that the effect of long-range hopping interactions and structural distortions at the edges are comparable in determining the magnitude of the energy gap, with the contribution from including t_3 exceeding that from accounting for Δt_1 by ∼20%. Overall, this observation points to a distinct nature of the semiconducting state in AGNRs of width $n = 3p + 2$ compared to $n = 3p$ or $n = 3p + 1$.

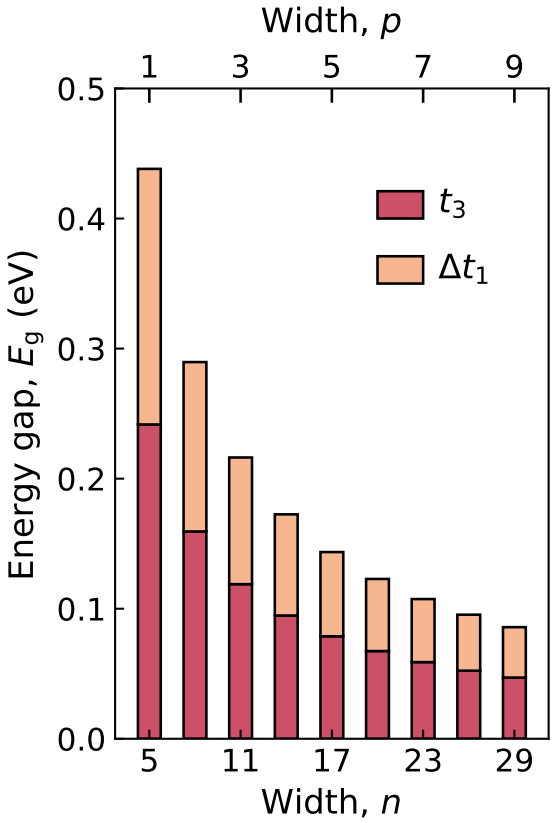


Figure 3.4: Contribution of the third-nearest neighbour hopping t_3 and the edge-distortion term Δt_1 to the energy gaps E_g of AGNRs of width $n = 3p + 2$. Reprinted with permission from *Phys. Rev. Lett.* 2023, 130, 026401 [114]. Copyright 2023 American Physical Society.

3.1.3 Robustness of semimetallic phase in graphene

It is important to stress that contrary to armchair graphene nanoribbons, graphene remains semimetallic irrespective of the strength of long-range next-neighbor hopping interactions between the p_z-orbitals. The tight-binding Hamiltonian of graphene, written in the basis of two sublattices A and B, reads [118]

$$\hat{\mathcal{H}}_{\mathbf{k}} = \begin{pmatrix} h_2(\mathbf{k}) & h_1(\mathbf{k}) + h_3(\mathbf{k}) \\ h_1^\dagger(\mathbf{k}) + h_3^\dagger(\mathbf{k}) & h_2(\mathbf{k}) \end{pmatrix}, \tag{3.2}$$

where

$$h_1(\mathbf{k}) = t_1 \left[e^{ik_y a} + 2\cos\frac{\sqrt{3}k_x a}{2} e^{-ik_y a/2} \right], \tag{3.3}$$

$$h_2(\mathbf{k}) = 2t_2 \left[\cos\left(\sqrt{3}k_x a\right) + 2\cos\frac{\sqrt{3}k_x a}{2} \cos\frac{3k_y a}{2} \right], \tag{3.4}$$

$$h_3(\mathbf{k}) = t_3 \left[e^{-2ik_y a} + 2\cos\left(\sqrt{3}k_x a\right) e^{ik_y a} \right], \tag{3.5}$$

and a is the C-C bond length. Around the K point of the Brillouin zone, this Hamiltonian can be simplified as

$$\hat{\mathcal{H}}_{\mathbf{k}} = \begin{pmatrix} -3t_2 & (1 - 2t_3/t_1) v_{\mathrm{F}} q_+ \\ (1 - 2t_3/t_1) v_{\mathrm{F}} q_- & -3t_2 \end{pmatrix}, \tag{3.6}$$

where $q_\pm = q_x \pm i q_y$, $\mathbf{q} = \mathbf{k} - \mathrm{K}$ is the electron momentum relative to the K point and $v_{\mathrm{F}} = 3t_1 a/2$ is the Fermi velocity when t_2 and t_3 are set to zero. The diagonalization of this Hamiltonian yields

$$E_\pm(\mathbf{k}) = -3t_2 \pm \left(1 - \frac{2t_3}{t_1}\right) v_{\mathrm{F}} |\mathbf{q}|. \tag{3.7}$$

Hence, the addition of second and third nearest-neighbor hopping interactions, t_2 and t_3, is ineffective in opening the energy gap in graphene, which remains semimetallic at $\mathbf{q} = 0$. Unlike armchair graphene nanoribbons, in graphene t_3 merely renormalises the Fermi velocity as

$$\tilde{v}_{\mathrm{F}} = \left(1 - \frac{2t_3}{t_1}\right) v_{\mathrm{F}}. \tag{3.8}$$

3.2 Origin of energy gaps in graphene nanoribbons

3.2.1 Isomorphic transformation of graphene nanoribbons

To explain the origin of the energy-gap opening in nanoribbons with $n = 3p + 2$, we initially consider the nearest-neighbor tight-binding Hamiltonian with $\Delta t_1 = t_2 = t_3 = 0$. Instead of treating a graphene nanoribbon as an infinitely extended one-dimensional crystal, we perform an isomorphic transformation and replace it with the auxiliary, finite-size model shown in Fig. 3.5. It is important that this model features the same energy spectrum as the corresponding AGNR at the center of the Brillouin zone [14]. Since the valence band maximum and conduction band minimum of AGNRs are both at the Γ point, the energy gap of the auxiliary model is the same as the energy gap of the corresponding AGNR. For the illustrative case of $n = 8$ ($p = 2$), the energy spectrum of the auxiliary model is shown in Fig. 3.6(a). We observe a pair of zero-energy degenerate levels $|\psi\rangle$ and $|\phi\rangle$, which correspond to the Dirac point in the band structure of the equivalent AGNR from the $n = 3p + 2$ group.

The main reason why we introduce this auxiliary model is because it provides important insights into the underlying symmetry of AGNRs. The presence of the double degeneracy

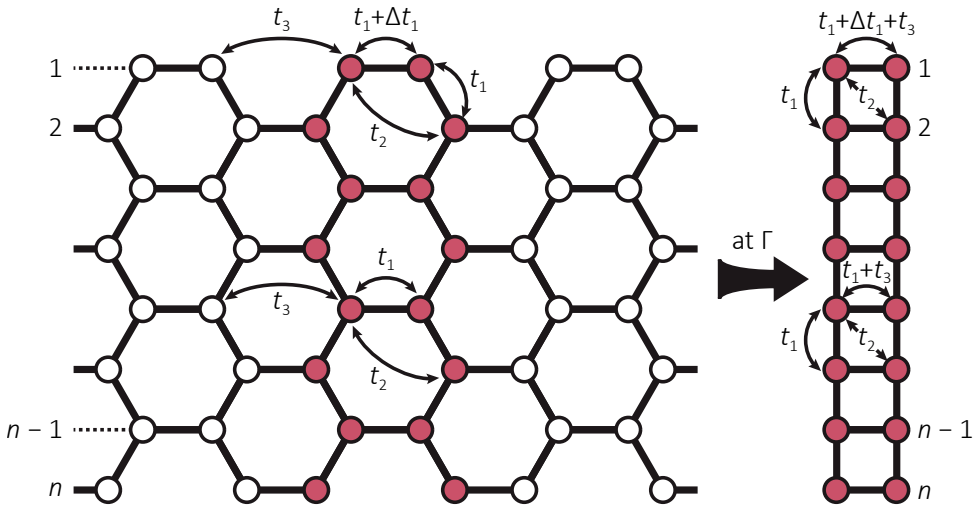


Figure 3.5: Isomorphic transformation of an extended AGNR with n carbon atoms in the lateral direction into a finite-size auxiliary model, represented by a $2 \times n$ two-leg ladder lattice. The auxiliary model has the same energy spectrum as the nanoribbon at the Γ point of the Brillouin zone. Reprinted with permission from *Phys. Rev. Lett.* 2023, 130, 026401 [114]. Copyright 2023 American Physical Society.

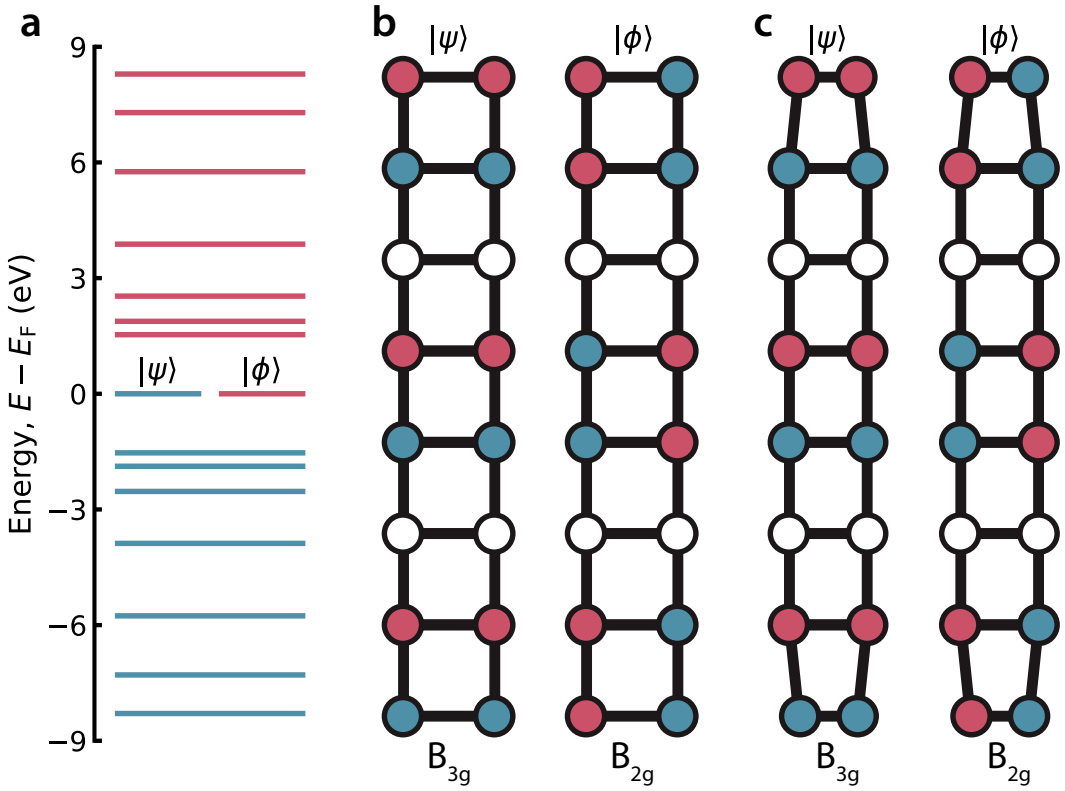


Figure 3.6: (a) Energy spectrum at the Γ point of an AGNR with $n = 8$, as obtained from the tight-binding Hamiltonian ignoring long-range hopping interactions and the structural distortion at the edges of the nanoribbon ($t_2 = t_3 = \Delta t_1 = 0$). (b) Wavefunctions corresponding to the pair of zero-energy degenerate levels $|\psi\rangle$ and $|\phi\rangle$ of the auxiliary model with $n = 8$, as obtained through the tight-binding Hamiltonian with $t_2 = t_3 = \Delta t_1 = 0$; red and blue colours indicate opposite signs of the wavefunction, whereas white colour corresponds to its zero values. (c) Same as panel (b), but including long-range hopping interactions, t_2 and t_3, and the structural distortion occurring at the edges of the nanoribbon, Δt_1, in the tight-binding Hamiltonian. Reprinted with permission from *Phys. Rev. Lett.* 2023, 130, 026401 [114]. Copyright 2023 American Physical Society.

at the Fermi level in AGNRs with $n = 3p + 2$ is surprising because it is not enforced by the rectangular point symmetry group D_{2h} of the auxiliary model, which has only non-degenerate irreducible representations. These degenerate zero-energy modes $|\psi\rangle$ and $|\phi\rangle$, therefore, must arise from an additional, *hidden* symmetry, not evident from the geometry of AGNRs. The most famous example of such a hidden symmetry is the degeneracy of the energy levels of the hydrogen atom with respect to the orbital angular momentum, which is not enforced by the spherical symmetry of the atoms, but is rather associated with the Laplace-Runge-Lenz vector [119].

We now need to reveal the hidden symmetry associated with the auxiliary model corresponding to $n = 3p + 2$ AGNRs. At the nearest-neighbor tight-binding level, the Hamiltonian of the auxiliary model can be solved analytically. First, we note that the solution for a square lattice is separable in Cartesian coordinates x and y, i.e., it can be decoupled in two perpendicular sets of one-dimensional chains. A one-dimensional chain of infinite length has a straightforward solution of the form

$$\psi_k(\xi_i) = Ae^{ik\xi_i} + Be^{-ik\xi_i}, \tag{3.9a}$$

$$E_k = 2t_1 \cos k, \tag{3.9b}$$

where we set the lattice constant to unity, t_1 is the nearest-neighbor hopping amplitude, and ξ_i is the coordinate of the i-th lattice site. In a finite chain comprising n sites located at $\xi_i = 1, 2, \ldots, n$, the wavefunction must vanish outside the chain region. This is described by the boundary condition

$$\psi_k(0) = \psi_k(n + 1) = 0, \tag{3.10}$$

which enforces the quantization of the electron momentum as

$$k = \frac{\pi m}{n + 1}, \tag{3.11}$$

where $m = 1, 2, \ldots, n$ labels the energy states of the chain. The normalized wavefunctions and the energies are then given by

$$\psi_m(\xi_i) = \sqrt{\frac{2}{n + 1}} \sin\left(\frac{\pi m \xi_i}{n + 1}\right), \tag{3.12a}$$

$$E_m = 2t_1 \cos\left(\frac{\pi m}{n + 1}\right). \tag{3.12b}$$

Notably, the wavefunctions of the chain of n sites are identical to continuum wavefunctions of an infinite quantum well of width $(n + 1)$, albeit with different energies.

This analytical result is easily generalized to the case of the auxiliary model shown in Figure 3.5, which is a lattice of $2 \times n$ sites (i.e., the two-leg ladder lattice), yielding

$$E_{m_x m_y} = 2t_1 \left[\cos\left(\frac{\pi m_x}{3}\right) + \cos\left(\frac{\pi m_y}{n + 1}\right)\right], \tag{3.13a}$$

$$\psi_{m_x m_y}(x_i, y_i) = \frac{2}{\sqrt{3(n + 1)}} \sin\left(\frac{\pi m_x x_i}{3}\right) \sin\left(\frac{\pi m_y y_i}{n + 1}\right), \tag{3.13b}$$

where x_i and y_i are the Cartesian coordinates of the i-th site of the auxiliary model. Since the n-site chain is equivalent to an infinite well of size $(n + 1)$, then the auxiliary model of size

$2 \times n$ is equivalent by analogy to a two-dimensional quantum box of dimensions $3 \times (n+1)$, where the quantum numbers labeling the states take values $m_x = 1, 2$ and $m_y = 1, 2, \ldots, n$, so that in total there are $2n$ states. The wavefunctions $\psi_{m_x m_y}(x_i, y_i)$ are discrete and provide the coefficients of the eigenvectors on the i-th site with Cartesian coordinates x_i and y_i. This wavefunction can be viewed as the mapping of the continuous wavefunction $\psi_{m_x m_y}(x, y)$, which spans over the entire two-dimensional space, onto the lattice sites of the auxiliary model.

3.2.2 Hidden symmetry of rectangular quantum box

We have thus shown that the auxiliary model corresponding to AGNRs is somewhat equivalent to the rectangular quantum box. Notably, it is known that the rectangular quantum box possesses a hidden symmetry associated with the four-fold rotation around one of the corners of the box [120], described by the operator

$$\hat{C}_4 \psi(x, y) = \psi(y, -x). \tag{3.14}$$

This symmetry enforces the seemingly accidental degeneracy of pairs of states (m_x, m_y) and (m'_x, m'_y) that transform into each other as $\psi_{m_x m_y} = -\hat{C}_4 \psi_{m'_x m'_y}$. In order to determine such pairs, we solve $\psi_{m_x m_y}(x, y) = -\psi_{m'_x m'_y}(y, -x)$ or

$$\sin\left(\frac{\pi m_x x}{3}\right) \sin\left(\frac{\pi m_y y}{n+1}\right) = \sin\left(\frac{\pi m'_x y}{3}\right) \sin\left(\frac{\pi m'_y x}{n+1}\right). \tag{3.15}$$

This equation must hold for all values of x and y. Hence we obtain that pairs of degenerate levels are determined by the conditions

$$m'_x = \frac{3}{n+1} m_y, \quad m'_y = \frac{n+1}{3} m_x. \tag{3.16}$$

Since m_x only assumes values 1 and 2, the ratio $(n+1)/3$ must be an integer and we naturally obtain the condition $n = 3p + 2$, yielding

$$m'_x = \frac{m_y}{p+1}, \quad m'_y = (p+1) m_x. \tag{3.17}$$

For any n, there is only one pair of states that satisfies these conditions: $(m_x, m_y) = (1, 2p+2)$ and $(m'_x, m'_y) = (2, p+1)$. Importantly, the electron-hole symmetry following from the nearest-neighbor tight-binding Hamiltonian requires that this double degeneracy occurs at

the Fermi level. We have thus obtained that the two-leg ladder lattice corresponding to the $n = 3p + 2$ AGNRs does not have an energy gap at this level of theory. This lack of energy gap originates from the hidden four-fold rotational symmetry of the rectangular quantum box. Note, however, that the hidden symmetry is only relevant at the Γ point of the extended nanoribbons, and that the AGNRs are gapped throughout the rest of the Brillouin zone.

3.2.3 Wave functions of degenerate states

To further understand the effect of the hidden symmetry $\hat{C}_4$ on the electronic structure, we examine the wavefunctions of the two degenerate states, $|\psi\rangle$ and $|\phi\rangle$, illustrated in Fig. 3.6(b). As can be seen in the figure, these wavefunctions are strictly localized in regions of square symmetry that are separated by nodal lines (sites denoted by empty circles). Even though $|\psi\rangle$ and $|\phi\rangle$ belong to the irreducible representations B_{3g} and B_{2g} of the D_{2h} group, the wavefunction in each square region is reminiscent of a doubly degenerate irreducible representation E_{2g} of D_{4h}, which is the point symmetry group of the square molecule cyclobutadiene (C_4H_4), arguably the simplest π-electron model system hosting zero-energy degenerate levels. And it is indeed the case that the wavefunctions of these degenerate states $|\psi\rangle$ and $|\phi\rangle$ transform into each other through a hidden four-fold rotational symmetry, as demonstrated in Fig. 3.7. The degenerate states $|\psi\rangle$ and $|\phi\rangle$ correspond to the states $(1,2p+2)$ and $(2,p+1)$ in the quantum box, which, as we have shown previously, are connected through the hidden symmetry as $|\psi\rangle = -\hat{C}_4|\phi\rangle$.

In Figure 3.8, we expand our investigation by inspecting the wavefunctions of all the sixteen energy levels of the auxiliary model for the representative case $n = 8$, and of cyclobutadiene (C_4H_4) for comparison. Remarkably, we note that, in addition to the pair of zero-energy states denoted $|\psi\rangle = |8\rangle$ and $|\phi\rangle = |9\rangle$, there are two additional states $|3\rangle$ and $|14\rangle$ which are localized in a similar square-shaped pattern separated by unoccupied nodes of the square lattice. Within each square region, these states are reminiscent of the non-degenerate ground and second excited states of cyclobutadiene, in the same way that $|8\rangle$ and $|9\rangle$ resemble its zero-energy modes. The eigenstate coefficients of the additional states $|3\rangle$ and $|14\rangle$ are obtained by mapping the wave functions of states $(1,p+1)$ and $(2,2p+2)$ in the rectangular quantum box. Combined, these four states with the square-shaped localization pattern are observed in all armchair graphene nanoribbons of the $n = 3p + 2$ family.

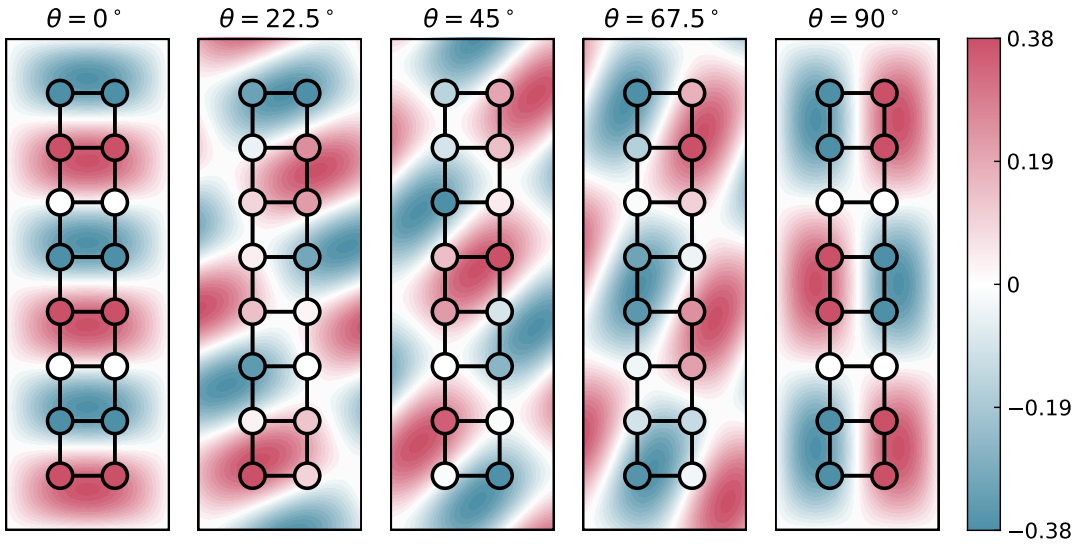


Figure 3.7: Rotation of the degenerate state with indices $(1, 2p + 2) = (1, 6)$ in the quantum box corresponding to the auxiliary model with $n = 8$ by an angle θ. Upon four-fold rotation ($\theta = 90°$), this state transforms into the other degenerate state $(2, p + 1) = (2, 3)$, up to a minus sign. Reprinted with permission from *Phys. Rev. Lett.* 2023, 130, 026401 [114]. Copyright 2023 American Physical Society.

We have thus established that the origin of the degeneracy in the energy spectrum of the ANGRs with $n = 3p + 2$ traces back to the presence of a hidden four-fold rotational symmetry $\hat{C}_4$, that is, a symmetry operation of the electronic states that is not inherent to the symmetry of the crystal structure. This hidden symmetry enforces the peculiar square-shaped localization pattern of electrons, which only AGNRs of the $n = 3p+2$ class can accommodate according to our analysis.

We are now ready to answer the key question of this chapter as to why $n = 3p + 2$ AGNRs have an energy gap at the center of the Brillouin zone that originates from the third nearest-neighbour hopping, t_3, and from the structural distortions at the edges of the nanoribbon, Δt_1. Both mechanisms lift the local $\hat{C}_4$ symmetry of the square-shaped regions of the two-leg ladder model. As evidenced by Figure 3.5, longer-range π-electron hopping t_3 effectively shortens the bonds in the periodic direction of the nanoribbon, but does not affect the bonding in the transverse direction. This deforms the square-shaped localization pattern of the zero-energy states, as illustrated in Fig. 3.6(c), and breaks the hidden symmetry. The edge reconstruction mechanism further contributes to the symmetry breaking, strengthening the bonding at the edges of the nanoribbon by Δt_1. Figure 3.5 also makes it clear why the second

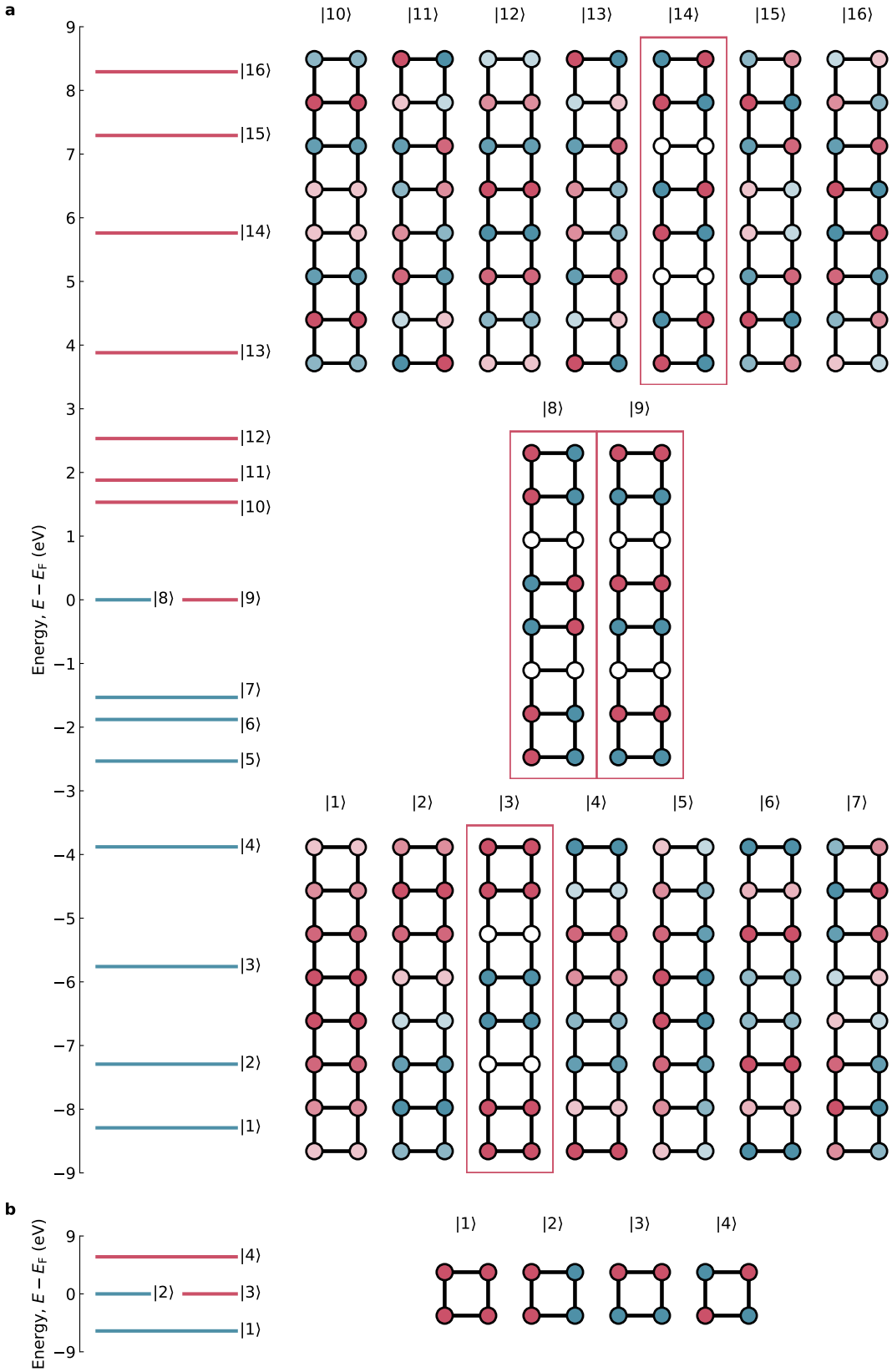


Figure 3.8: Energy spectrum and corresponding wavefunctions of (a) the auxiliary model for the representative case $n = 8$ and (b) cyclobutadiene, as obtained at the nearest-neighbor tight-binding level. Reprinted with permission from *Phys. Rev. Lett.* 2023, 130, 026401 [114]. Copyright 2023 American Physical Society.

nearest-neighbor hopping t_2 is ineffective in opening an energy gap in the nanoribbon. By acting along the diagonal of each square fragment of the two-leg ladder model, t_2 preserves the hidden four-fold rotational symmetry and thus does not lift the degeneracy of the energy bands at the Fermi level. Nevertheless, the second nearest-neighbor hopping t_2 still has an important effect on the energy gaps of $n = 3p + 2$ AGNRs. If each square-shaped fragment of the auxiliary model was isolated from the others, the energy gap of the nanoribbon would be determined only by t_3 and Δt_1. However, since the square fragments are coupled through t_2, the overall energy gap of the AGNR decreases with the width of the nanoribbon, as shown in Fig. 3.3(b).

3.3 Strain engineering of armchair graphene nanoribbons

3.3.1 Energy gap tuning and Dirac semimetallicity

Having established the origin of the semiconducting state in AGNRs of width $n = 3p + 2$, we next devise strategies to engineer their electronic structure. This is accomplished by exploiting the interplay between the spatial and hidden symmetries through lattice deformations. As illustrated in Fig. 3.9, tensile strain exerted along the nanoribbon axis decreases the longitudinal hopping interactions in the auxiliary model from $t_1 + t_3$ to $t_{\parallel} \approx (t_1 + t_3)(1 - \gamma\varepsilon)$, where γ is the spatial decay constant of the hopping integrals and ε is the relative elongation. Due to the Poisson effect, such an elongation induces a concurrent compression of $-\nu\varepsilon$ in the perpendicular direction, where $\nu = 0.2$ is the Poisson ratio [121]. This, in turn, leads to an increase of the lateral hopping interactions from t_1 to $t_{\perp} \approx t_1(1 + \gamma\nu\varepsilon)$.

In order to model the effect of lattice strain on the electronic structure of the nanoribbons, we first increase the lattice constant of the nanoribbon by ε and optimize the atomic positions from first-principles calculations and then perform the same Wannierization procedure discussed above to extract the hopping parameters. The hopping parameters are found to vary with the lattice strain as

$$t_i(\varepsilon) = t_i(0)e^{-\gamma[a_i(\varepsilon)/a_i(0)-1]}, \tag{3.18}$$

where $i = 1, 2, 3$ corresponds to the three distinct hopping interactions, $\gamma = 2.0$ is the spatial decay rate, and $a_i(\varepsilon)$ is the distance between i-th nearest neighbors in the nanoribbon under

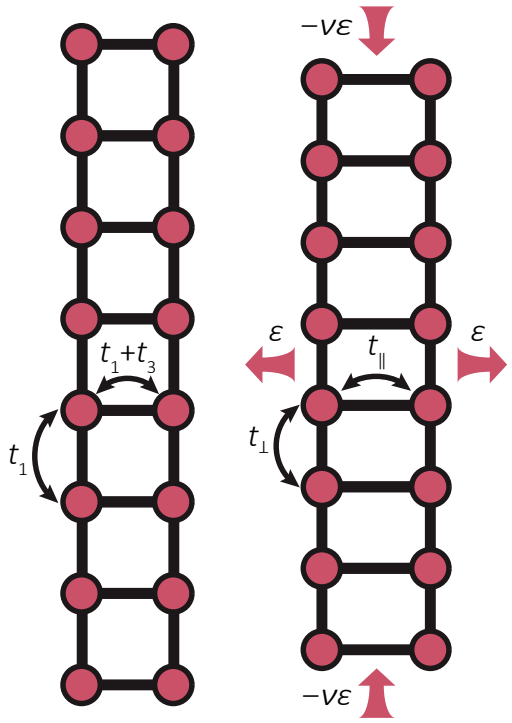


Figure 3.9: Illustration of the lattice strain exerted on the auxiliary model, resulting in the elongation ε in the periodic direction and compression $-\nu\varepsilon$ in the transverse direction, where ν is the Poisson ratio. Reprinted with permission from *Phys. Rev. Lett.* 2023, 130, 026401 [114]. Copyright 2023 American Physical Society.

tensile strain. A similar relationship describes how the change of the first nearest-neighbour hopping at the edges of the nanoribbon $\Delta t_1(\varepsilon)$ scales with the lattice strain.

In Fig. 3.10(a), we show that full control over the energy gap of AGNRs can be achieved by modulating the ratio between $t_\parallel$ and $t_\perp$ via lattice strain. Note that these calculations were performed using the complete tight-binding approximation of AGNRs rather than the auxiliary model. For each n, three regimes can be distinguished: (i) $t_\parallel > t_\perp$, where E_g decreases linearly as the value of $t_\parallel/t_\perp$ is reduced, (ii) $t_\parallel = t_\perp$, occurring at a critical strain ε_0, where the hidden symmetry is restored, E_g is quenched, and Dirac points develop at the Fermi level, and (iii) $t_\parallel < t_\perp$, where the energy gap increases linearly as the value of $t_\parallel/t_\perp$ is reduced further. Similarly to the energy gap, the critical strain, ε_0, follows an approximate inverse dependence on the nanoribbon width, w, as

$$\varepsilon_0(w) = \frac{\alpha}{w + \delta w}, \tag{3.19}$$

where $\alpha = 2.7\%\cdot$nm and $\delta w = 0.2$ nm, as extracted from the fitting given in Fig. 3.10(b). Earlier theoretical works predicted an analogous strain-dependence of the energy gaps of

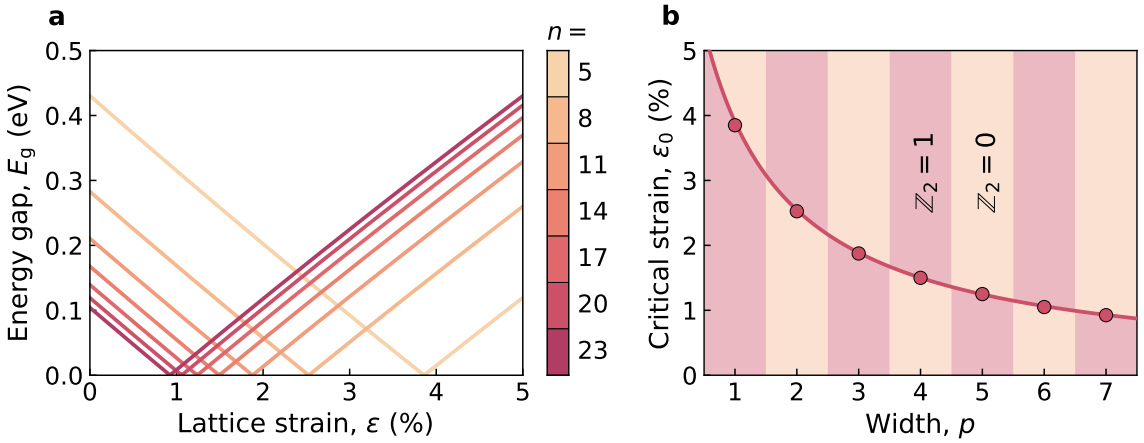


Figure 3.10: (a) Evolution of the energy gap, E_g, of AGNRs with $n = 3p + 2$ as a function of applied lattice strain, ε. (b) Evolution of the critical value of strain required to close the energy gap, ε_0, as a function of p; orange and red shaded areas denote trivial and topological insulating phases, respectively. Reprinted with permission from *Phys. Rev. Lett.* 2023, 130, 026401 [114]. Copyright 2023 American Physical Society.

AGNRs [122, 123], although the origin of these observations remained poorly understood. Our results provide an explanation to these otherwise elusive effects by connecting them to a hidden symmetry in the electronic structure of the nanoribbons.

3.3.2 Topological phase transitions and end states

Finally, to assess how the observed evolution of the energy gap as a function of strain affects the band topology of AGNRs, we determine the topological invariant, $\mathbb{Z}_2$, as [124]

$$(-1)^{\mathbb{Z}_2} = \prod_i \delta_i, \tag{3.20}$$

where $\delta_i = \pm 1$ is the parity of the ith band with respect to reflection across the nanoribbon width ($x \to -x$, where x is the periodic direction), with the product taken over all occupied bands. According to this definition, an even (odd) number of antisymmetric valence states yields $\mathbb{Z}_2 = 0$ ($\mathbb{Z}_2 = 1$), denoting a trivial (non-trivial) band topology. For unstrained AGNRs, $(-1)^{\mathbb{Z}_2} = (-1)^n$, so that the topology is strictly defined by the width, i.e., nanoribbons with an even (odd) n are topologically trivial (non-trivial) [124, 125].

Figure 3.10(b) shows the dependence of $\mathbb{Z}_2$ on the strength of the lattice deformation. The energy-gap closing and subsequent reopening driven by strain is accompanied by a change in

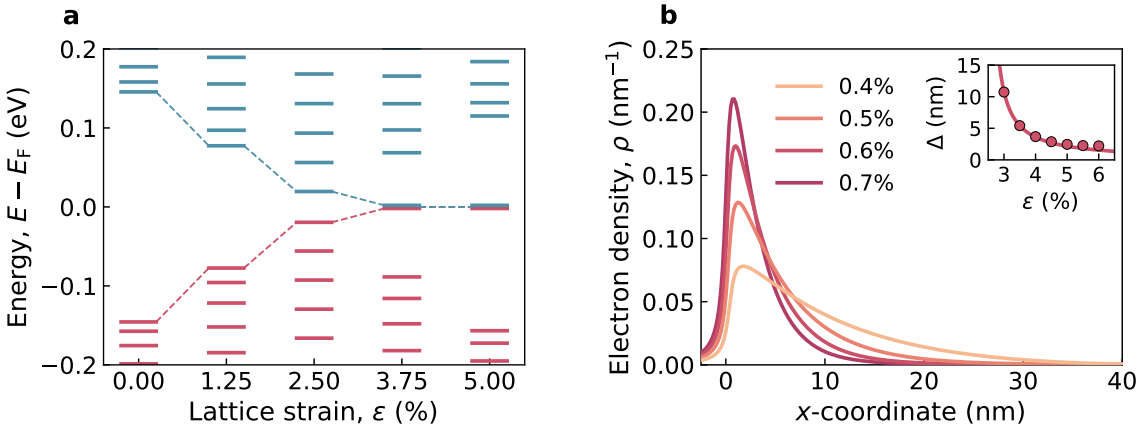


Figure 3.11: (a) Energy spectrum of a finite-size AGNR with $n = 8$ and length 50 nm as a function of ε. (b) Electron density of one of the two end states for increasing values of strain, visualized along the nanoribbon x-axis; the inset shows the decay length of the end states, Δ, as a function of the applied strain. Reprinted with permission from *Phys. Rev. Lett.* 2023, 130, 026401 [114]. Copyright 2023 American Physical Society.

$\mathbb{Z}_2$ between 0 and 1. This signals that topologically trivial nanoribbons become non-trivial, and vice versa. The observed topological quantum phase transition stems from the fact that the two states that form the band edges [cf. Fig. 3.7(c)] have opposite parities with respect to reflection across the width of the nanoribbon. When the strain is strong enough to exchange the energy ordering of these two bands, the total parity of the occupied bands flips and so does the topological invariant.

We further analyse the emergence of the topological phase transition by considering a finite-length nanoribbon, computationally treated as a big aromatic molecule. In Fig. 3.11(a), we present the effect of lattice strain on the energy spectrum of a representative topologically trivial finite-size ANGR of width $n = 8$ and length of 50 nm. The application of strain continuously reduces the energy gap, which eventually vanishes at the critical value $\varepsilon_0 = 2.5\%$, giving rise to a pair of zero-energy degenerate states. These are topologically protected *end* states (not to be confused with edge states) which, as shown in Fig. 3.11(b), selectively reside at the nanoribbon ends and are the hallmark of one-dimensional topological insulators [126–128]. Their electron density decays exponentially into the nanoribbon, $\rho(x) \propto e^{-x/\Delta}$, where Δ is the decay length. By fitting, we obtain that the decay length of these end states depends on strain according to the relation

$$\Delta = \frac{\Delta_0}{|\varepsilon - \varepsilon_0|}, \tag{3.21}$$

where $\Delta_0 = 0.054$ nm. Such end states can be experimentally probed through scanning tunneling spectroscopy [129].

3.4 Conclusions

In this Chapter, I have demonstrated that the electronic structure of armchair graphene nanoribbons of width $n = 3p + 2$ is dominated by a previously unidentified hidden symmetry. The energy-gap opening originates from the hidden-symmetry breaking induced by long-range hopping interactions between π-electrons and structural distortions occurring at the edges of the nanoribbon. The identification of this hidden symmetry enables the engineering of the properties of graphene nanoribbons through lattice deformations, which can give rise to Dirac points at the Fermi level, tunable energy gaps, and topological quantum phase transitions. To conclude, these findings present a novel interpretation of the semiconducting character of armchair graphene nanoribbons and provide means for the precise control of their functionalities.

Chapter 4

Graphene nanoribbons in an electric field

Graphene nanoribbons are widely regarded as promising building blocks for next-generation carbon-based devices. A critical issue to their prospective applications is whether and to what degree their electronic structure can be externally controlled. In this Chapter, I combine simple model Hamiltonians with extensive first-principles calculations to investigate the response of armchair graphene nanoribbons (AGNRs) to transverse electric fields. Such fields can be achieved either upon laterally gating the nanoribbon or incorporating ambipolar chemical co-dopants along the edges. I reveal that the field induces a semiconductor-to-semimetal transition, with the semimetallic phase featuring zero-energy Dirac fermions that propagate along the armchair edges. The transition occurs at a critical field that scales inversely with the width of the nanoribbons. These findings are universal to group-IV honeycomb lattices, including silicene and germanene nanoribbons, irrespective of the type of edge termination. Overall, these results create new opportunities to electrically engineer Dirac fermions in otherwise semiconducting graphene-like nanoribbons.

This Chapter draws heavily upon a research paper co-authored by me and published in *Nano Letters*:

> M. Pizzochero, **N. V. Tepliakov**, A. A. Mostofi, and E. Kaxiras. Electrically Induced Dirac Fermions in Graphene Nanoribbons. *Nano Lett.* **21**(21), 9332–9338 (2021). [Online]

Substantial portions of text included in this chapter were written collaboratively by all contributing authors. I contributed to the work by revealing the origin of the semiconductor-

to-semimetal phase transition, conducting tight-binding calculations, preparing figures, and leading the writing process.

4.1 Electric route to Dirac fermions

We begin by considering the response of hydrogen-terminated graphene nanoribbons to external electric fields from first principles. Our *ab initio* calculations are performed within the Density Functional Theory (DFT) framework [130], as implemented in the SIESTA package [111]. We use the gradient-corrected exchange and correlation functional devised by Perdew, Burke, and Ernzerhof (PBE) [107], although we thoroughly assessed that our results are insensitive to the exchange-correlation functional adopted, including the generalized gradient approximation (GGA) proposed by Perdew and Wang (PW91) [131], or the local density approximation (LDA) [132, 133].

The Kohn-Sham orbitals of the valence electrons are represented as a linear combination of atom-centered basis functions of double-ζ plus single polarization (DZP) quality. Core electrons are replaced by norm-conserving pseudopotentials generated following the scheme proposed by Troullier and Martins [135]. A mesh-cutoff of 400 Ry is used throughout. The integration over the one-dimensional Brillouin zone is carried out using a grid of 180 k-points, properly rescaled when considering supercells. The atomic coordinates are optimized at zero field until the maximum component of the atomic forces is smaller than 0.01 eV/Å.

We introduce an external electric field, E_{ext}, in the direction transverse to the axis of the nanoribbon. To this end, we add a sawtooth potential that increases linearly across the nanoribbon and changes discontinuously in the vacuum region between the periodic images of the nanoribbon. We ensure that the supercell in the calculations is large enough to exclude interactions between the periodic images, but we also avoid using supercells that are too large, as this may result in electrons tunneling out of the nanoribbon to the artifical potential wells formed by the discontinuities of the sawtooth potential in the vacuum regions. The transverse electric field in graphene nanoribbons can be realized experimentally in an open circuit split-gate configuration where the armchair edges of the nanoribbon are contacted to source and drain electrodes [136], as schematically illustrated in Fig. 4.1(a). The charge density shown in the same figure indicates that such an electric field drives a spatial separation

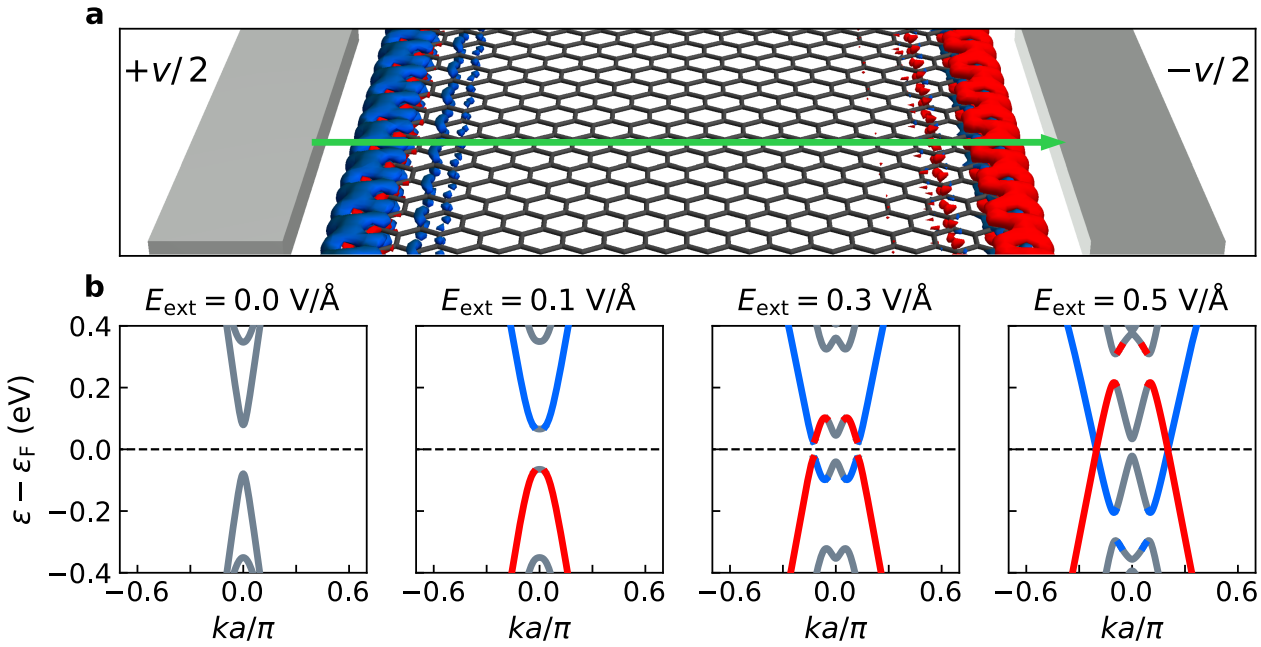


Figure 4.1: (a) Atomic structure of a hydrogen-terminated armchair graphene nanoribbon with $n = 33$ carbon atoms across the unit cell, immersed in a transverse external electric field. Such a field can be experimentally realized by laterally contacting the nanoribbon to source and drain electrodes, as illustrated. Red and blue isosurfaces represent the electron- and hole- charge density induced by the field. Isosurface values are set to ± 0.001 e/Å^3. (b) Band structures of AGNR at electric fields $E_{\text{ext}} = 0.0$, 0.1, 0.3, 0.5 V/Å. Red and blue lines indicate the bands that mainly originate from each of the two armchair edges of the nanoribbon, whereas the grey lines are the rest of the bands that do not have a pronounced localisation at the edge carbon atoms. Energies are referenced to the Fermi level, ε_{F}. Reprinted with permission from *Nano Lett.* 2021, 21, 21, 9332–9338 [134]. Copyright 2021 American Chemical Society.

of electrons and holes along the two edges of the nanoribbon.

In Fig. 4.1(b), we show the evolution of the band structure of a hydrogen-terminated armchair graphene nanoribbon of width $n = 33$ (or, in the unit of length, $w = 3.9$ nm, where $w = (n-1)\sqrt{3}d_{\text{C}}/2$ and $d_{\text{C}} = 1.42$ Å is the carbon-carbon bond length) as a function of E_{ext}. As the strength of the field increases, the band extrema reorganise by first narrowing and then quenching the direct energy gap, while the k-space location of the smallest gap shifts from $ka = 0$ to $ka \approx \pm 0.3\pi$. At $E_{\text{ext}} \approx 0.5$ V/Å, valence and conduction bands cross at the Fermi level, giving rise to zero-energy Dirac points. The projections of the band structure onto the carbon atoms that form the two armchair edges reveal that these linearly dispersing states are confined selectively on these edges, as is further confirmed by the local density of states

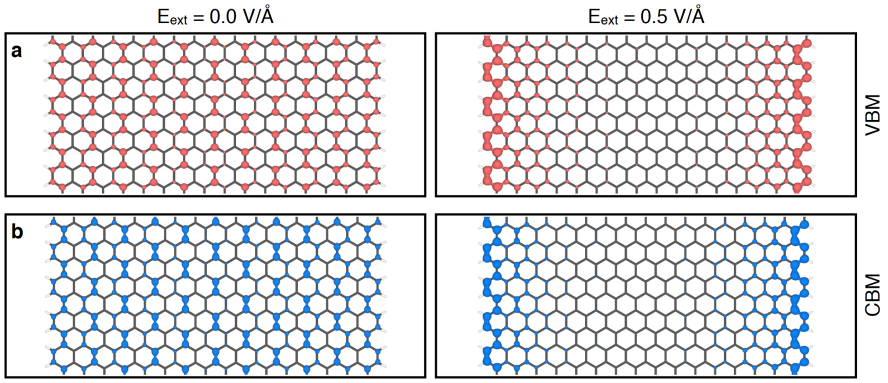


Figure 4.2: Local density of states (LDOS) of hydrogen-terminated graphene nanoribbons of width $n = 33$ at electric fields $E_{\text{ext}} = 0.0$ and 0.5 V/Å, evaluated in the vicinity (0.1 eV) of the valence band maximum (VBM; red colour) and conduction band minimum (CBM; blue colour), as obtained from first-principles calculations. In all cases, the isosurfaces enclose the same amount of charge density (30%). The electric field and the accompanying formation of the semimetallic phase promote a transition from a uniformly delocalised to a localised LDOS, with the localization primarily occurring along the cis-polyacetylene units that compose the armchair edges. Reprinted with permission from *Nano Lett.* 2021, 21, 21, 9332–9338 [134]. Copyright 2021 American Chemical Society.

shown in Fig. 4.2. This indicates that Dirac fermions with opposite Fermi velocities propagate along each of the two edges in AGNRs when subjected to a uniform external electric field.

To unveil the origin of the field-induced crossover from the semiconducting to the Dirac semimetallic phase, we rely on a tight-binding Hamiltonian of the π-electron network,

$$\mathcal{H} = \sum_i v_i c_i^\dagger c_i + \sum_{i,j} t_{ij}(c_i^\dagger c_j + \text{h.c.}), \tag{4.1}$$

where $c_i^\dagger$ and c_i are the fermion creation and annihilation operators, respectively, t_{ij} is the hopping integral between the ith and jth sites, and v_i is the on-site energy acting on the ith lattice site, which is used to control the strength of the applied external electric field. We include the first, second, and third nearest-neighbour hopping integrals with respective values of $t_1 = -2.70$ eV, $t_2 = -0.20$ eV, and $t_3 = -0.18$ eV [137, 138], and vary the strength and spatial distribution of v_i to examine its role on the electronic properties.

In Fig. 4.3(a), we consider a representative AGNR of width $n = 33$. To emulate the action of the electric field, we set the on-site energies such that they vary linearly from $v/2$ to $-v/2$ between the two armchair edges, with the edge on-site energy v being proportional to the electric field strength. The evolution of the band structure with increasing v is given

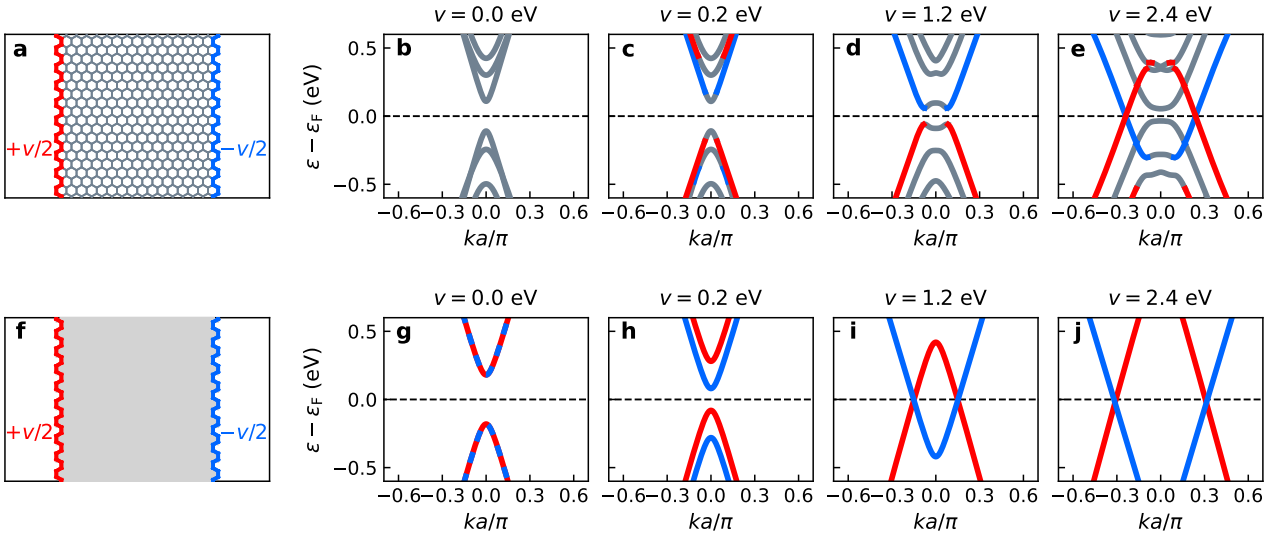


Figure 4.3: (a) Atomic structure of an AGNR of width $n = 33$, along with (b-e) its band structure with the on-site energies linearly varying from $v/2$ to $-v/2$ between the two edges. (f) Atomic structure of a pair of *cis*-polyacetylene chains, a simple model to describe the edges of an armchair graphene nanoribbon, along with (g-j) its electronic band structure upon the introduction of opposite on-site energies $\pm v/2$ on the two chains. Results obtained from the tight-binding Hamiltonian given in Eq. (4.1). Red and blue lines indicate the bands that mainly originate from each of the two *cis*-polyacetylene chains composing the armchair edges of the nanoribbon. Energies are referenced to the Fermi level, ε_F. Reprinted with permission from *Nano Lett.* 2021, 21, 21, 9332–9338 [134]. Copyright 2021 American Chemical Society.

in Fig. 4.3(b-e). As on-site energies increase, the energy gap of the system decreases and eventually vanishes, yielding band crossing at the Fermi level. As evidenced by the projections of the energy bands, on-site energies of opposite signs cause electrons to redistribute from one edge to the other through the inner sites of the nanoribbon, leading to gapless Dirac states.

To further clarify the emergence of these Dirac states, we consider a simple model consisting of a pair of parallel *cis*-polyacetylene chains, as shown in Fig. 4.3(f). This system can be regarded as the simplest description of the edges of AGNRs. We assume that the electronic subsystems of the two chains do not interact, but electrons can redistribute between the chains if their Fermi levels are different. At vanishing on-site energies, the band structure shown in Fig. 4.3(g) consists of doubly degenerate valence and conduction bands that, similar to AGNRs, have an energy gap at the center of the Brillouin zone [14]. Upon the introduction of opposite potentials $\pm v/2$ on the two chains, the four bands split into two

sets, as displayed in Fig. 4.3(h–j). Importantly, the top of the valence band of one chain shifts to higher energies, while the bottom of the conduction band of the other chain shifts to lower energies. As a result, the energy gap of the system reduces and ultimately closes at large enough values of v, with the linearly dispersing bands of the two chains crossing at the Fermi level. Hence, opposite on-site energies induce a semimetallic phase featuring two Dirac points located at equivalent off-symmetry points of the Brillouin zone. Although each *cis*-polyacetylene chain is individually insulating, the inter-chain redistribution of electrons allows the formation of the semimetallic phase. The analogy between Dirac points in the armchair edges of a graphene nanoribbon and *cis*-polyacetylene chains is made clear by the comparison of Fig. 4.3(e) with Fig. 4.3(i). In both cases, the semimetallic states are localized on each of the two armchair chains of carbon atoms. These conceptually simple models illustrate that the onset of the field-induced Dirac semimetallic phase in otherwise semiconducting AGNRs traces back to edges having charges of opposite sign and the resulting band shifts.

4.2 Role of width and chemical composition

We generalize our findings by systematically addressing the dependence of the semiconductor-to-semimetal transition on the width of hydrogen-terminated AGNRs. In Fig. 4.4(a–c), we trace the energy gap, ε_g, as a function of an increasing electric field for over thirty nanoribbons of widths ranging from $n = 11$ ($w = 1.2$ nm) to $n = 43$ ($w = 5.1$ nm), grouped according to whether $n = 3p$, $3p + 1$, or $3p + 2$. Note that these and all of the following results are obtained at the DFT level of theory. Independently of the width, ε_g reduces and eventually closes at large enough E_{ext}. As the electrostatic potential between the two edges is proportional to their separation, w, the critical field required to develop the semimetallic phase, E_{crit}, decreases as the nanoribbon widens [136]. The dependence of the critical field on the width is shown in Fig. 4.4(d–f), where we observe that, within each class, E_{crit} is inversely proportional to the width of the nanoribbon,

$$E_{\text{crit}} = \frac{V_{\text{crit}}}{w} = \frac{2V_{\text{crit}}}{\sqrt{3}d_{\text{C}}(n-1)}, \tag{4.2}$$

with V_{crit} being the critical potential required to close the energy gap. Fitting the first-principles results with Eq. (4.2), we obtain $V_{\text{crit}} = 22.45$, 18.69 and 10.87 V for armchair

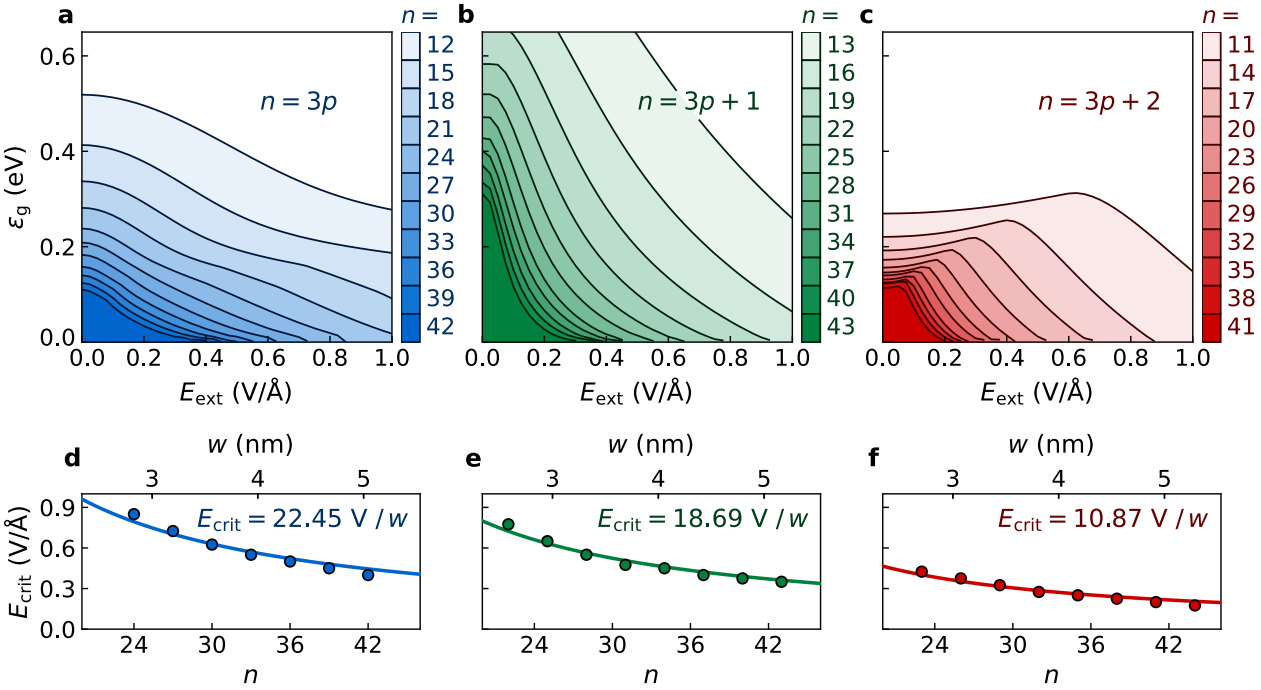


Figure 4.4: (a–c) Energy gaps, ε_{g}, of hydrogen-terminated armchair graphene nanoribbons as a function of an increasing electric field, E_{ext}. Depending on their width, n, AGNRs are classified into the (a) $n = 3p$, (b) $n = 3p + 1$, and (c) $n = 3p + 2$ classes, with p being a positive integer. (d–f) Evolution of the critical field, E_{crit}, required to close the energy gap as a function of the width of the nanoribbon for the (d) $3p$, (e) $3p + 1$, and (f) $3p + 2$ classes. Circles represent first-principles results while solid lines are the fit with Eq. (4.2) to extract the class-dependent critical potential, V_{crit}. Reprinted with permission from *Nano Lett.* 2021, 21, 21, 9332–9338 [134]. Copyright 2021 American Chemical Society.

graphene nanoribbons pertaining to the $n = 3p$, $3p + 1$, and $3p + 2$ classes, respectively. We thus envision that wider graphene nanoribbons belonging to the $3p + 2$ class are optimally suited to electrically access Dirac fermions due to the occurrence of the semimetallic phase at the smallest fields.

Our results are not restricted to hydrogen-terminated AGNRs. Motivated by the rapid experimental progress in the synthesis of halogen-terminated nanoribbons [139, 140], we assess the influence of fluorine and chlorine edge-passivations of AGNRs on the Dirac semimetallic phase, as shown in Fig. 4.5(a). The evolution of their band structure and energy gap with E_{ext} is presented in Fig. 4.5(b, c). No appreciable differences are observed as compared to their hydrogen-terminated counterparts, thereby suggesting that the type of edge termination does not affect the formation of the semimetallic phase. It is crucial to note that this

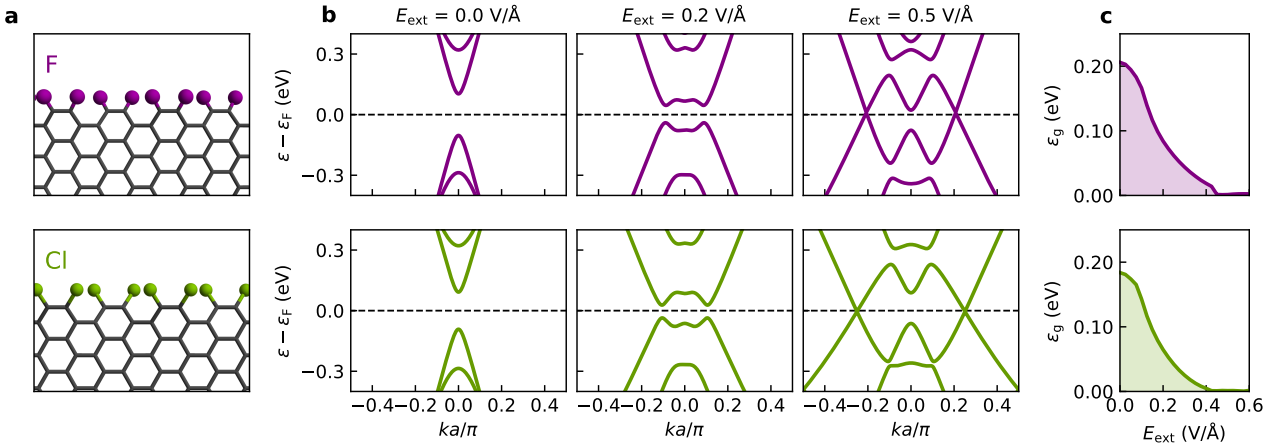


Figure 4.5: (a) Atomic structure of fluorine- and chlorine-terminated armchair graphene nanoribbons, (b) their band structures at width $n = 33$ in an external electric fields of strength $E_{\text{ext}} = 0.0$, 0.2, and 0.5 V/Å, along with (c) the evolution of their energy gap, ε_{g}, with E_{ext}. Energies in the band structures are referenced to the Fermi level, ε_{F}. Reprinted with permission from *Nano Lett.* 2021, 21, 21, 9332–9338 [134]. Copyright 2021 American Chemical Society.

conclusion may no longer hold if the opposite edges of the nanoribbon are terminated with different chemical species, which could create a built-in transverse electric field, interfering with the external electric field. This possibility is explored in great detail in the next Chapter of this Thesis.

We have further explored additional monovalent terminations of varied electronegativities, including hydroxylated (-OH), amminated (-NH_2), and hydroborated (-BH_2) nanoribbons. Figure 4.6 shows that similar to F- and Cl-terminated AGNRs, these graphene nanoribbons are also capable of developing the semimetallic phase in sufficiently strong electric fields. We therefore conclude that the field-assisted phase transition is robust with respect to the functional group used to passivate the carbon atoms at the edges.

To further illustrate that this field-induced transition to the Dirac semimetal is of a general nature, we investigate heavier group-IV congeners of graphene nanoribbons, *i.e.*, silicene and germanene nanoribbons [141, 142]. These nanostructures have been recently fabricated on silver substrates via epitaxial growth [143–145], and subsequently integrated as active channels into electronic devices in various configurations [146, 147]. Figure 4.7(a) displays the atomic structure of hydrogen-terminated silicene and germanene nanoribbons. Unlike carbon, the arrangement of silicon and germanium atoms in a honeycomb lattice is unstable in a planar geometry, and is subject to a structural distortion that consists of a relative out-

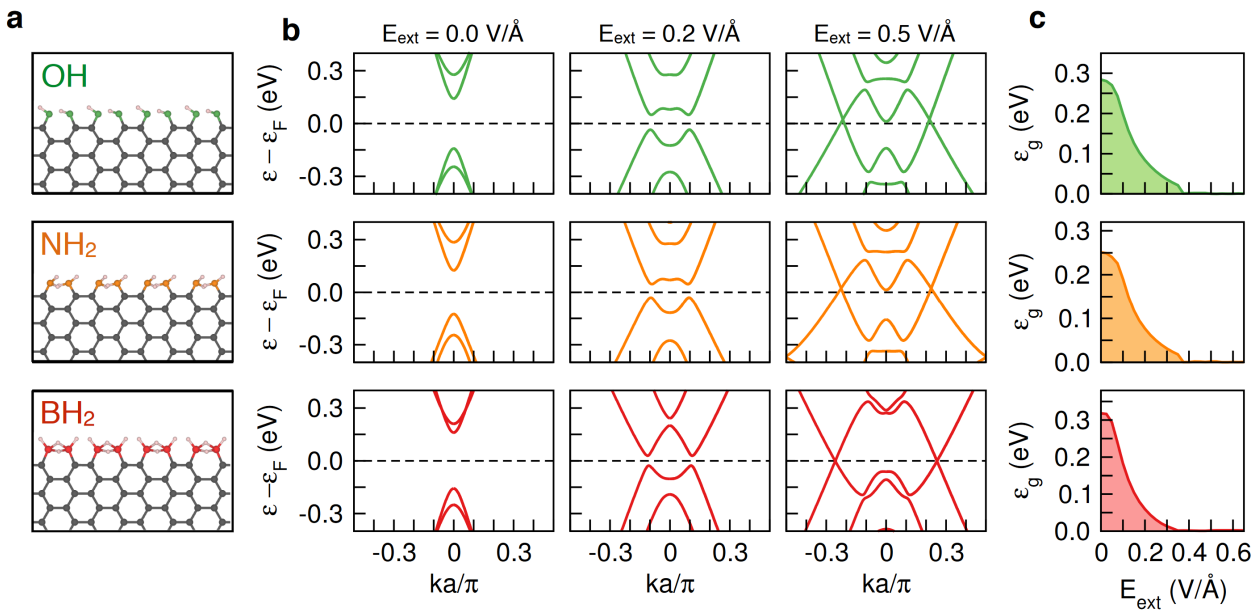


Figure 4.6: (a) Top view of the atomic structure of the edges of OH-, NH_2-, and BH_2-terminated armchair graphene nanoribbon, along with (b) their band structures at electric fields of $E_{\text{ext}} = 0.0$, 0.2, and 0.5 V/Å, and (c) evolution of the energy gap (ε_{g}) as a function of increasing electric fields. Energies in the band structures are referenced to the Fermi level (ε_{F}). Reprinted with permission from *Nano Lett.* 2021, 21, 21, 9332–9338 [134]. Copyright 2021 American Chemical Society.

of-plane displacement of the two sublattices by 0.53 Å and 0.63 Å, respectively [148, 149]. Despite the marked difference in the crystal structure, the field-induced semiconductor-to-semimetal transition is preserved, as evident from Fig. 4.7(b, c). The energy gap closes at weaker critical fields than in the case of graphene nanoribbons. The reason for this is that, for a given n, silicene and germanene nanoribbons are wider (larger w) than AGNRs owing to the longer bond distance ($d_{\text{Si}} = 2.30$ Å and $d_{\text{Ge}} = 2.44$ Å *vs.* $d_{\text{C}} = 1.42$ Å), resulting in a larger potential difference between the edges of the nanoribbon at a given electric field strength. Altogether, these findings demonstrate a reversible electric control over Dirac fermions in this family of graphene-like nanoribbons regardless of their chemical composition, provided that the armchair edges of the honeycomb lattice and the ensuing π-electron network are retained.

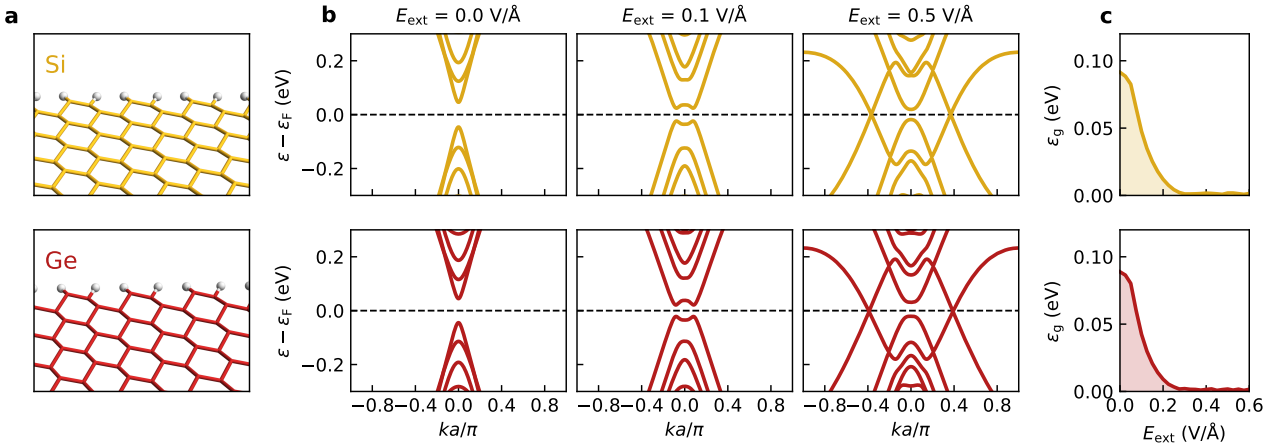


Figure 4.7: (a) Atomic structure of hydrogen-terminated armchair silicene and germanene nanoribbons, (b) their band structures at width $n = 33$ at fields of strength $E_{\text{ext}} = 0.0, 0.1$, and 0.5 V/Å, and (c) the evolution of energy gap ε_{g} with E_{ext}. Energies in the band structures are referenced to the Fermi level, ε_{F}. Reprinted with permission from *Nano Lett.* 2021, 21, 21, 9332–9338 [134]. Copyright 2021 American Chemical Society.

4.3 Chemical route to Dirac fermions

Finally, we propose an alternative, chemical approach for creating Dirac fermions in AGNRs. Instead of relying on an external electric field, we consider the incorporation of n-type impurities into one edge of the nanoribbon and p-type impurities into the other, effectively leading to an intra-ribbon p-n junction and an accompanying transverse internal field. This qualitatively corresponds to the physical realization of the simple tight-binding model explored above, where edges of opposite polarities were considered; see Fig. 4.3(a, b) and related discussion. In Fig. 4.8(a), we show the atomic structure of an AGNR with $n = 33$ ($w = 3.9$ nm) patterned with two arrays of boron and nitrogen dopants. We remark that advances in the on-surface synthesis enable atomically precise incorporations of heteroatoms in graphene nanoribbons [150], including periodically arranged nitrogen [151, 152] or boron atoms, [153, 154] as well as their co-doping [155].

For a given width of the nanoribbon, the strength of the internal field resulting from the spatial separation of electrons and holes can be quantified through the density of the chemical dopants hosted in the lattice, $\theta = [n_{\text{X}}/(n_{\text{X}} + n_{\text{C}})]\,\%$, where n_{X} and n_{C} are the total numbers of dopant and carbon atoms in the nanoribbon, respectively. In Fig. 4.8(b–d), we show the band structure of a hydrogen-terminated AGNR co-doped with boron and nitrogen atoms at

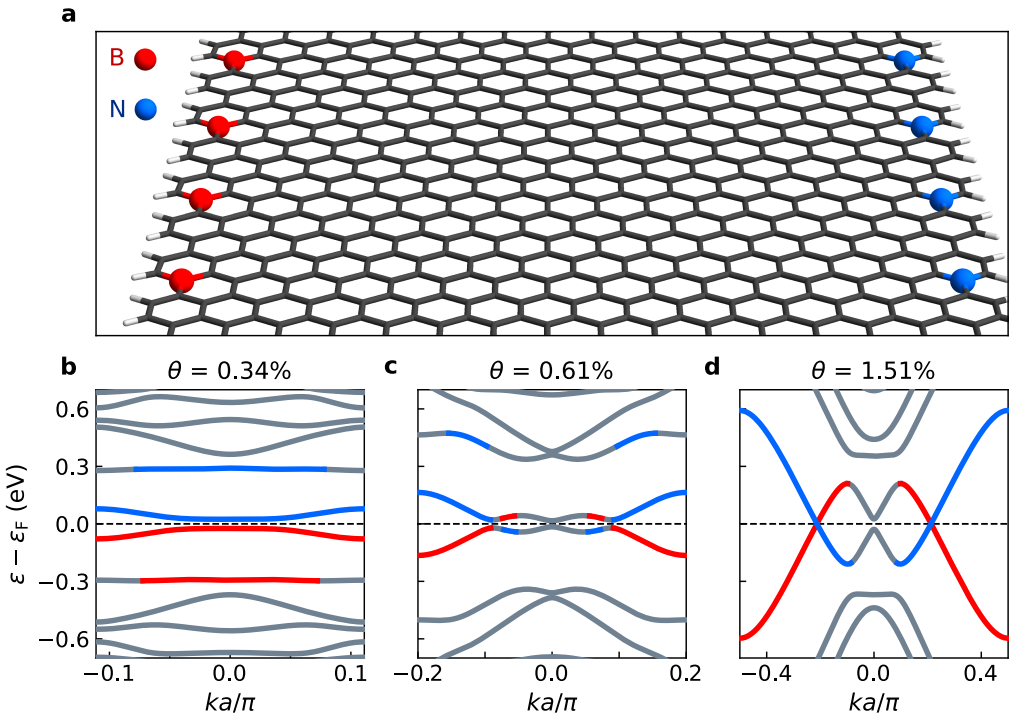


Figure 4.8: Dirac fermions in graphene nanoribbons induced by chemical co-doping. (a) Atomic structure of a hydrogen-terminated armchair graphene nanoribbon of width $n = 33$ patterned with an array of boron and nitrogen dopants, at a representative co-dopant density $\theta = 1.51\%$. (b-d) Band structures of co-doped AGNR at increasing $\theta = 0.34$, 0.61, and 1.51%. Red, blue, and grey lines indicate the projections of the bands onto the B, N, and C atoms, respectively. Energies are referenced to the Fermi level, ε_F. Reprinted with permission from *Nano Lett.* 2021, 21, 21, 9332–9338 [134]. Copyright 2021 American Chemical Society.

$\theta = 0.33$, 0.61 and 1.51%. Upon ambipolar co-doping, we observe a rearrangement of the bands around the Fermi level, similar to that induced through the application of the external electric field; *cf.* Fig. 4.1(b). The Dirac semimetallic phase emerges at dopant densities exceeding $\sim 1.5\%$, with the linearly crossing bands mainly arising from the heteroatoms. This Dirac semimetallicity has the same general origin as in the graphene nanoribbons exposed to transverse electric field. It is therefore also possible to achieve semiconductor-to-semimetal phase transition in graphene nanoribbons by means of chemical doping, avoiding the need for external electric fields.

4.4 Conclusions

In this Chapter, I have demonstrated that semiconducting armchair graphene nanoribbons develop a Dirac semimetallic phase under a transverse electric field. Such a field can be achieved by laterally gating the nanoribbon or by introducing n- and p-type dopants along the nanoribbon edges. The semimetallic phase features linearly dispersing bands crossing at the Fermi level and hosts zero-energy Dirac fermions propagating along the nanoribbon edges. The semiconductor-to-semimetal transition occurs at critical fields that scale inversely with the nanoribbon width and is universal to group-IV armchair nanoribbons, including silicene and germanene nanoribbons, irrespective of the edge passivation. The work presented in this Chapter opens new avenues to electrically engineer Dirac fermions in this broad family of one-dimensional nanostructures.

Chapter 5

Graphene nanoribbon/hexagonal boron nitride heterojunctions

Half-metals have been envisioned as active components in spintronic devices by virtue of their completely spin-polarized electrical currents. Actual materials hosting half-metallic phases, however, remain scarce. In this Chapter, I predict that recently fabricated heterojunctions of zigzag nanoribbons embedded in two-dimensional hexagonal boron nitride are half-semimetallic, featuring fully spin-polarized Dirac points at the Fermi level. The half-semimetallicity originates from the transfer of charges from hexagonal boron nitride to the embedded graphene nanoribbon. These charges give rise to opposite energy shifts of the states residing at the two edges while preserving their intrinsic antiferromagnetic exchange coupling. Upon doping, an antiferromagnetic-to-ferrimagnetic phase transition occurs in these heterojunctions, with the sign of the excess charge controlling the spatial localisation of the net magnetic moments. These findings demonstrate that such heterojunctions realise tunable one-dimensional conducting channels of spin-polarised Dirac fermions seamlessly integrated into a two-dimensional insulator, thus holding promise for the development of carbon-based spintronics.

This Chapter draws heavily upon a research paper co-authored by me and published in *Nano Letters*:

> **N. V. Tepliakov**, R. Ma, J. Lischner, E. Kaxiras, A. A. Mostofi, M. Pizzochero. Dirac Half-Semimetallicity and Antiferromagnetism in Graphene Nanoribbon/Hexagonal Boron Nitride Heterojunctions. *Nano Lett.* **23**(14), 6698–6704 (2023). [Online]

Substantial portions of text included in this chapter were written collaboratively by all contributing authors. I contributed to the work by analysing first-principles calculations, developing the tight-binding model, revealing the origin of the half-semimetallic phase, proposing the existence of the ferrimagnetic phase in doped heterojunctions, preparing figures, and writing the text.

The results reported in this chapter served as a basis for a follow-up research paper, focussing on heterojunctions in which the graphene nanoribbon embedded in hexagonal boron nitride is terminated by atoms of the same type at the both edges. This research paper was also published in *Nano Letters*:

> M. Pizzochero, **N. V. Tepliakov**, J. Lischner, A. A. Mostofi, E. Kaxiras. One-Dimensional Magnetic Conduction Channels across Zigzag Graphene Nanoribbon/Hexagonal Boron Nitride Heterojunctions. *Nano Lett.* **24**(22), 6521–6528 (2024). [Online]

I contributed to this follow-up work by conducting additional tight-binding calculations, preparing figures, and assisting in the writing process.

5.1 Electronic structure of ZGNR/hBN heterojunctions

The electronic properties of graphene nanoribbons and heterojunctions proposed in this Chapter will be assessed using a combination of first-principles methods and tight-binding modelling. The *ab initio* calculations reported in this Chapter are based on density-functional theory (DFT), as implemented in the SIESTA package [111, 130]. We adopt the gradient-corrected approximation to the exchange-correlation functional proposed by Perdew, Burke, and Ernzerhof [107], but have explicitly verified that our results are robust with respect to this choice, as will be shown later. The Kohn-Sham valence orbitals are expanded in a linear combination of atom-centered basis functions at the single-ζ plus single polarization level.

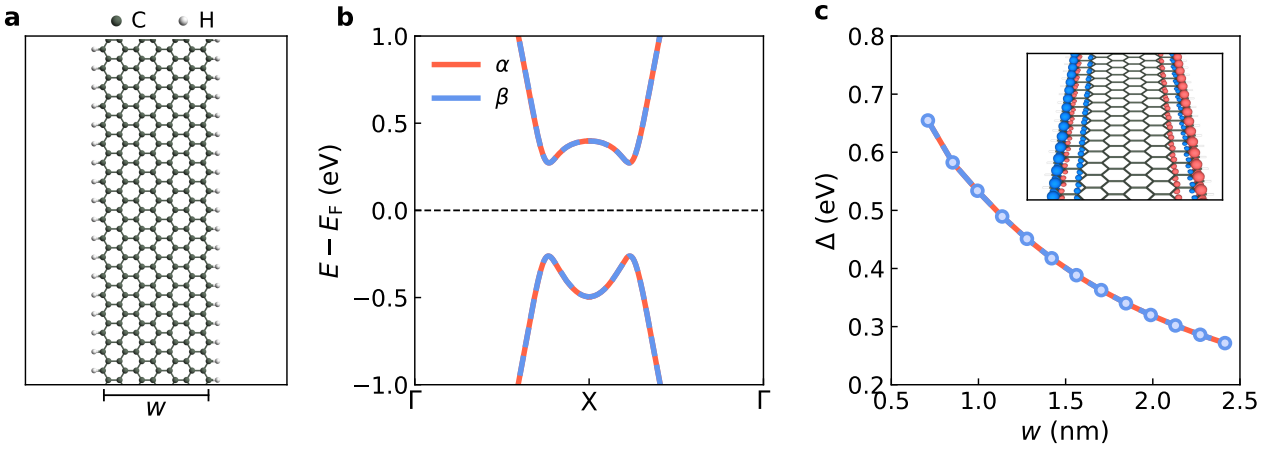


Figure 5.1: (a) Atomic structure of a hydrogen-terminated ZGNR of width $w = 1.4$ nm, which is periodic and infinite in the vertical direction. (b) Band structure of the hydrogen-terminated ZGNR shown in panel (a); red and blue lines denote α- and β-spin bands; energies are referenced to the Fermi level E_{F}. (c) Band gaps Δ of hydrogen-terminated ZGNRs as a function of the width w. The inset in panel (c) shows the spin density of a hydrogen-terminated ZGNR for $w = 1.4$ nm; red and blue contours represent α- and β-spin density. Reprinted with permission from *Nano Lett.* 2023, 23, 14, 6698–6704 [157]. Copyright 2023 American Chemical Society.

Atomic nuclei and core electrons are represented by norm-conserving pseudopotentials generated according to the Troullier-Martins scheme [135]. We use a mesh cutoff of 300 Ry for all calculations except for the Bader charge analysis [156], for which this value is increased to 500 Ry. The integration over the Brillouin zone is carried out using a grid of $1 \times 15 \times 1$ k-points (y is the periodic direction) for all calculations but the density of states, for which the grid is increased by a factor of 80 in the periodic direction. The atomic structure is relaxed at charge neutrality until the maximum force component on each atom is lower in magnitude than 0.02 eV/Å.

We begin by recalling the well-known electronic and magnetic properties of free-standing zigzag graphene nanoribbons (ZGNRs), whose edges are terminated by hydrogen atoms. The atomic structure of a ZGNR for a representative width of 1.4 nm is given in Figure 5.1(a). In DFT calculations, ZGNRs are constrained by orthorhombic supercells of dimensions $a = 86.92$ Å, $b = 2.46$ Å, and $c = 20.00$ Å that ensure enough vacuum space between the periodic replicas of the nanoribbon. Unlike armchair graphene nanoribbons studied in previous chapters, ZGNRs feature π-electron magnetism. In the antiferromagnetic phase, ZGNRs possess width-independent magnetic moments of $0.27\,\mu_{\mathrm{B}}$ per unit cell that are localized at the edge

carbon atoms. The magnetic moments align parallel along each edge of the nanoribbon and antiparallel across opposite edges. The total magnetic moment of the unit cell is thus zero.

The inter-edge antiferromagnetic exchange coupling, obtained as the difference in energy between parallel and antiparallel spin orientations, is 3.64 meV. In line with Lieb's theorem for the repulsive Hubbard model on a bipartite lattice at half filling [158], this leads to a ground state with zero total magnetisation, as evident from the spin-density pattern shown in the inset of Figure 5.1(c). The antiferromagnetic ordering of the edge-localized magnetic moments in ZGNRs results in the spin-degenerate band structure shown in Figure 5.1(b), which exhibits a direct band gap. As reported in Figure 5.1(c), the magnitude of the energy gap decreases monotonically as the width of the nanoribbon increases due to the weakening of confinement effects. Hence, hydrogen-terminated ZGNRs are semiconducting and antiferromagnetic regardless of their width.

We next proceed to modelling recently fabricated heterojunctions consisting of zigzag graphene nanoribbons embedded in hexagonal boron nitride (hBN). Figure 5.2(a) shows the atomic structure of a ZGNR/hBN heterojunction in which the nanoribbon has the same width of 1.4 nm as before. In DFT calculations, the lattice constant of ZGNR/hBN heterojunctions is constrained to that of hexagonal boron nitride, 2.51 Å. The model consists of orthorhombic supercells of size $a = 86.92$ Å, $b = 2.51$ Å, and $c = 20.00$ Å. This ensures enough vacuum space in the direction perpendicular to the plane of the heterojunction and also guarantees that the sheets of hBN are large enough to be considered two-dimensional.

Because of the structural topology of the ZGNR, its incorporation into hBN enforces a connectivity pattern such that the carbon atoms along opposite edges of the nanoribbon are covalently bonded to boron and nitrogen atoms, as seen in Figure 5.2(a). The hBN matrix does not modify the spin density distribution, where edge-localized magnetic moments retain an antiparallel alignment that leads to a zero net magnetization, as shown in the inset of Figure 5.2(c). Compared to hydrogen-terminated ZGNR, the magnetic moment is lowered to $0.19\,\mu_{\mathrm{B}}$ per unit cell, with the antiferromagnetic exchange coupling reduced to 2.41 meV.

The electronic band structure of the ZGNR/hBN heterojunction is qualitatively different from that of hydrogen-terminated ZGNR. In particular, the ZGNR/hBN heterojunction exhibits the spin-split band structure shown in Figure 5.2(b), where the α-spin electrons are semimetallic and β-spin are semiconducting. The crossing of the α-spin energy bands forms

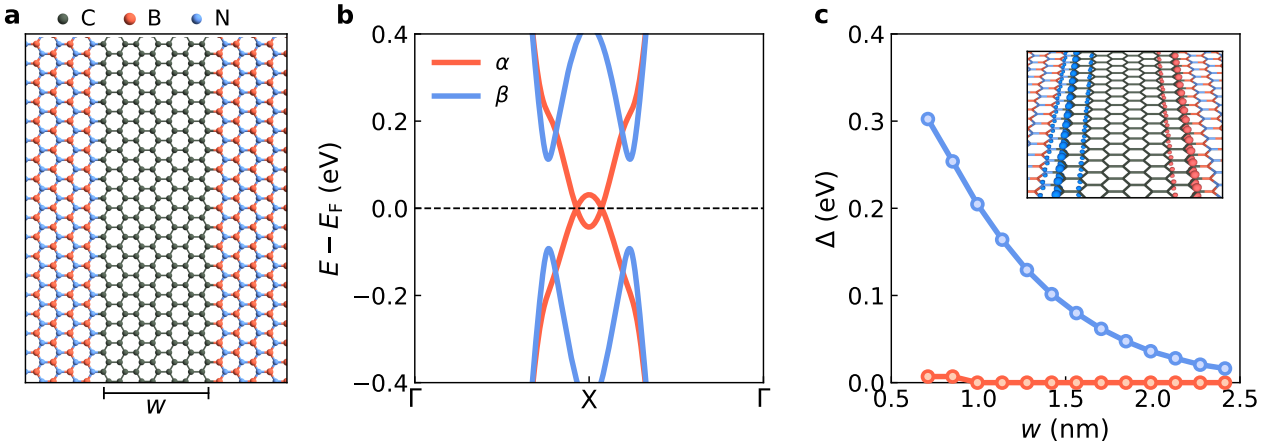


Figure 5.2: (a) Atomic structure of a ZGNR/hBN heterojunction comprising a ZGNR of width $w = 1.4$ nm embedded in a two-dimensional hBN matrix. (b) Band structure of the ZGNR/hBN heterojunction shown in panel (a). (c) Band gaps Δ of ZGNR/hBN heterojunctions as a function of the ZGNR width w. The inset in panel (c) shows the spin density of a ZGNR/hBN heterojunction for $w = 1.4$ nm; red and blue contours represent α- and β-spin density. Reprinted with permission from *Nano Lett.* 2023, 23, 14, 6698–6704 [157]. Copyright 2023 American Chemical Society.

Dirac points at the Fermi level, with a corresponding Fermi velocity of 1.2×10^5 m/s, approximately one order of magnitude lower than that of monolayer graphene [164]. This is the hallmark of Dirac half-semimetallicity [165] which, as shown by the red curve in Figure 5.2(c), is insensitive to the width of the nanoribbon embedded in hBN. Hence, ZGNR/hBN heterojunctions host an unconventional Dirac half-semimetallic antiferromagnetic phase [166], where a spin-split band structure, typical of ferromagnets, coexists with fully compensated magnetization, typical of antiferromagnets [167].

Given the unique nature of the half-semimetallic phase in ZGNR/hBN heterojunctions, it is crucial to thoroughly explore its stability with respect to various parameters of the calculations. In Fig. 5.3, we show that the band structures of ZGNR/hBN heterojunctions are practically independent of the choice of the DFT functional used, with the notable exception of the simplest local-density approximation. Given the slight mismatch between the lattice constants of free-standing ZGNRs and hBN (2.46 Å vs. 2.51 Å, respectively), it is also important to check that the half-semimetallic phase is robust with respect to the application of a moderate lattice strain. In Fig. 5.4, we show that the band structures of ZGNR/hBN with marginally different lattice constants are practically equivalent.

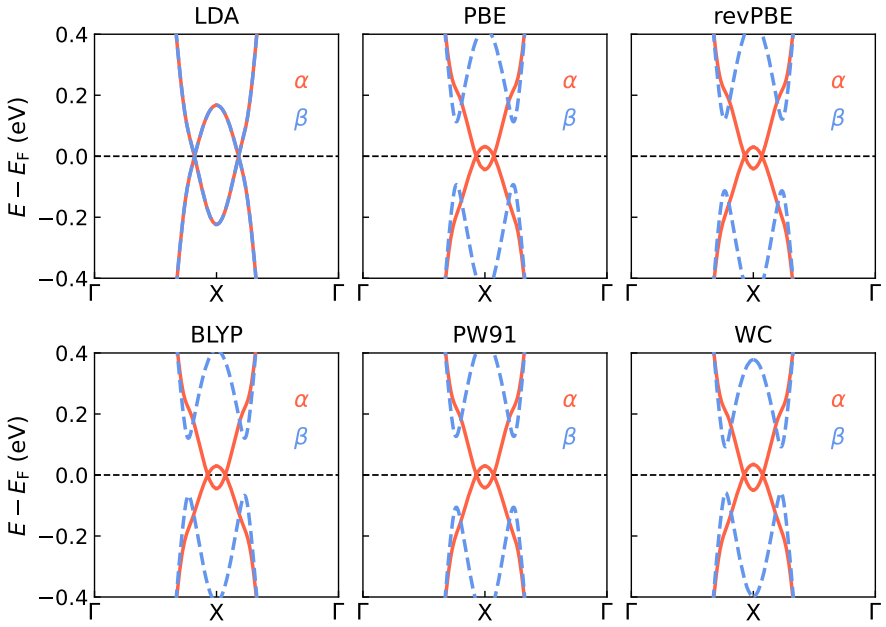


Figure 5.3: Band structure of a zigzag graphene nanoribbon of width $w = 1.4$ nm embedded in hexagonal boron nitride, as obtained at the density-functional theory level for different exchange-correlation functionals, i.e., LDA [132, 133], PBE [107], revPBE [159], BLYP [160–162], PW91 [131], and WC [163]. Reprinted with permission from *Nano Lett.* 2023, 23, 14, 6698–6704 [157]. Copyright 2023 American Chemical Society.

It is also important to stress that the structural models of ZGNR/hBN heterojunctions adopted in our *ab initio* calculations ensure a large lateral distance between periodic replicas of the embedded graphene nanoribbon. For example, in the case of a ZGNR of width $w = 1.4$ nm, discussed throughout the text, this distance is 73 Å. Because of the large spatial separation between adjacent nanoribbons, each ZGNR can be considered to be isolated in the two-dimensional sheet of hexagonal boron nitride. Hence, we ensure that our models closely resemble the experimental situation where graphene nanoribbons are grown in two-dimensional hexagonal boron nitride [53, 54]. In this way, our approach is different from previous works, where ZGNR/hBN heterojunctions were typically described as periodically repeated, alternated strips of hBN and ZGNR [55–57] or as a single interface in a hybrid hBN/ZGNR nanoribbon [58].

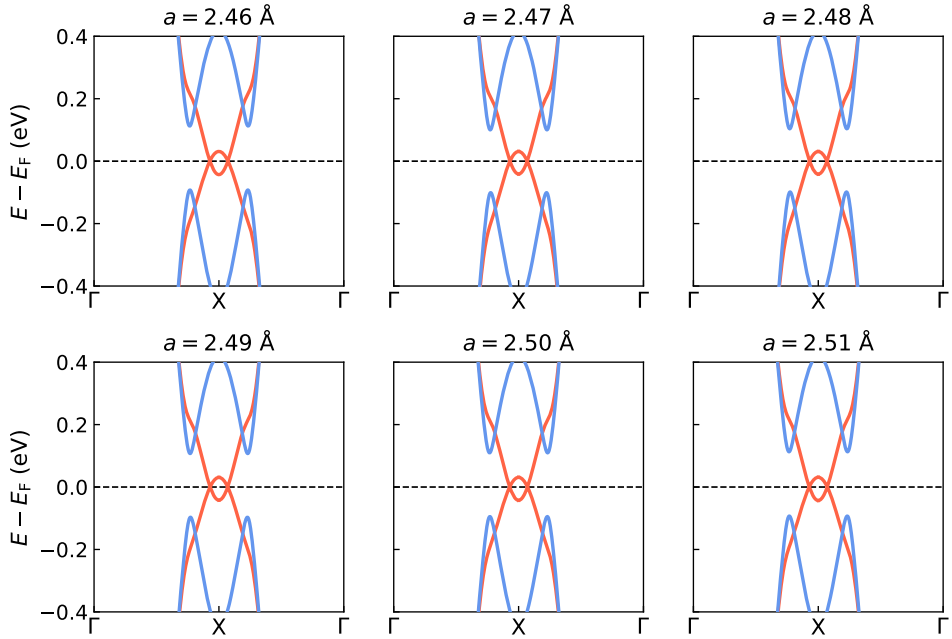


Figure 5.4: Electronic band structure of a zigzag graphene nanoribbon of width $w = 1.4$ nm embedded into hexagonal boron nitride for different values of lattice constant a. Reprinted with permission from *Nano Lett.* 2023, 23, 14, 6698–6704 [157]. Copyright 2023 American Chemical Society.

5.2 Origin of half-semimetallicity in ZGNR/hBN heterojunctions

Having established the presence of Dirac half-semimetallicity in ZGNR/hBN heterojunctions, we now proceed to uncover the origin of this peculiar electronic phase. In Figure 5.5(a), we show the atomic charges residing at each carbon atom in the ZGNR/hBN heterojunction with $w = 1.4$ nm, as obtained from an analysis based on Bader's theory of atoms in molecules [156]. Carbon atoms on the edges of the nanoribbon are negatively charged when bonded to boron atoms and positively charged when bonded to nitrogen atoms. This is a consequence of the difference in electronegativity between these elements [168]. We can then speculate that the emergence of the half-semimetallic phase in the ZGNR/hBN heterojunctions traces back to this charge transfer occurring at the two interfaces between the constituent materials. Because of the formation of an array of point-like charges of opposite polarity at the spatially-separated edges, a built-in electric field develops in the in-plane direction perpendicular to the periodic direction of the heterojunction. The half-semimetallicity arises from the energy shifts of opposite signs caused by the built-in electric field, which lifts

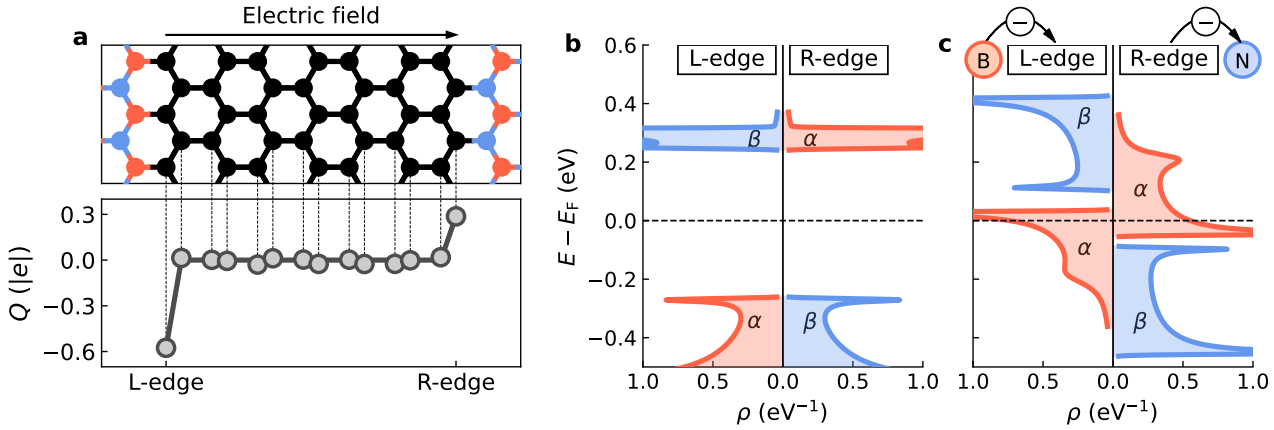


Figure 5.5: (a) Atomic charges Q at each carbon atom across the ZGNR/hBN heterojunction with $w = 1.4$ nm; in the upper panel, blue, red, and black spheres indicate nitrogen, boron, and carbon atoms, respectively. (b) Density of states ρ of hydrogen-terminated ZGNRs projected onto the carbon atoms at the left (L-) and right (R-) edge of the nanoribbon. (c) Projected density of states of the ZGNR/hBN heterojunction, where electrons transferred from boron-to-carbon (carbon-to-nitrogen) atoms at the interface between hBN and the L-edge (R-edge) of ZGNR induce an upward (downward) energy shift of each pair of edge states. Reprinted with permission from *Nano Lett.* 2023, 23, 14, 6698–6704 [157]. Copyright 2023 American Chemical Society.

the degeneracy of the localized edge states.

According to Fig. 5.5(b), the electronic density of states projected onto the edge carbon atoms of a free-standing ZGNR is spin-polarised, but the energies of the electronic states on the opposite edges are equivalent. In ZGNR/hBN heterojunctions, however, the negatively charged edge of the ZGNR shifts the α-spin valence band and β-spin conduction band towards *higher* energies; see Fig. 5.5(c). At the same time, the positively charged edge shifts the α-spin conduction band and β-spin valence band towards *lower* energies. Consequently, the energy gap of the α-spin closes, forming the half-semimetallic phase.

This is qualitatively analogous to the external field effect in hydrogen-terminated armchair graphene nanoribbons [134, 169, 170], investigated in Chapter 4 of this Thesis, but here the behavior is driven by intrinsic charge transfer resulting from embedding the ZGNR in a two-dimensional hBN matrix. Our results are consistent with previous calculations performed on superlattices consisting of alternating graphene and hexagonal boron nitride nanoribbons [55–57, 59] and lend support to the experimental observation of a finite electronic conductance at the Fermi level in these heterojunctions [53]. Importantly, the half-semimetallic

phase is not observed in the case of armchair graphene nanoribbons embedded in hBN, as carbon atoms at both of their edges are terminated with both B- and N-atoms. This does not create a charge imbalance between the opposite edges of the nanoribbon, necessary to lift the spin degeneracy of the energy bands, and AGNRs embedded in hBN retain their semiconducting electronic properties.

5.3 Mean-field Hubbard model

To gain insight into the origin of the half-semimetallicity in ZGNR/hBN heterojunctions and further elucidate the role of charge transfer in the magnetic states at the zigzag edges, we develop a simple and intuitive model restricted to the π-electron network of ZGNRs. This model is described by the following mean-field Hubbard model (MFHM) Hamiltonian [167, 171],

$$\hat{\mathcal{H}} = t \sum_{\langle i,j\rangle,\sigma} \left[\hat{c}^{\dagger}_{i\sigma}\hat{c}_{j\sigma} + \text{h.c.}\right] + \sum_{i,\sigma} \epsilon_i \hat{c}^{\dagger}_{i\sigma}\hat{c}_{i\sigma} + U \sum_{i} \left[\hat{n}_{i\uparrow}\langle\hat{n}_{i\downarrow}\rangle + \langle\hat{n}_{i\uparrow}\rangle\hat{n}_{i\downarrow}\right], \tag{5.1}$$

where $\hat{c}_{i\sigma}$ and $\hat{c}^{\dagger}_{i\sigma}$ are the annnihilation and creation operators, respectively, for a p_z-electron with spin σ at lattice site i (h.c. denotes the Hermitian conjugate), t is the hopping between nearest-neighboring lattice sites i and j, ϵ_i is the on-site potential at lattice site i, $\hat{n}_{i\sigma} = \hat{c}^{\dagger}_{i\sigma}\hat{c}_{i\sigma}$ is the spin density at lattice site i, and U is the strength of the on-site Coulomb repulsion between a pair of p_z-electrons residing at the same lattice site. We use $U = |t|$, which is obtained from fitting *ab initio* calculations [172] and experimental observations on sp^2-hybridized carbon chains [173]. To emulate the charge transfer of opposite signs at the interfaces between hBN and ZGNR in the actual heterojunction, we set $\epsilon = \epsilon_1 > 0$ along the sites forming one edge, $\epsilon = \epsilon_2 < 0$ along the sites forming the other edge, and $\epsilon = 0$ otherwise. Our model is sketched in Figure 5.6(a).

The mean-field Hubbard Hamiltonian given in Eq. (5.1) is solved self-consistently. To that end, we begin by considering $\epsilon_i = 0$ and initializing the electron density $\langle\hat{n}_{i,\sigma}\rangle$ such that the spins residing at the different edges of the nanoribbon have an antiparallel orientation. We solve the Hamiltonian iteratively to obtain the converged electron densities $\langle\hat{n}_{i,\sigma}\rangle$. Next, we introduce the on-site potentials ϵ_i as a first-order perturbation to the energies of electronic states. This is possible even when the energy bands cross at the Fermi level due to the localization of the corresponding states at the opposite edges of the nanoribbon, which results

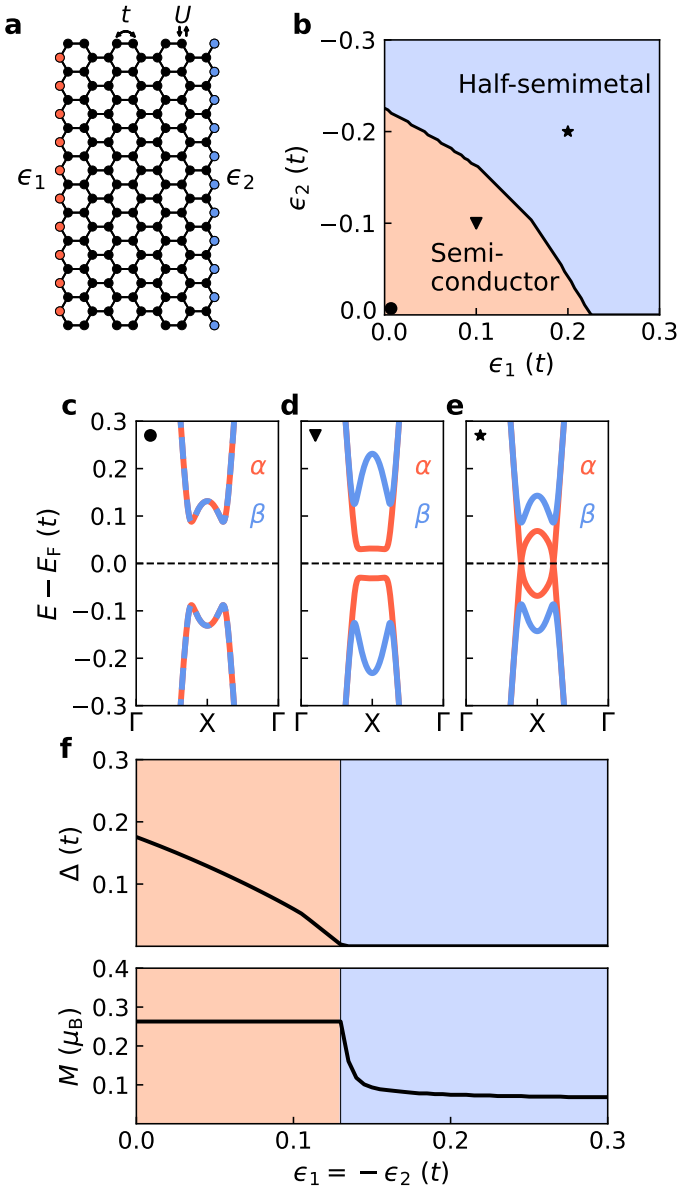


Figure 5.6: (a) Schematic representation of the mean-field Hubbard model used to describe a ZGNR embedded in hBN; black, red, and blue dots denote lattice sites with on-site potentials of $\epsilon = 0$, $\epsilon = \epsilon_1$, and $\epsilon = -\epsilon_2$ respectively; t is the nearest-neighbor hopping amplitude and U is the on-site Coulomb repulsion energy of a pair p_z-electrons residing at the same lattice site. (b) Electronic phase diagram of ZGNR as a function of on-site potentials ϵ_1 and ϵ_2 on the edges; red and blue shaded areas correspond to semiconducting and half-semimetallic phases, respectively. Representative band structures of ZGNR are shown when (c) $\epsilon_1 = \epsilon_2 = 0$, (d) $\epsilon_1 = -\epsilon_2 = 0.1t$, and (e) $\epsilon_1 = -\epsilon_2 = 0.2t$; red and blue lines denote α-spin and β-spin energy bands, respectively. (f) Energy gaps Δ and magnetic moments per carbon atom on the edge M as a function of on-site potentials $\epsilon_1 = -\epsilon_2$. In all the panels, the width of the nanoribbon is $w = 1.4$ nm. Reprinted with permission from *Nano Lett.* 2023, 23, 14, 6698–6704 [157]. Copyright 2023 American Chemical Society.

in vanishing matrix elements coupling these bands. Finally, we re-calculate the electron densities $\langle \hat{n}_{i,\sigma} \rangle$, which may have changed due to the crossing of energy bands at the Fermi level, and perform a final diagonalization of the model Hamiltonian.

Using this model Hamiltonian, we track the evolution of the spin-dependent energy gap as a function of ϵ_1 and ϵ_2. This allows us to derive the electronic phase diagram shown in Figure 5.6(b). Depending on the magnitude of the charge residing at the edge carbon atoms in the ZGNRs, we identify three phases, all of them with zero net magnetization: (i) a spin-degenerate semiconducting phase at $\epsilon_1 = \epsilon_2 = 0$, with finite and equal α-spin and β-spin energy gaps; see Figure 5.6(c); (ii) a spin-split semiconducting phase at, e.g., $\epsilon_1 = -\epsilon_2 = 0.1t$, with a finite α-spin energy gap that is smaller than the β-spin energy gap; see Figure 5.6(d); and (iii) a half-semimetallic phase at, e.g., $\epsilon_1 = -\epsilon_2 = 0.2t$, with a vanishing α-spin energy gap and finite β-spin energy gap; see Figure 5.6(e).

The full phase diagram for both positive and negative ϵ_1 and ϵ_2 is given in Fig. 5.7. Note that Fig. 5.6(b) corresponds to the bottom right quadrant of the full phase diagram, i.e., the region of $\epsilon_1 > 0$ and $\epsilon_2 < 0$. It is seen from the full phase diagram that the termination of the graphene nanoribbon's edges with the charges of the same sign can potentially give rise to the third, metallic electronic phase. This can be realised in ZNGR/hBN heterojunctions by flipping one of the sheets of hBN, so that both edges are terminated by either B or N atoms [174]. Lateral integration of ZGNRs with hexagonal boron nitride thus allows realisation of three different electronic phases — semiconducting, metallic, and half-semimetallic — within a family of closely-related one-dimensional nanostructures that can be connected via in-plane integration.

Although we focus on the representative ZGNR of width $w = 1.4$ nm, the phase diagrams shown in Figures 5.6(b) and 5.7 are found to be independent of w. This is explained by the fact that the built-in electric field induced by boron and nitrogen atoms terminating the opposite edges of the ZGNR in the heterojuntion scales inversely with the width, and so does the energy gap of the nanoribbon [cf. Figure 5.1(c)]. Owing to this, the critical potential required to close the energy gap for one spin orientation is width-independent. By fitting the phase diagram, we obtain that the critical potential is given by $(\epsilon_1 + a)^2 + (\epsilon_2 - a)^2 = b^2$, where $a = 0.19t$ and $b = 0.45t$. Thus, the charge transfer from hBN to ZGNR is large enough to enforce the Dirac half-semimetallicity in ZGNR/hBN heterojunctions at any nanoribbon

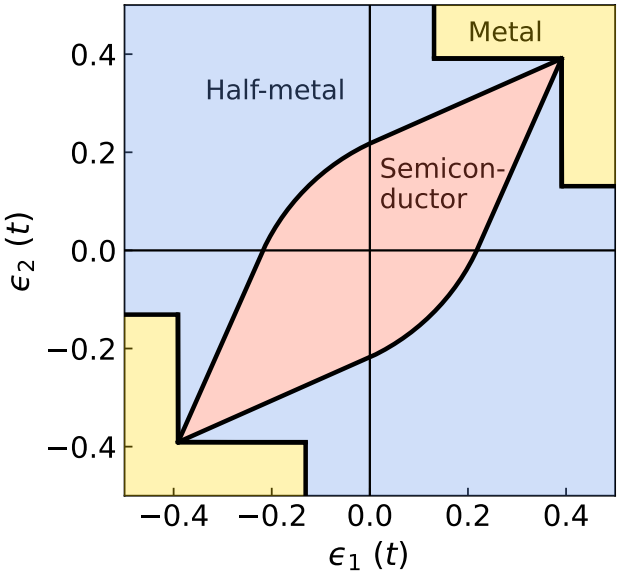


Figure 5.7: Global electronic phase diagram of ZGNR of width $w = 1.4$ nm as a function of on-site potentials ϵ_1 and ϵ_2 on the edges, as obtained from the mean-field Hubbard model Hamiltonian. Red, blue, and yellow shaded areas indicate semiconducting, half-metallic, and metallic phases, respectively. Note that Figure 5.6(b) corresponds to the bottom right quadrant of this extended phase diagram. Reprinted with permission from *Nano Lett.* 2023, 23, 14, 6698–6704 [157]. Copyright 2023 American Chemical Society.

width [cf. Figure 5.2(c)]. Notably, the phase diagrams in Figure 5.7 indicates that a half-metallic phase in the nanoribbon can appear when the potential is exerted only on one of the two edges of the nanoribbon. However, as evident from both *ab initio* and tight-binding results shown in Figure 5.8, a single interface between ZGNR and hBN is not sufficient to induce the Dirac half-semimetallic phase in the nanoribbon, which retains a small energy gap [58].

As shown in Figure 5.6(f), the onset of the half-semimetallic phase is accompanied by an abrupt decrease of the magnetic moments on the edge atoms from $0.26\,\mu_{\mathrm{B}}$ to $0.07\,\mu_{\mathrm{B}}$, consistent with the *ab initio* calculations previously discussed. This reduction of the magnetization can be understood from the electronic band diagrams in Figure 5.5(c): the energy gap closing results in a transfer of a fraction of α-spin electrons to the edge occupied by β-spin electrons, thereby partially quenching the magnetic moment on the both edges.

Although we set $U/t = 1$ in the MFHM calculations, we have additionally investigated the interplay between the model parameters U/t and ϵ, as shown in Figure 5.9. It is clear

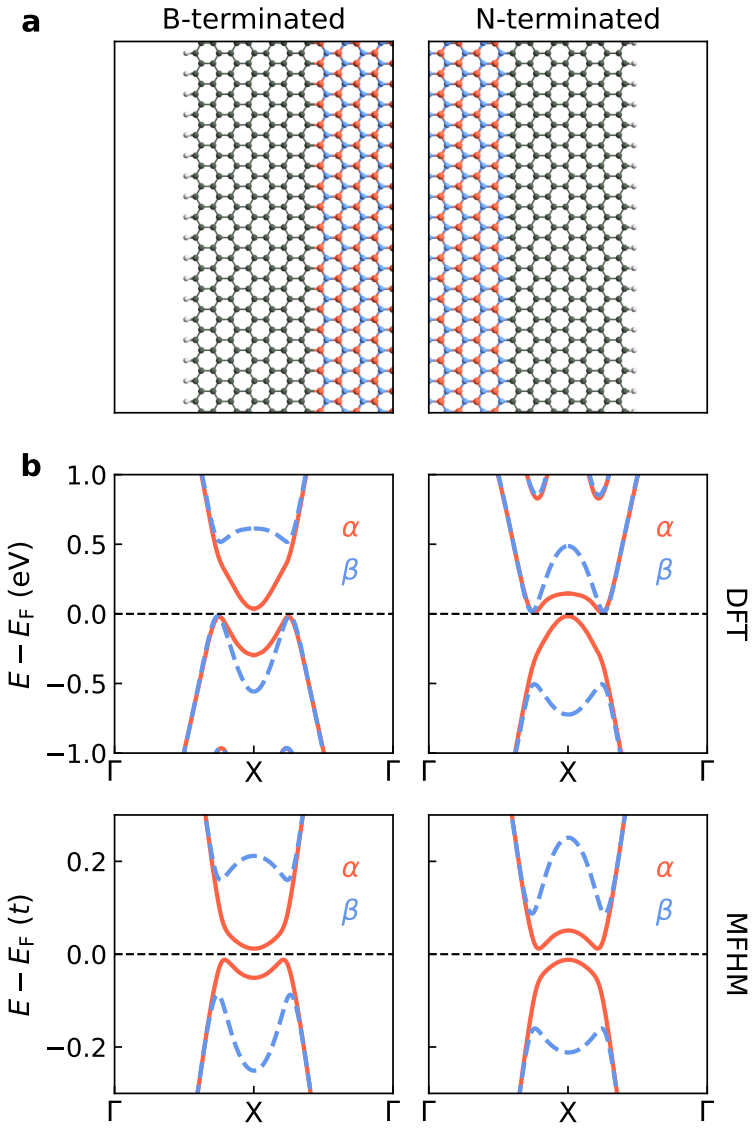


Figure 5.8: (a) Atomic structure of a zigzag graphene nanoribbon (ZGNR) of width $w = 1.4$ nm connected to hexagonal boron nitride on one edge and terminated with hydrogen atoms on the other edge [58]. Left and right panels show two different cases in which the edge of the ZGNR is terminated with either B or N atoms. Red, blue, black, and white spheres denote boron, nitrogen, carbon, and hydrogen atoms, respectively. (b) Electronic band structure of the B- and N-terminated ZGNR, calculated using density-functional theory (DFT) and mean-field Hubbard model (MFHM). The value of electron-electron repulsion in the MFHM is set to $U = t$, where t is the nearest-neighbor hopping integral; the edge potentials for B-terminated ZGNRs are set to $\epsilon_1 = 0.2t$ and $\epsilon_2 = 0$, whereas N-terminated ZGNRs have $\epsilon_1 = 0$ and $\epsilon_2 = -0.2t$. Reprinted with permission from *Nano Lett.* 2023, 23, 14, 6698–6704 [157]. Copyright 2023 American Chemical Society.

that larger values of electron-electron repulsion U make it more difficult to close the energy gap for α-spin electrons, which requires higher edge potentials ϵ to achieve the half-

semimetallicity.

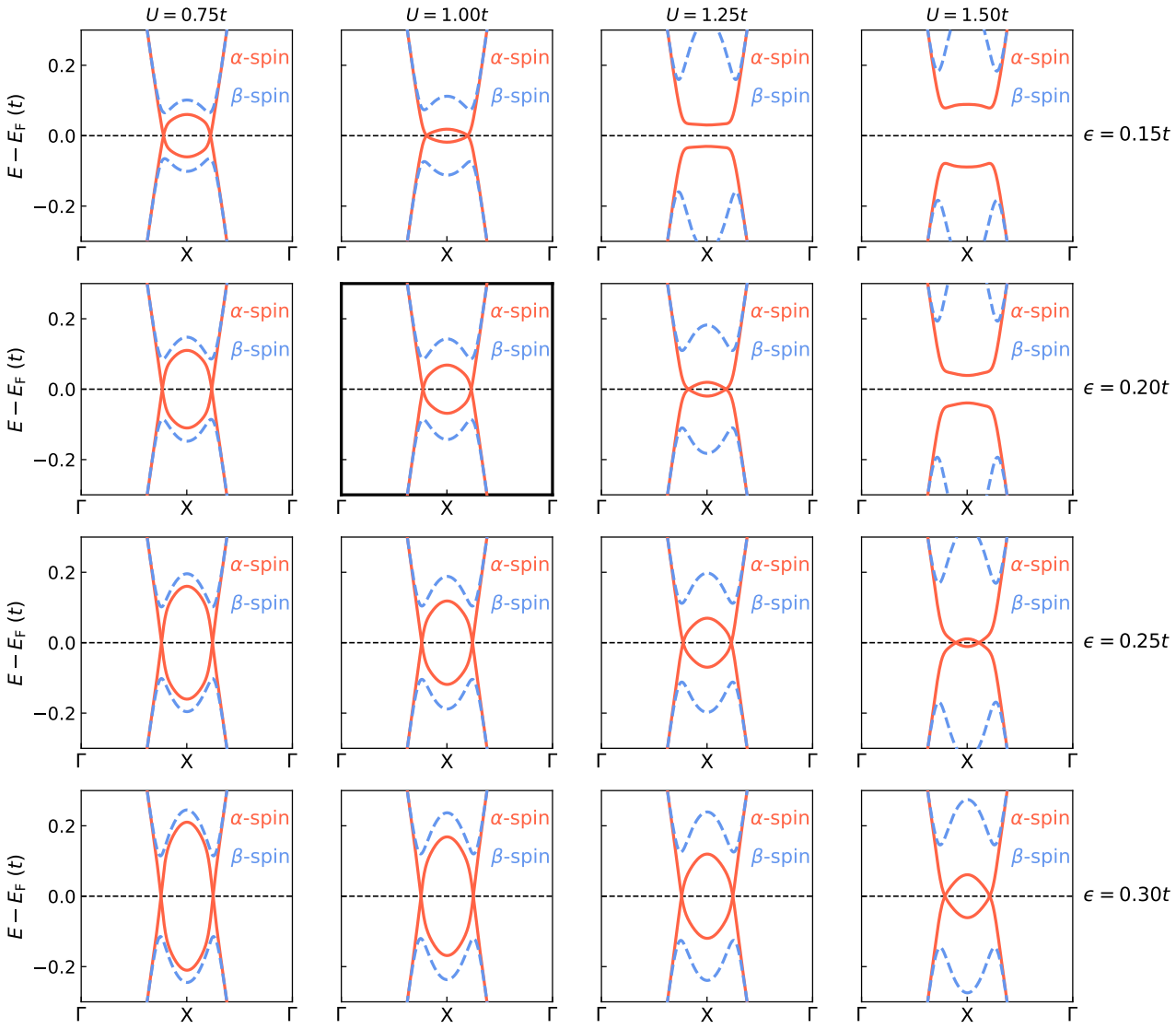


Figure 5.9: Band structure of a zigzag graphene nanoribbon of width $w = 1.4$ nm embedded in hexagonal boron nitride, as obtained using the mean-field Hubbard model Hamiltonian, for increasing values of electron-electron repulsion U and potentials on the two edges set to $\epsilon_1 = -\epsilon_2 = \epsilon$. All parameters are expressed in units of the nearest-neighbor hopping integral t. The case with $U = t$ and $\epsilon = 0.2t$, highlighted with the bold bounding box, corresponds to the choice of parameters adopted in rest of the calculations. Reprinted with permission from *Nano Lett.* 2023, 23, 14, 6698–6704 [157]. Copyright 2023 American Chemical Society.

5.4 Doping of ZGNR/hBN heterojunctions

The electronic and magnetic properties of the ZGNR/hBN heterojunctions can be extensively modified through charge doping. In Figure 5.10(a), we show the evolution of the band structure of a representative heterojunction as a function of excess charge q. The half-metallic character of the heterojunction is robust with respect to both p-type ($q > 0$) and n-type ($q < 0$) doping, as only α-spin energy bands cross the Fermi level. However, a non-trivial effect is observed in β-spin energy bands upon doping, which is not limited to a rigid energy shift. Specifically, n-type (p-type) doping shifts selectively the β-spin conduction (valence) bands towards the Fermi level, while leaving the position of the valence (conduction) bands unchanged. This occurs because the excess charge alters only the density of α-spin states, which affects the electron-electron repulsion experienced by β-spin states, but not vice versa.

Because the excess charge only affects the density of α-spin states, doped ZGNR/hBN heterojunctions acquire non-vanishing net magnetic moments due to the resulting imbalance between the α- and β-spin states, as shown in Figure 5.10(b). Remarkably, depending on whether the heterojunction is n- or p-doped, such net magnetic moments develop on either one or the other edge of the nanoribbon. According to the diagram of the electronic density of states given in Figure 5.5(c), the valence (conduction) band of the α-spin electrons is localized on the left, boron-terminated edge (right, nitrogen-terminated edge) of the nanoribbon. Hence, p-type (n-type) doping increases the magnetic moments residing at the left (right) edge, thus enabling an electrical modulation of their spatial localization. This effect is well captured by both *ab initio* and mean-field Hubbard model calculations.

Overall, as depicted in Figure 5.10(c), charge doping in ZGNR/hBN heterojunctions drives a transition from an *antiferromagnetic* ground state, where the magnetic moments at the two edges of the nanoribbon feature antiparallel orientation and equal magnitude, to a *ferrimagnetic* ground state. In the latter state, the magnetic moments at the edges of the nanoribbon retain an antiparallel orientation, but their difference in magnitude results in a global spin polarization [175]. This is opposed to hydrogen-terminated ZGNRs, where the antiferromagnetic and spin-degenerate ground state is unchanged upon charge doping due to the spin-degeneracy of the band structure, as shown in Fig. 5.11. Embedding ZGNRs into an hBN matrix is thus an effective strategy to achieve electrical control of their magnetism.

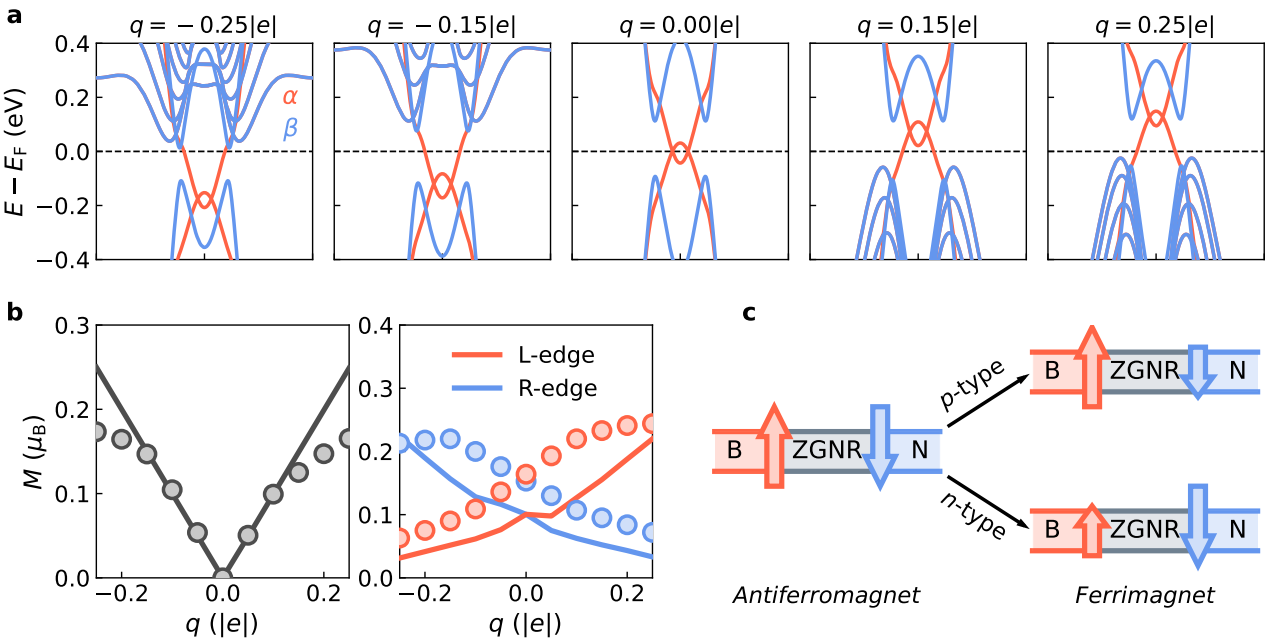


Figure 5.10: (a) Band structures of a ZGNR of width $w = 1.4$ nm embedded in hBN for an increasing amount of excess charge q per unit cell of the nanoribbon; red and blue lines denote α-spin and β-spin energy bands; the results are obtained at the density functional theory (DFT) level. (b) Dependence of the net magnetic moment per unit cell M (left panel) and magnetic moments at the carbon atoms forming the left, boron-terminated and the right, nitrogen-terminated edge of the ZGNR (right panel), on q; circles denote results obtained at the DFT level, whereas solid lines denote results obtained using the mean-field Hubbard model Hamiltonian. (c) Schematics of the doping-induced antiferromagnetic-to-ferrimagnetic phase transition in the ZGNR/hBN heterojunctions. Reprinted with permission from *Nano Lett.* 2023, 23, 14, 6698–6704 [157]. Copyright 2023 American Chemical Society.

5.5 Conclusions

In this Chapter, I investigated the electronic structure of recently fabricated heterojunctions consisting of zigzag graphene nanoribbons embedded in hexagonal boron nitride. I predict that these heterojunctions host a peculiar combination of Dirac half-semimetallicity and antiferromagnetism, where a fully compensated magnetization coexists with a spin-polarization of the charge carriers that arises from a Dirac semimetallic behavior in one spin orientation and a semiconducting behavior in the other. This unconventional electronic phase originates from the charge transfer of opposite polarity at the edges of the zigzag graphene nanoribbon which, in turn, leads to an energy shift of opposite signs of the otherwise spin-degenerate edge states. I have additionally shown that charge doping induces an antiferromagnetic-to-

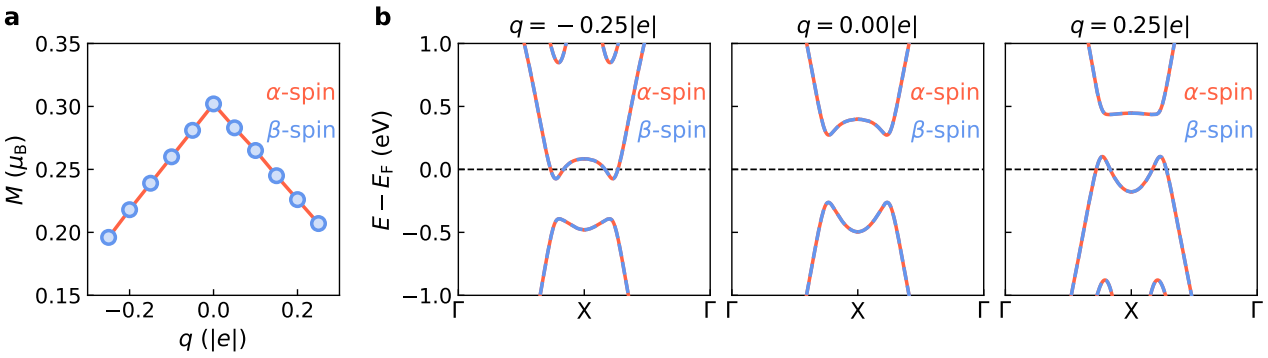


Figure 5.11: (a) Magnetic moments M localized at the edges of a hydrogen-terminated zigzag graphene nanoribbon (ZGNR) of width $w = 1.4$ nm as a function of the excess charge q. (b) Band structure of doped, hydrogen-terminated ZGNR for different values of q. The data is obtained using density functional theory calculations. Red and blue colors denote α- and β-spin contributions, respectively. Energies are referenced to the Fermi level (E_{F}). Reprinted with permission from *Nano Lett.* 2023, 23, 14, 6698–6704 [157]. Copyright 2023 American Chemical Society.

ferrimagnetic phase transition in these heterojunctions, where the net magnetic moments can be spatially modulated through the sign of the excess charge. To conclude, these findings unveil novel and highly tunable functionalities in zigzag graphene nanoribbon/hexagonal boron nitride heterojunctions emerging from an intriguing interplay between charge and spin degrees of freedom, with potential implications for integrated carbon-based spintronic devices where completely spin-polarized electrical currents are desirable.

Chapter 6

Möbius graphene nanostrips for chiral nanophotonics

Chiral nanostructures are characterised by their lack of mirror symmetry and the ensuing differential response to left- and right-circularly polarised radiation. The advancement of optical technology demands the development of chiral nanostructures in which such dissymmetry of optical response is designed to be as strong as possible. In this Chapter, I comprehensively analyse the chiral optical properties of circular twisted graphene nanostrips, with a particular emphasis on the case of a Möbius graphene nanostrip. I use the method of coordinate transformation to analytically model the electronic structure and optical spectra of the nanostrips, while employing the cyclic boundary conditions to account for their topology. It is found that the dissymmetry factors of twisted graphene nanostrips can reach 0.01, exceeding the typical dissymmetry factors of small chiral molecules by one to two orders of magnitude. The results of this work thus demonstrate that twisted graphene nanostrips of Möbius and similar geometries are highly promising nanostructures for chiral optical applications.

This Chapter draws heavily upon a research paper co-authored by me and published in *The Journal of Physical Chemistry Letters*:

> M. E. Razzhivina, I. D. Rukhlenko, **N. V. Tepliakov**. Chiral Optical Properties of Möbius Graphene Nanostrips. *J. Phys. Chem. Lett.* **14**(19), 4426–4432 (2023). [Online]

Substantial portions of text included in this chapter were written collaboratively by all contributing authors. I contributed to the work by conceiving the original idea, supervising a student through the entire process of calculations and preparing figures, and managing the writing process.

6.1 Electronic properties of Möbius graphene nanostrips

6.1.1 Coordinate transformation method

Consider a plane graphene nanoribbon of length L, made of atoms arranged in the armchair configuration, and denote the maximum number of atoms across the nanoribbon's width as n. Figure 6.1(a) shows a plane nanoribbon with $n = 5$ and the orientation of the Cartesian axes (x, y, z) associated with its surface. A twisted circular nanostrip is obtained by twisting a plane nanoribbon m times along its x-axis, so that the opposite ends of the nanoribbon are rotated by $m\pi$ with respect to each other, and connecting these ends to form a loop. Without loss of generality, we focus on three types of twisted nanoribbons shown in Fig. 6.1(b): an achiral circular nanostrip with $m = 0$, that possesses mirror symmetry, a chiral Möbius nanostrip with $m = 1$, and a doubly twisted nanostrip with $m = 2$. Such graphene nanostrips have recently been fabricated by Segawa et al. [98], who also discovered a relatively strong optical activity in these chiral nanostructures. This experimental breakthrough emphasises the growing need for a comprehensive theoretical framework describing the optical response of such nanostrips.

The Cartesian coordinates (X, Y, Z) of atoms in a twisted circular nanostrip are expressed through the Cartesian coordinates (x, y, z) of atoms in the plane nanoribbon as

$$X = \left[\rho + z\cos\left(\frac{mx}{2\rho}\right) + y\chi\sin\left(\frac{mx}{2\rho}\right)\right]\cos(x/\rho), \tag{6.1}$$

$$Y = \left[\rho + z\cos\left(\frac{mx}{2\rho}\right) + y\chi\sin\left(\frac{mx}{2\rho}\right)\right]\sin(x/\rho), \tag{6.2}$$

$$Z = y\cos\left(\frac{mx}{2\rho}\right) - z\chi\sin\left(\frac{mx}{2\rho}\right), \tag{6.3}$$

where $\rho = L/(2\pi)$ is the radius of the circular nanostrip and $\chi = \pm 1$ distinguishes between the twist directions.

The interaction of a twisted nanostrip with light can be conveniently described using the local coordinates (x, y, z), in which the nanostrip is plane and has simple electronic structure,

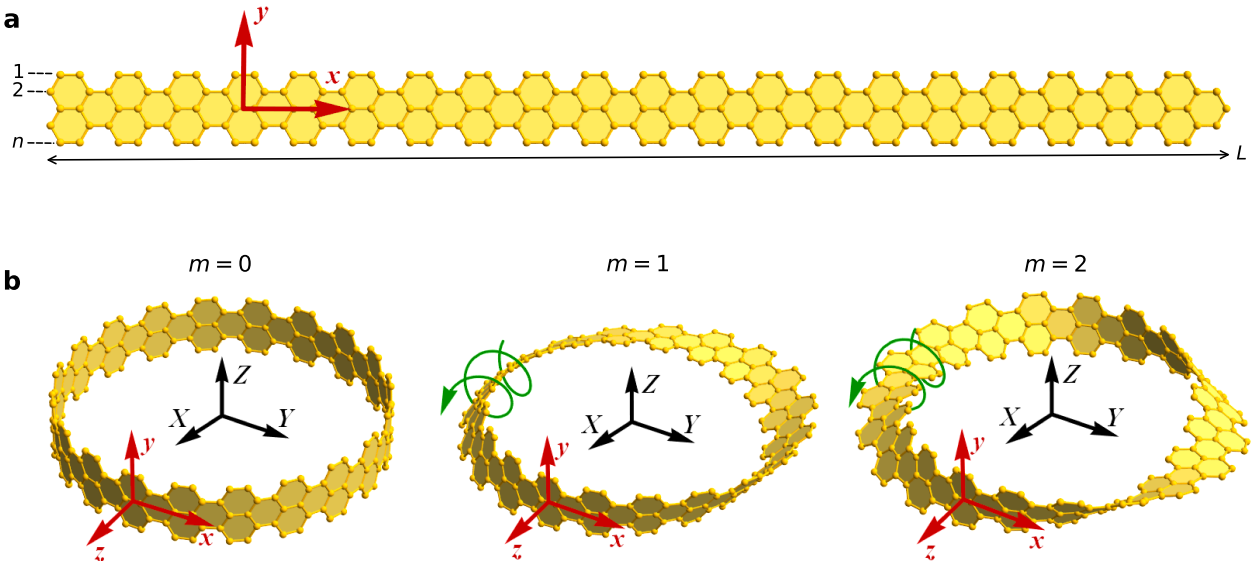


Figure 6.1: (a) Plane graphene nanoribbon of length L and with n atoms across the width and (b) circular graphene nanostrips obtained by twisting the nanoribbon m times around its x axis and connecting the opposite ends. The green spiral arrows indicate the direction of twist in the displayed enantiomers with $\chi = 1$. The nanostrips are a plane nanoribbon in the local curvilinear coordinates (x, y, z), and the origin of Cartesian coordinates (X, Y, Z) is at the center of the circular nanostrip. In all cases, $n = 5$ and $L = 85$ nm. Reprinted with permission from *J. Phys. Chem. Lett.* 2023, 14, 19, 4426–4432 [176]. Copyright 2023 American Chemical Society.

yet the light–matter interaction is modified by the inverse coordinate transformation

$$x = \rho\Phi, \tag{6.4}$$

$$y = Z\cos\left(\frac{m\Phi}{2}\right) + \chi(R-\rho)\sin\left(\frac{m\Phi}{2}\right), \tag{6.5}$$

$$z = -\chi Z\sin\left(\frac{m\Phi}{2}\right) + (R-\rho)\cos\left(\frac{m\Phi}{2}\right), \tag{6.6}$$

where $R = \sqrt{X^2+Y^2}$ and $\Phi = \arctan(Y/X)$.

We then solve the standard tight-binding Hamiltonian of a graphene nanoribbon (see, for example, Eq. (3.1) in Chapter 3) and find the wave functions $\psi_{\mu k}(\mathbf{r})$ and energies $E_{\mu k}$ of the p_z electrons, where μ labels energy bands, and k is the electron wavenumber in the x-direction. The wave functions of electrons are defined in the local curvilinear coordinates $\mathbf{r} = (x, y, z)$ on the surface of the nanostrip. These wave functions are the Bloch waves of the form

$$\psi_{\mu k}(\mathbf{r}) = \frac{e^{ikx}}{\sqrt{L}}\, u_{\mu k}(\mathbf{r}), \tag{6.7}$$

where $u_{\mu k}(\mathbf{r})$ is the periodic Bloch amplitude. The wavenumber k determines the local velocity of the electrons on the surface of the nanostrip, as well as the projection of their angular momentum on the Cartesian Z-axis of the circular nanostrip as $\langle \mu k | L_Z | \mu k \rangle = \hbar \rho k$.

6.1.2 Topological properties of Möbius nanostrips

The quantization of the electron wavenumber k (and angular momentum L_Z, correspondingly) is determined by the continuity of the wave function at the connected ends of the nanoribbon. For even m, which describe the nanostrips of trivial topology, the cross-section of the nanostrip is oriented the same way at the two ends, as demonstrated in Figure 6.2(a). The corresponding boundary condition

$$\psi_{\mu k}(L/2, y, z) = \psi_{\mu k}(-L/2, y, z), \tag{6.8}$$

yields the trivial quantization rule

$$k = \frac{2\pi n_x}{L}, \tag{6.9}$$

or $L_Z = \hbar n_x$, where $n_x \in Z$. For odd m, corresponding to the nontrivial topology, the cross section of the nanostrip is rotated by $m\pi$ upon the twist, as shown in Figure 6.2(b), and the same boundary condition reads

$$\psi_{\mu k}(L/2, y, z) = \psi_{\mu k}(-L/2, -y, -z). \tag{6.10}$$

Note that the Bloch amplitudes are odd functions of z because they originate from the p_z-orbitals of carbon atoms, $u_{\mu k}(y, -z) = -u_{\mu k}(y, z)$. Therefore, the quantization rule following from Eq. (6.10) depends on the parity of the Bloch amplitude with respect to y. One can see in Figure 6.2(b) that when $u_{\mu k}$ is an odd function of y, the wave function is continuous at the connected ends of the nanostrip, $u_{\mu k}(-y, -z) = u_{\mu k}(y, z)$, and the electron wavenumber k is quantized according to Eq. (6.9). On the contrary, the wave function which is even with respect to y changes sign upon the rotation by $m\pi$, $u_{\mu k}(-y, -z) = -u_{\mu k}(y, z)$, and the quantization rule becomes

$$k = \frac{2\pi}{L}\left(n_x + \frac{1}{2}\right), \tag{6.11}$$

or $L_Z = \hbar(n_x + 1/2)$. We thus obtain that in Möbius graphene nanostrips, the Z-projection of angular momentum can assume semi-integer values of $\hbar$, contrary to the systems of trivial geometry.

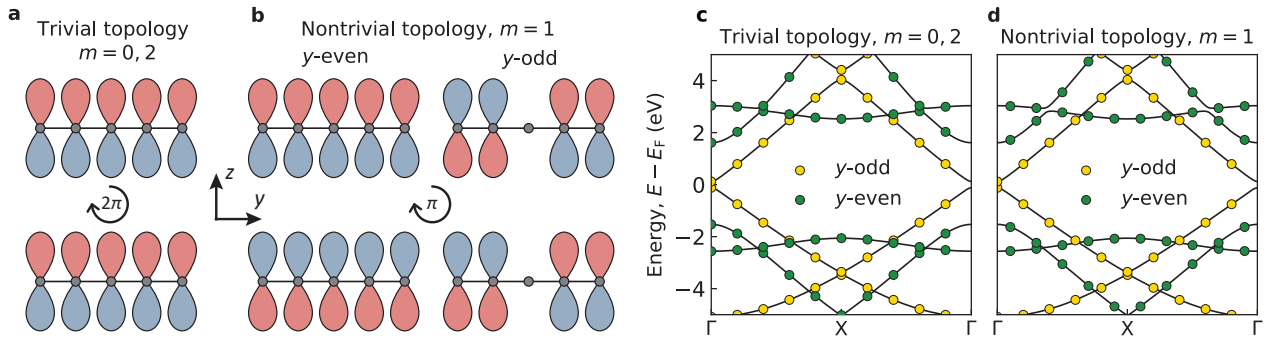


Figure 6.2: Rotation of the wave functions formed by p_z-orbitals of carbon atoms in the cross-section of a graphene nanoribbon with $n = 5$ upon the formation of a circular nanostrip with (a) trivial and (b) nontrivial topology. The cross section is rotated in the yz-plane either by 2π in the case of even number of twists ($m = 0, 2$) or by π in the case of odd number of twists ($m = 1$). Panel (b) shows states of different parities with respect to reflection $y \to -y$. Energy bands of circular graphene nanostrips with (c) even and (d) odd number of twists. Yellow and green circles correspond to the states that are odd and even with respect to y, respectively. Reprinted with permission from *J. Phys. Chem. Lett.* 2023, 14, 19, 4426–4432 [176]. Copyright 2023 American Chemical Society.

Figures 6.2(c) and (d) compare the band structures of circular nanostrips with even and odd numbers of twists. One sees that different quantization rules of the electron wavenumber for even and odd Bloch amplitudes in Möbius nanostrip shift the even energy states by π/L with respect to the odd states. This prevents vertical transitions between the bands of opposite parities, resulting in the red shift of the absorption spectrum noticeable for small L.

6.2 Optical properties of Möbius graphene nanostrips

6.2.1 Measures of optical activity

Optical properties of chiral nanostructures are conveniently quantified via the circular dichroism spectrum, $\mathrm{CD}\,(\hbar\omega)$, which is the difference of the absorption spectra for left- and right-circularly polarised light:

$$\mathrm{CD}(\hbar\omega) = A^{\mathrm{L}}(\hbar\omega) - A^{\mathrm{R}}(\hbar\omega). \tag{6.12}$$

Conventional linear absorption, $A(\hbar\omega)$, is found as the average of the absorption coefficients for two circular polarisations:

$$A(\hbar\omega) = \frac{A^{\mathrm{L}}(\hbar\omega) + A^{\mathrm{R}}(\hbar\omega)}{2}. \tag{6.13}$$

If the circular graphene nanostrips nanostrips are oriented randomly with respect to the incident radiation, their absorption and CD spectra are given by

$$A(\hbar\omega) = C\hbar\omega \sum_{k,k'} \sum_{\mu,\nu} D_{\mu k;\nu k'} f\left(\hbar\omega - E_{\mu k} + E_{\nu k'}\right), \tag{6.14}$$

$$\mathrm{CD}(\hbar\omega) = 2C\hbar\omega \sum_{k,k'} \sum_{\mu,\nu} R_{\mu k;\nu k'} f\left(\hbar\omega - E_{\mu k} + E_{\nu k'}\right), \tag{6.15}$$

where $C = 32\pi^3 N_c/\left(3\hbar c\right)$, N_c is the volumetric concentration of the nanostrips, the summation is performed over all occupied states $|\mu k\rangle$ and all unoccupied states $|\nu k'\rangle$, $D_{\mu k;\nu k'} = |\langle \mu k|\mathbf{d}|\nu k'\rangle|^2$ is the transition probability, $R_{\mu k;\nu k'} = \mathrm{Im}\langle \mu k|\mathbf{d}|\nu k'\rangle \cdot \langle \nu k'|\mathbf{m}|\mu k\rangle$ is the rotatory strength of the transition [177, 178], $\mathbf{d}$ and $\mathbf{m}$ are the electric and magnetic dipole moment operators, and $f(\hbar\omega)$ is the spectral lineshape function.

Since the absorption and CD spectra are proportional to the same scaling factor, it is more instructive to analyse the relative strength of the optical activity, which is conveniently characterised by the dissymmetry factor (or g-factor) spectrum:

$$g(\hbar\omega) = 2\frac{\mathrm{CD}(\hbar\omega)}{A(\hbar\omega)} \tag{6.16}$$

According to this definition, the maximum values of the g-factor are ± 2, corresponding to the two scenarios in which the system totally transmits one or the other circular polarisation of light. While these scenarios are highly desirable for the optical applications of chiral nanomaterials, realistic g-factors of small chiral molecules and semiconductor nanocrystals range between $\pm(10^{-3}$–$10^{-2})$ [77, 88, 89, 179, 180].

6.2.2 Transition matrix elements

In order to calculate the absorption probabilities $D_{\mu k;\nu k'}$ and rotatory strengths $R_{\mu k;\nu k'}$ of transitions in the circular graphene nanostrips, we express the matrix elements of the dipole moments through the coordinate and momentum operators in the original Cartesian coordinates, $\mathbf{R} = (X, Y, Z)$ and $\mathbf{P} = -i\hbar(\partial_X, \partial_Y, \partial_Z)$, as

$$\langle \mu k|\mathbf{d}|\nu k'\rangle = \frac{ie}{m_e\omega}\langle \mu k|\mathbf{P}|\nu k'\rangle, \tag{6.17}$$

$$\langle \nu k'|\mathbf{m}|\mu k\rangle = \frac{e}{m_e c}\langle \nu k'|\mathbf{R}\times\mathbf{P}|\mu k\rangle. \tag{6.18}$$

Note that we do not include the topological contribution to the magnetic moment in Eq. (6.18). Such contribution is relevant for the Möbius graphene nanostrips with zigzag edges, whose bandstructures are spin-polarised [102, 181], but not for armchair graphene nanostrips analysed in this study. On the other hand, armchair-edge Möbius nanostrips made of materials other than graphene may potentially feature topologically protected states due to non-negligible spin-orbit coupling [99].

In order to calculate the matrix elements of the electric and magnetic dipole moments, we convert the momentum operator $\mathbf{P} = P_X\mathbf{e}_X + P_Y\mathbf{e}_Y + P_Z\mathbf{e}_Z$ in the original Cartesian coordinates (X, Y, Z) into the local curvilinear coordinates (x, y, z) of the nanostrip as

$$P_X = \frac{\partial x}{\partial X}p_x + \frac{\partial y}{\partial X}p_y + \frac{\partial z}{\partial X}p_z, \tag{6.19}$$

$$P_Y = \frac{\partial x}{\partial Y}p_x + \frac{\partial y}{\partial Y}p_y + \frac{\partial z}{\partial Y}p_z, \tag{6.20}$$

$$P_Z = \frac{\partial x}{\partial Z}p_x + \frac{\partial y}{\partial Z}p_y + \frac{\partial z}{\partial Z}p_z. \tag{6.21}$$

The result is given by

$$P_X = -\sin\left(\frac{x}{\rho}\right)p_x + \chi\cos\left(\frac{x}{\rho}\right)\sin\left(\frac{mx}{2\rho}\right)p_y, \tag{6.22}$$

$$P_Y = \cos\left(\frac{x}{\rho}\right)p_x + \chi\sin\left(\frac{x}{\rho}\right)\sin\left(\frac{mx}{2\rho}\right)p_y, \tag{6.23}$$

$$P_Z = \cos\left(\frac{mx}{2\rho}\right)p_y, \tag{6.24}$$

where it was taken into account that the width of the nanoribbon is much smaller than its radius, $|y| \ll \rho$, and that the nanoribbon is locally flat, so that $z = 0$ and $p_z = 0$.

Similarly, the angular momentum in the original coordinates, $\mathbf{L} = \mathbf{R} \times \mathbf{P}$, is expressed through the curvilinear coordinates as

$$L_X = p_y\rho\cos\left(\frac{mx}{2\rho}\right)\sin\left(\frac{x}{\rho}\right), \tag{6.25}$$

$$L_Y = -p_y\rho\cos\left(\frac{mx}{2\rho}\right)\cos\left(\frac{x}{\rho}\right), \tag{6.26}$$

$$L_Z = \rho p_x. \tag{6.27}$$

We next need to calculate the interband matrix elements of operators which have the forms $f(x)p_x$ and $f(x)p_y$. Following the standard approach of $\mathbf{k}\cdot\mathbf{p}$-perturbation theory, we calculate the matrix elements of the momentum operators p_x and p_y using the periodic Bloch

amplitudes $u_{\mu k}$ and $u_{\nu k'}$ and evaluate the matrix element of the slowly varying functions $f(x)$ by integrating them over the exponential envelopes e^{ikx}. The resulting matrix elements of the momentum operator are given by

$$\langle \mu k|P_X|\nu k'\rangle = -\frac{i}{2}\langle \mu k|p_x|\nu k'\rangle \left(\delta_{k',k+\frac{2\pi}{L}} - \delta_{k',k-\frac{2\pi}{L}}\right) + \frac{i\chi\langle \mu k|p_y|\nu k'\rangle}{4}\left(\delta_{k',k+\frac{(m+2)\pi}{L}} + \delta_{k',k+\frac{(m-2)\pi}{L}} - \delta_{k',k-\frac{(m-2)\pi}{L}} - \delta_{k',k-\frac{(m+2)\pi}{L}}\right), \quad (6.28)$$

$$\langle \mu k|P_Y|\nu k'\rangle = \frac{\langle \mu k|p_x|\nu k'\rangle}{2}\left(\delta_{k',k+\frac{2\pi}{L}} + \delta_{k',k-\frac{2\pi}{L}}\right) - \frac{\chi\langle \mu k|p_y|\nu k'\rangle}{4}\left(\delta_{k',k+\frac{(m+2)\pi}{L}} - \delta_{k',k+\frac{(m-2)\pi}{L}} - \delta_{k',k-\frac{(m-2)\pi}{L}} + \delta_{k',k-\frac{(m+2)\pi}{L}}\right), \quad (6.29)$$

$$\langle \mu k|P_Z|\nu k'\rangle = \frac{\langle \mu k|p_y|\nu k'\rangle}{2}\left(\delta_{k',k+\frac{m\pi}{L}} + \delta_{k',k-\frac{m\pi}{L}}\right). \quad (6.30)$$

Similarly, the matrix elements of the angular momentum are given by

$$\langle \nu k'|L_X|\mu k\rangle = \frac{\rho\langle \nu k'|p_y|\mu k\rangle}{4i}\left(\delta_{k',k+\frac{(m+2)\pi}{L}} - \delta_{k',k+\frac{(m-2)\pi}{L}} + \delta_{k',k-\frac{(m-2)\pi}{L}} - \delta_{k',k-\frac{(m+2)\pi}{L}}\right), \quad (6.31)$$

$$\langle \nu k'|L_Y|\mu k\rangle = -\frac{\rho\langle \nu k'|p_y|\mu k\rangle}{4}\left(\delta_{k',k+\frac{(m+2)\pi}{L}} + \delta_{k',k+\frac{(m-2)\pi}{L}} + \delta_{k',k-\frac{(m-2)\pi}{L}} + \delta_{k',k-\frac{(m+2)\pi}{L}}\right), \quad (6.32)$$

$$\langle \nu k'|L_Z|\mu k\rangle = \rho\langle \nu k'|p_x|\mu k\rangle\delta_{k',k}. \quad (6.33)$$

The absorption probability and intensity of the CD signal are given by

$$|\langle \mu k|\mathbf{P}|\nu k'\rangle|^2 = \frac{|\langle \mu k|p_x|\nu k'\rangle|^2}{2}\left(\delta_{k',k+\frac{2\pi}{L}} + \delta_{k',k-\frac{2\pi}{L}}\right) + \frac{|\langle \mu k|p_y|\nu k'\rangle|^2}{8} \times \left(\delta_{k',k+\frac{(m+2)\pi}{L}} + \delta_{k',k+\frac{(m-2)\pi}{L}} + \delta_{k',k-\frac{(m-2)\pi}{L}} + \delta_{k',k-\frac{(m+2)\pi}{L}} + 2\delta_{k',k+\frac{m\pi}{L}} + 2\delta_{k',k-\frac{m\pi}{L}}\right), \quad (6.34)$$

$$\langle \mu k|\mathbf{P}|\nu k'\rangle\langle \nu k'|\mathbf{L}|\mu k\rangle = \chi\frac{\rho|\langle \mu k|p_y|\nu k'\rangle|^2}{8} \times \left(\delta_{k',k+\frac{(m+2)\pi}{L}} - \delta_{k',k+\frac{(m-2)\pi}{L}} - \delta_{k',k-\frac{(m-2)\pi}{L}} + \delta_{k',k-\frac{(m+2)\pi}{L}}\right). \quad (6.35)$$

Specifically, for $m = 0$

$$|\langle \mu k|\mathbf{P}|\nu k'\rangle|^2 = \frac{|\langle \mu k|p_x|\nu k'\rangle|^2}{2}\left(\delta_{k',k+\frac{2\pi}{L}} + \delta_{k',k-\frac{2\pi}{L}}\right) + \frac{|\langle \mu k|p_y|\nu k'\rangle|^2}{4}\left(\delta_{k',k+\frac{2\pi}{L}} + 2\delta_{k',k} + \delta_{k',k-\frac{2\pi}{L}}\right), \quad (6.36)$$

$$\langle \mu k|\mathbf{P}|\nu k'\rangle\langle \nu k'|\mathbf{L}|\mu k\rangle = 0. \quad (6.37)$$

For $m = 1$

$$|\langle \mu k|\mathbf{P}|\nu k'\rangle|^2 = \frac{|\langle \mu k|p_x|\nu k'\rangle|^2}{2}\left(\delta_{k',k+\frac{2\pi}{L}} + \delta_{k',k-\frac{2\pi}{L}}\right) + \frac{|\langle \mu k|p_y|\nu k'\rangle|^2}{8}\left(\delta_{k',k+\frac{3\pi}{L}} + 3\delta_{k',k+\frac{\pi}{L}} + 3\delta_{k',k-\frac{\pi}{L}} + \delta_{k',k-\frac{3\pi}{L}}\right), \quad (6.38)$$

$$\langle \mu k|\mathbf{P}|\nu k'\rangle\langle \nu k'|\mathbf{L}|\mu k\rangle = \chi\frac{\rho|\langle \mu k|p_y|\nu k'\rangle|^2}{8}\left(\delta_{k',k+\frac{3\pi}{L}} - \delta_{k',k+\frac{\pi}{L}} - \delta_{k',k-\frac{\pi}{L}} + \delta_{k',k-\frac{3\pi}{L}}\right). \quad (6.39)$$

Finally, for $m = 2$

$$|\langle \mu k|\mathbf{P}|\nu k'\rangle|^2 = \frac{|\langle \mu k|p_x|\nu k'\rangle|^2}{2}\left(\delta_{k',k+\frac{2\pi}{L}} + \delta_{k',k-\frac{2\pi}{L}}\right) + \frac{|\langle \mu k|p_y|\nu k'\rangle|^2}{8}\left(\delta_{k',k+\frac{4\pi}{L}} + 2\delta_{k',k+\frac{2\pi}{L}} + 2\delta_{k',k} + 2\delta_{k',k-\frac{2\pi}{L}} + \delta_{k',k-\frac{4\pi}{L}}\right), \quad (6.40)$$

$$\langle \mu k|\mathbf{P}|\nu k'\rangle\langle \nu k'|\mathbf{L}|\mu k\rangle = \chi\frac{\rho|\langle \mu k|p_y|\nu k'\rangle|^2}{8}\left(\delta_{k',k+\frac{4\pi}{L}} - 2\delta_{k',k} + \delta_{k',k-\frac{4\pi}{L}}\right). \quad (6.41)$$

The momentum matrix elements calculated using Bloch amplitudes, $\langle \nu k'|\mathbf{p}|\mu k\rangle$, are obtained from the matrix representation of the tight-binding Hamiltonian, H. First, the momentum operator is calculated in the basis of sublattices as

$$\mathbf{p} = \frac{m_\mathrm{e}}{\hbar}\frac{\partial H}{\partial \mathbf{k}}. \quad (6.42)$$

Then the interband matrix elements of the momentum operator are calculated as

$$\langle \nu k'|\mathbf{p}|\mu k\rangle = \sum_{i,j} c^*_{\nu k' i} p_{ij} c_{\mu k j} \quad (6.43)$$

where $c_{\mu k j}$ is the jth component of the eigenvector corresponding to state $|\mu k\rangle$.

In a more accessible form, the absorption intensities and rotatory strengths of the transitions are presented in Table 6.1. It is seen that the selection rules of interband transitions (i.e., the allowed values of $\Delta k = k' - k$) in circular graphene nanostrips vary significantly depending on the number of the nanoribbon's twists m. Absorption of light by circular nanostrips with $m = 0$ occurs via vertical transitions with $\Delta k = 0$ ($\Delta L_Z = 0$) and diagonal transitions with $\Delta k = \pm 2\pi/L$ ($\Delta L_Z = \pm\hbar$). Möbius nanostrips with $m = 1$ absorb via six diagonal transitions accompanied by the transfer of momentum $\Delta k = \pm\pi/L$, $\pm 2\pi/L$, and $\pm 3\pi/L$, corresponding to $\Delta L_Z = \pm\hbar/2$, $\pm\hbar$, and $\pm 3\hbar/2$. Finally, doubly twisted nanostrips with $m = 2$ absorb via vertical transitions with $\Delta k = 0$ ($\Delta L_Z = 0$) and diagonal transitions with $\Delta k = \pm 2\pi/L$ ($\Delta L_Z = \pm\hbar$) and $\pm 4\pi/L$ ($\Delta L_Z = \pm 2\hbar$).

$k'-k$	$m=0$		$m=1$		$m=2$	
	$D_{\mu k;\nu k'}$	$R_{\mu k;\nu k'}$	$D_{\mu k;\nu k'}$	$R_{\mu k;\nu k'}$	$D_{\mu k;\nu k'}$	$R_{\mu k;\nu k'}$
0	$\lvert\mathcal{P}_y\rvert^2/2$	0	—	—	$\lvert\mathcal{P}_y\rvert^2/4$	$-\chi\rho\lvert\mathcal{P}_y\rvert^2/4$
$\pm\pi/L$	—	—	$3\lvert\mathcal{P}_y\rvert^2/8$	$-\chi\rho\lvert\mathcal{P}_y\rvert^2/8$	—	—
$\pm2\pi/L$	$\lvert\mathcal{P}_x\rvert^2/2+\lvert\mathcal{P}_y\rvert^2/4$	0	$\lvert\mathcal{P}_x\rvert^2/2$	0	$\lvert\mathcal{P}_x\rvert^2/2+\lvert\mathcal{P}_y\rvert^2/4$	0
$\pm3\pi/L$	—	—	$\lvert\mathcal{P}_y\rvert^2/8$	$\chi\rho\lvert\mathcal{P}_y\rvert^2/8$	—	—
$\pm4\pi/L$	—	—	—	—	$\lvert\mathcal{P}_y\rvert^2/8$	$\chi\rho\lvert\mathcal{P}_y\rvert^2/8$

Table 6.1: Parameters $D_{\mu k;\nu k'}$ and $R_{\mu k;\nu k'}$ for circular graphene nanostrips with $m=0,1,2$; $\mathcal{P}_\xi=\langle\mu k|p_\xi|\nu k'\rangle$ $(\xi=x,y)$ is the momentum matrix element calculated using the Bloch states of the nanoribbon; $D_{\mu k;\nu k'}$ is in units $e^2/(m_\mathrm{e}\omega)^2$ and $R_{\mu k;\nu k'}$ is in units $e^2/(m_\mathrm{e}^2\omega c)$. Reprinted with permission from *J. Phys. Chem. Lett.* 2023, 14, 19, 4426–4432 [176]. Copyright 2023 American Chemical Society.

Naturally, the rotatory strengths of optical transitions are vanishing in the case of achiral graphene nanostrips with $m=0$. For the chiral nanostrips with $m=1,2$, the rotatory strengths are proportional to the twist direction $\chi=\pm1$, meaning that the two mirror images of the nanostrip have the same magnitude and opposite sign of the CD signal. While absorption occurs upon both x- and y-polarised transitions, the optical activity is only observed for transitions which are polarised in the y-direction, because chirality of the nanostrip stems from its rotation in the cross-section, *i.e.*, the yz-plane in the local coordinates. This means that the CD signal is only produced by transitions between the bands of opposite parities with respect to reflection $y\to-y$.

6.2.3 Relative strength of optical activity

The relative strength of optical activity on an individual optical transition can be characterised by the transition g-factor [180], which is given by $g_{\mu k;\nu k'}=4R_{\mu k;\nu k'}/D_{\mu k;\nu k'}$. The data in Table 6.1 shows that the dissymmetry factors of optically active transitions in circular graphene nanostrips scale linearly with the nanostrip's radius ρ as $g_{\mu k;\nu k'}\propto\pm q\rho$, where $q=\omega/c$ is the wavenumber of light. In theory, this means that the values of the dissymmetry factor spectrum $g(\hbar\omega)$ increase with the nanostrip's radius as well. However, the intensities of the CD peaks and the peaks in the g-factor spectrum are limited by the finite widths of the

absorption peaks.

For example, the CD signal of Möbius nanostrips is generated by four transitions with selection rules $\Delta k = \pm\pi/L$ and $\Delta k = \pm 3\pi/L$ (see Table 6.1 for $m = 1$). The respective pairs of the transitions have rotatory strengths that are equal in magnitude and opposite in sign. The energy separation of these pairs of transitions is relatively small, so that their corresponding absorption and CD peaks partially overlap in the spectrum. The partial overlap of the adjacent absorption peaks yields the following maximal value of the CD signal: $\max[g(\hbar\omega)] \sim \pm q\rho(\pi/L)^2(\partial E_{\nu k}/\partial k)^2/\gamma^2$, where 2γ is the full width at half maximum (FWHM) of the peak. In graphene nanostructures $\partial E_{\nu k}/\partial k \sim \hbar v_{\mathrm{F}}$, where v_{F} is the Fermi velocity, so that we finally get an estimate

$$\max[g(\hbar\omega)] \sim \pm(q/\rho)(\hbar v_{\mathrm{F}}/2\gamma)^2, \tag{6.44}$$

where we also took into account that $L = 2\pi\rho$. Hence, while the strengths of individual optically active transitions grow linearly with the nanostrip's size due to the linear growth of the dipole moment of the structure, the relative CD signal weakens as $\propto 1/\rho$ due to the increasing overlap of the absorption peaks. We cannot, however, assess the g-factors of chiral graphene nanostrips with very small ρ, since the coordinate transformation method used in this study requires the width of the nanostrip to be much smaller than its radius, $|y| \ll \rho$.

6.2.4 Optical spectra

Absorption spectra of Möbius $(m = 1)$ and doubly twisted $(m = 2)$ nanostrips with $n = 5$ and $L = 85$ nm are shown in Fig. 6.3(a). Owing to the large length and the resulting quasi-continuity of the energy spectra of the nanostrips, the difference between their absorption spectra is negligible and not reflected in the figure. The absorption is contributed by transitions polarised either along or perpendicular to the nanoribbon's length. These contributions are shown by the yellow and green areas in the figure. One sees that the x-polarised transitions occur over the entire spectrum, whereas the y-polarised transitions occur only in the visible range and above. The absence of the y-polarised transitions in the infrared range is due to the fact that the two energy bands near the Fermi level have the same parities with respect to reflection $y \to -y$ (see the band structure in Fig. 6.2).

The CD spectra of the nanostrips are plotted in Fig. 6.3(b). Unlike absorption, the CD

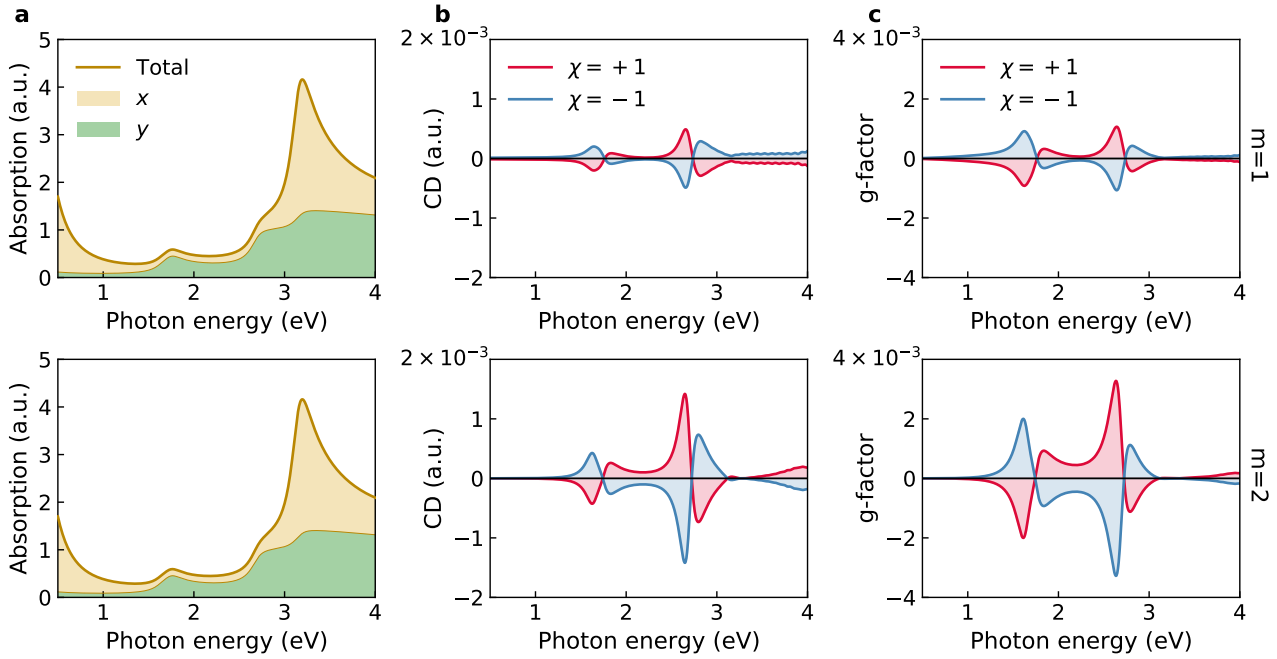


Figure 6.3: (a) Absorption, (b) CD, and (c) g-factor spectra of chiral graphene nanostrips with $m = 1, 2$, $n = 5$ atoms across the nanoribbon, and a length of $L = 85$ nm. The yellow and green areas under the absorption spectrum show relative contributions from the x- and y-polarised transitions; the colors of the CD spectra differentiate between the two enantiomers of the nanostrips ($\chi = \pm 1$). Reprinted with permission from *J. Phys. Chem. Lett.* 2023, 14, 19, 4426–4432 [176]. Copyright 2023 American Chemical Society.

signal is seen to strongly depend on the number of twists. Note that the infrared CD signal is absent because only the y-polarised transitions in the nanostrips are optically active. The CD of the doubly twisted nanostrip is several times stronger than the CD of the Möbius nanostrip of the same size. Since the nanostrips absorb equally, this implies that the doubly twisted nanostrips exhibit larger dissymmetry of optical response and are thus more appealing for chiroptical applications. This is confirmed by the g-factor spectra of the chiral graphene nanostrips in Fig. 6.3(c).

Figure 6.4 further illustrates the dependence of the g-factor spectrum on the parameters of chiral graphene nanostrips. Only nanoribbons with odd n, capable to form closed Möbius nanostrips, are considered. Such nanoribbons possess mirror symmetry with respect to reflection $y \to -y$, necessary to satisfy the boundary conditions $\psi(L/2, y, z) = \psi(-L/2, -y, -z)$ at the connected ends of the nanostrip composed of an integer number of unit cells. The density plots in Figure 6.4 show the preferential absorption of left-circularly polarised light by red and

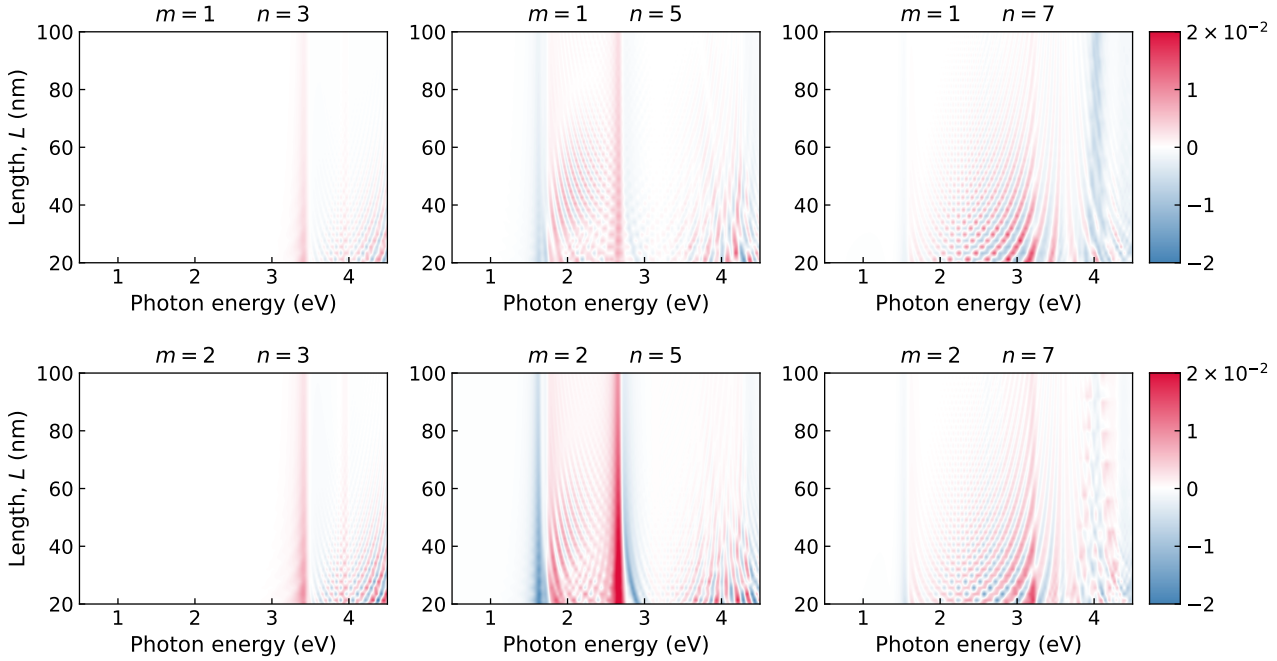


Figure 6.4: Dissymmetry factor spectra of chiral graphene nanostrips *vs* nanoribbon length L for $m = 1, 2$, $n = 3, 5, 7$, and $\chi = 1$. Reprinted with permission from *J. Phys. Chem. Lett.* 2023, 14, 19, 4426–4432 [176]. Copyright 2023 American Chemical Society.

right-circularly polarised light by blue. One sees that $g(\hbar\omega)$ can reach 10^{-2}, which is close to the experimental value for Möbius graphene nanobelts [98] and exceeds the typical values for small chiral molecules and quantum dots by one to two orders of magnitude [88, 182, 183]. Chiral molecular cylinders, morphologically similar to circular graphene nanostrips, can feature even larger dissymmetry factors of the order of 10^{-1}, though these values are highly sensitive to structural fluctuations [184]. In agreement with the above theoretical prediction, $g(\hbar\omega)$ in Figure 6.4 decreases like $\propto 1/L$. This suggests that smaller graphene nanoribbons are better for chiroptical applications. Confirming this, Möbius graphene nanobelts with unusually large dissymmetry factors, fabricated by Segawa et al., were indeed characterised by the radius of only a few nanometers [98].

The two narrower graphene nanostrips with $n = 3$ and $n = 5$ feature pronounced CD peaks, the spectral positions of which do not change with the length of the nanostrip. For $n = 3$ there is a strong signal at 3.4 eV and a weaker signal of the same sign at 3.9 eV, whereas for $n = 5$ there are two equally pronounced peaks of different signs at 1.7 and 2.7 eV. The dissymmetry factors of the doubly twisted nanostrips are seen to be notably larger than those of the Möbius nanostrips of the same dimensions. The difference between $m = 1$ and $m = 2$

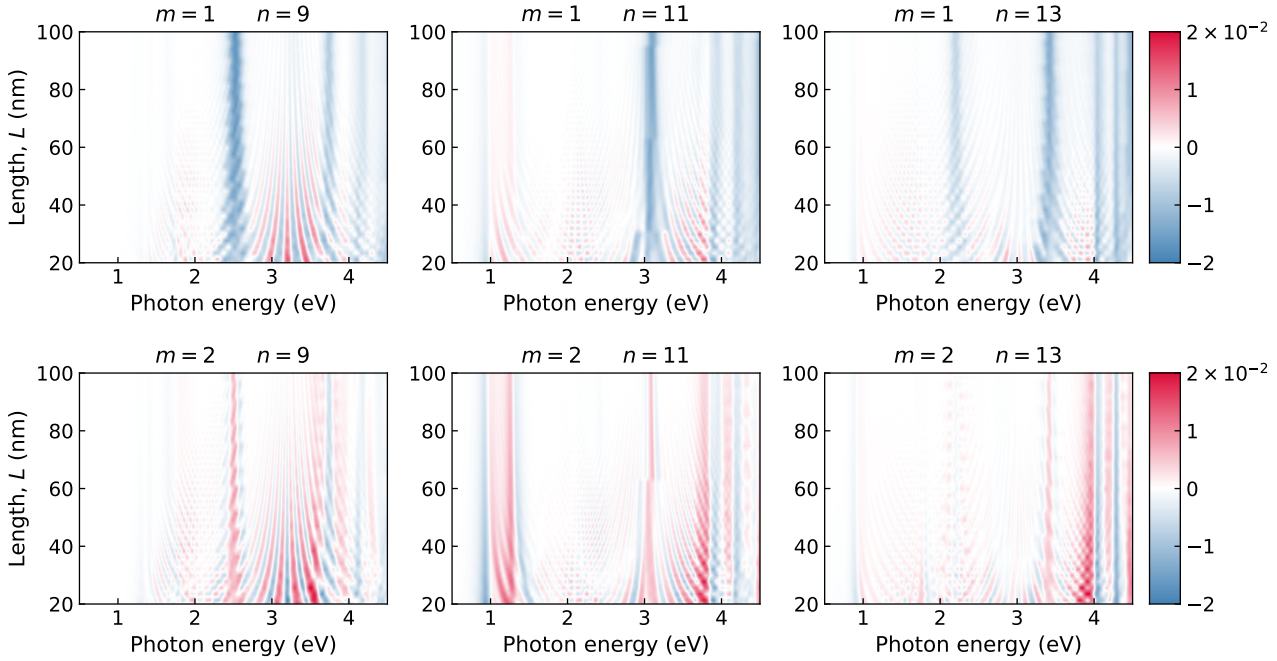


Figure 6.5: Dissymmetry factor spectra of chiral graphene nanostrips *vs* nanoribbon length L for $m = 1, 2$, $n = 9, 11, 13$, and $\chi = 1$. Reprinted with permission from *J. Phys. Chem. Lett.* 2023, 14, 19, 4426–4432 [176]. Copyright 2023 American Chemical Society.

is the least prominent for the widest nanoribbons with $n = 7$, yet there is more interference in the optical spectra, with two weak peaks of opposite signs identifiable at 1.5 and 3.2 eV.

To investigate the effect of larger widths on chiral optical properties of graphene nanostrips, in Figure 6.5 we show the dissymmetry factors for $n = 9$, 11, and 13. This figure reveals similar trends in the optical spectra of wider graphene nanostrips, including relatively large g-factors of the order of 0.01. Overall, our results demonstrate that short twisted graphene nanostrips with $n = 5$ exhibit the strongest dissymmetry of optical response. This may be attributed to the fact that the armchair graphene nanoribbons with $n = 3p+2$ $(p = 1, 2, 3, \ldots)$ generally have richer electronic properties than other members of this family of carbon nanostructures [114].

In future studies, the analytical model developed in this work can be extended to include various additional atoms, such as oxygen, to provide more accurate modelling of circular graphene nanostrips synthesised from organic precursors. Our theoretical approach can also be employed to analyse Möbius graphene nanostrips with zigzag edges, whose nontrivial topological and magnetic properties can have significant implications for their chiral optical response. Finally, the coordinate transformation method can potentially describe Möbius

nanostrips made of other two-dimensional semiconductors, *e.g.*, transition metal dichalcogenides or hexagonal boron nitride, thus opening up new perspectives for studying the influence of nontrivial topology on different materials.

6.3 Conclusions

In this Chapter, I have modelled electronic and optical properties of Möbius graphene nanostrips and similar graphene nanostructures with a different number of twists. In order to describe the electronic properties of these graphene nanostrips, I developed a coordinate transformation that turns a twisted graphene nanostrip into a plane graphene nanoribbon residing in curvilinear space. Electronic properties of plane graphene nanoribbons are obtained using the tight-binding approximation for p_z-electrons. The nontrivial topology of the Möbius nanostrip is accounted for by the cyclic boundary conditions which distinguish between energy bands of different parities. The coordinate transformation transfers the chirality of the nanostrip to the curvature of the space, modifying the light-matter interaction operator. Further analytical calculations revealed that circular dichroism in twisted graphene nanostrips can only be observed in transitions polarised across the nanostrip, whereas absorption is formed by the transitions polarised both across and along the axis of the nanoribbon. We further analysed the dependence of the dissymmetry factor on the length and width of the Möbius and doubly twisted nanostrips. Among the analysed structures, doubly twisted nanostrips of width $n = 5$ and smaller lengths were found to feature the strongest dissymmetry of optical response. Overall, the dissymmetry factors of small twisted graphene nanostrips can reach values $\sim$0.01, highlighting Möbius graphene nanostrips as highly promising nanostructures for applications in chiral nanophotonics.

Summary and Outlook

This thesis presents several significant findings on the electronic, magnetic, and optical properties of graphene nanoribbons. Chapter 3 uncovers a previously unknown hidden symmetry governing the electronic properties of certain armchair graphene nanoribbons; this hidden symmetry can be controlled through mechanical strain, altering the nanoribbon's topological invariant. Chapter 4 demonstrates that applying a strong external electric field can trigger a semiconductor-to-semimetal transition in armchair graphene nanoribbons by polarising and decoupling their edges. Chapter 5 investigates the electronic and magnetic properties of zigzag graphene nanoribbons embedded in hexagonal boron nitride, revealing that these heterojunctions exhibit half-semimetallic behavior and can become ferrimagnetic under charge doping. Finally, Chapter 6 examines the optical activity of chiral graphene nanostrips with Möbius geometry, highlighting the significant dissymmetry in their optical absorption.

Looking forward, it is crucial to experimentally validate the key results of this dissertation, with particular emphasis on strain-induced topological phase transitions in armchair graphene nanoribbons and the electric-field-driven emergence of new electronic phases in both armchair and zigzag graphene nanoribbons. The capacity to engineer various electronic phases (semiconducting, semimetallic, half-semimetallic, metallic), magnetic orderings (antiferromagnetic, ferromagnetic, ferrimagnetic), and topological phases (trivial, non-trivial) within interconnected structures of graphene nanoribbons offers exceptional flexibility for the design of logic devices that leverage electron charge or spin for information processing. I hope that the findings outlined in this thesis will bring us closer to realising graphene-based nanostructures as a viable alternative to silicon in modern technologies, ultimately enabling high-performance, practical devices powered by graphene.

Bibliography

(1) Novoselov, K. S.; Geim, A. K.; Morozov, S. V.; Jiang, D.-e.; Zhang, Y.; Dubonos, S. V.; Grigorieva, I. V.; Firsov, A. A. *Science* **2004**, *306*, 666–669.

(2) Novoselov, K. S.; Geim, A. K.; Morozov, S. V.; Jiang, D.; Katsnelson, M. I.; Grigorieva, I. V.; Dubonos, S. V.; Firsov, A. A. *Nature* **2005**, *438*, 197–200.

(3) Wallace, P. R. *Physical Review* **1947**, *71*, 622.

(4) Reich, S.; Maultzsch, J.; Thomsen, C.; Ordejon, P. *Physical Review B* **2002**, *66*, 035412.

(5) Xia, F.; Farmer, D. B.; Lin, Y.-m.; Avouris, P. *Nano Letters* **2010**, *10*, 715–718.

(6) Giovannetti, G.; Khomyakov, P. A.; Brocks, G.; Kelly, P. J.; Van Den Brink, J. *Physical Review B* **2007**, *76*, 073103.

(7) Castro, E. V.; Novoselov, K.; Morozov, S.; Peres, N.; Dos Santos, J. L.; Nilsson, J.; Guinea, F.; Geim, A.; Neto, A. C. *Physical Review Letters* **2007**, *99*, 216802.

(8) Yano, Y.; Mitoma, N.; Ito, H.; Itami, K. *The Journal of Organic Chemistry* **2019**, *85*, 4–33.

(9) Fujita, M.; Wakabayashi, K.; Nakada, K.; Kusakabe, K. *Journal of the Physical Society of Japan* **1996**, *65*, 1920–1923.

(10) Nakada, K.; Fujita, M.; Dresselhaus, G.; Dresselhaus, M. S. *Physical Review B* **1996**, *54*, 17954.

(11) Brey, L.; Fertig, H. *Physical Review B* **2006**, *73*, 235411.

(12) Ezawa, M. *Physical Review B* **2006**, *73*, 045432.

(13) Yamashiro, A.; Shimoi, Y.; Harigaya, K.; Wakabayashi, K. *Physical Review B* **2003**, *68*, 193410.

(14) Son, Y.-W.; Cohen, M. L.; Louie, S. G. *Physical Review Letters* **2006**, *97*, 216803.

(15) Jung, J.; MacDonald, A. *Physical Review B* **2009**, *79*, 235433.

(16) Yazyev, O. V.; Katsnelson, M. *Physical Review Letters* **2008**, *100*, 047209.

(17) Cao, T.; Zhao, F.; Louie, S. G. *Physical Review Letters* **2017**, *119*, 076401.

(18) Gröning, O.; Wang, S.; Yao, X.; Pignedoli, C. A.; Borin Barin, G.; Daniels, C.; Cupo, A.; Meunier, V.; Feng, X.; Narita, A., et al. *Nature* **2018**, *560*, 209–213.

(19) Han, M. Y.; Özyilmaz, B.; Zhang, Y.; Kim, P. *Physical Review Letters* **2007**, *98*, 206805.

(20) Li, X.; Wang, X.; Zhang, L.; Lee, S.; Dai, H. *Science* **2008**, *319*, 1229–1232.

(21) Tapasztó, L.; Dobrik, G.; Lambin, P.; Biro, L. P. *Nature Nanotechnology* **2008**, *3*, 397–401.

(22) Wang, X.; Ouyang, Y.; Li, X.; Wang, H.; Guo, J.; Dai, H. *Physical Review Letters* **2008**, *100*, 206803.

(23) Kosynkin, D. V.; Higginbotham, A. L.; Sinitskii, A.; Lomeda, J. R.; Dimiev, A.; Price, B. K.; Tour, J. M. *Nature* **2009**, *458*, 872–876.

(24) Jiao, L.; Zhang, L.; Wang, X.; Diankov, G.; Dai, H. *Nature* **2009**, *458*, 877–880.

(25) Cai, J.; Ruffieux, P.; Jaafar, R.; Bieri, M.; Braun, T.; Blankenburg, S.; Muoth, M.; Seitsonen, A. P.; Saleh, M.; Feng, X.; Müllen, K.; Fasel, R. *Nature* **2010**, *466*, 470.

(26) Ruffieux, P.; Wang, S.; Yang, B.; Sánchez-Sánchez, C.; Liu, J.; Dienel, T.; Talirz, L.; Shinde, P.; Pignedoli, C. A.; Passerone, D.; Dumslaff, T.; Feng, X.; Müllen, K.; Fasel, R. *Nature* **2016**, *531*, 489.

(27) Ismach, A.; Druzgalski, C.; Penwell, S.; Schwartzberg, A.; Zheng, M.; Javey, A.; Bokor, J.; Zhang, Y. *Nano Letters* **2010**, *10*, 1542–1548.

(28) Campos-Delgado, J.; Romo-Herrera, J. M.; Jia, X.; Cullen, D. A.; Muramatsu, H.; Kim, Y. A.; Hayashi, T.; Ren, Z.; Smith, D. J.; Okuno, Y., et al. *Nano Letters* **2008**, *8*, 2773–2778.

(29) Mohamad Yunus, R.; Miyashita, M.; Tsuji, M.; Hibino, H.; Ago, H. *Chemistry of Materials* **2014**, *26*, 5215–5222.

(30) Chen, Z.; Zhang, W.; Palma, C.-A.; Lodi Rizzini, A.; Liu, B.; Abbas, A.; Richter, N.; Martini, L.; Wang, X.-Y.; Cavani, N., et al. *Journal of the American Chemical Society* **2016**, *138*, 15488–15496.

(31) Yu, Y.-J.; Zhao, Y.; Ryu, S.; Brus, L. E.; Kim, K. S.; Kim, P. *Nano Letters* **2009**, *9*, 3430–3434.

(32) Lukose, V.; Shankar, R.; Baskaran, G. *Physical Review Letters* **2007**, *98*, 116802.

(33) Tepliakov, N. V.; Leonov, M. Y.; Baranov, A. V.; Fedorov, A. V.; Rukhlenko, I. D. *Optics Express* **2016**, *24*, A52–A57.

(34) Son, Y.-W.; Cohen, M. L.; Louie, S. G. *Nature* **2006**, *444*, 347–349.

(35) Fang, C. M.; De Wijs, G.; De Groot, R. *Journal of Applied Physics* **2002**, *91*, 8340–8344.

(36) Žutić, I.; Fabian, J.; Sarma, S. D. *Reviews of Modern Physics* **2004**, *76*, 323.

(37) Raza, H.; Kan, E. C. *Physical Review B* **2008**, *77*, 245434.

(38) Zhao, F.; Cao, T.; Louie, S. G. *Physical Review Letters* **2021**, *127*, 166401.

(39) Saroka, V.; Batrakov, K.; Demin, V.; Chernozatonskii, L. *Journal of Physics: Condensed Matter* **2015**, *27*, 145305.

(40) Sahu, B.; Min, H.; MacDonald, A.; Banerjee, S. K. *Physical Review B* **2008**, *78*, 045404.

(41) Bala Kumar, S.; Guo, J. *Journal of Applied Physics* **2011**, *110*.

(42) Sahu, B.; Min, H.; Banerjee, S. K. *Physical Review B* **2010**, *82*, 115426.

(43) Huang, Y.; Chang, C.; Lin, M.-F. *Journal of Applied Physics* **2008**, *104*.

(44) Li, T. S.; Huang, Y. C.; Chang, S.; Chuang, Y.; Lin, M.-F. *The European Physical Journal B* **2008**, *64*, 73–80.

(45) Dean, C. R.; Young, A. F.; Meric, I.; Lee, C.; Wang, L.; Sorgenfrei, S.; Watanabe, K.; Taniguchi, T.; Kim, P.; Shepard, K. L., et al. *Nature Nanotechnology* **2010**, *5*, 722–726.

(46) Zhang, K.; Yap, F. L.; Li, K.; Ng, C. T.; Li, L. J.; Loh, K. P. *Advanced Functional Materials* **2014**, *24*, 731–738.

(47) Kawaguchi, M.; Kawashima, T.; Nakajima, T. *Chemistry of Materials* **1996**, *8*, 1197–1201.

(48) Ci, L.; Song, L.; Jin, C.; Jariwala, D.; Wu, D.; Li, Y.; Srivastava, A.; Wang, Z.; Storr, K.; Balicas, L., et al. *Nature Materials* **2010**, *9*, 430–435.

(49) Levendorf, M. P.; Kim, C.-J.; Brown, L.; Huang, P. Y.; Havener, R. W.; Muller, D. A.; Park, J. *Nature* **2012**, *488*, 627–632.

(50) Liu, Z.; Ma, L.; Shi, G.; Zhou, W.; Gong, Y.; Lei, S.; Yang, X.; Zhang, J.; Yu, J.; Hackenberg, K. P., et al. *Nature Nanotechnology* **2013**, *8*, 119–124.

(51) Sutter, P.; Cortes, R.; Lahiri, J.; Sutter, E. *Nano Letters* **2012**, *12*, 4869–4874.

(52) Gao, Y.; Zhang, Y.; Chen, P.; Li, Y.; Liu, M.; Gao, T.; Ma, D.; Chen, Y.; Cheng, Z.; Qiu, X., et al. *Nano Letters* **2013**, *13*, 3439–3443.

(53) Wang, H. S. et al. *Nature Materials* **2021**, *20*, 202.

(54) Chen, L. et al. *Nature Communications* **2017**, *8*, 14703.

(55) Ding, Y.; Wang, Y.; Ni, J. *Applied Physics Letters* **2009**, *95*, 123105.

(56) Pruneda, J. M. *Physical Review B* **2010**, *81*, 161409.

(57) Leon, C.; Costa, M.; Chico, L.; Latgé, A. *Scientific Reports* **2019**, *9*, 3508.

(58) Liu, Y.; Wu, X.; Zhao, Y.; Zeng, X. C.; Yang, J. *The Journal of Physical Chemistry C* **2011**, *115*, 9442.

(59) Zeng, J.; Chen, W.; Cui, P.; Zhang, D.-B.; Zhang, Z. *Physical Review B* **2016**, *94*, 235425.

(60) Kim, S.-W.; Kim, H.-J.; Choi, J.-H.; Scheicher, R. H.; Cho, J.-H. *Physical Review B* **2015**, *92*, 035443.

(61) Mak, K. F.; Sfeir, M. Y.; Wu, Y.; Lui, C. H.; Misewich, J. A.; Heinz, T. F. *Physical Review Letters* **2008**, *101*, 196405.

(62) Chang, C.-P.; Huang, Y.-C.; Lu, C.; Ho, J.-H.; Li, T.-S.; Lin, M.-F. *Carbon* **2006**, *44*, 508–515.

(63) Hsu, H.; Reichl, L. *Physical Review B* **2007**, *76*, 045418.

(64) Chung, H.; Lee, M.; Chang, C.; Lin, M. *Optics Express* **2011**, *19*, 23350–23363.

(65) Sasaki, K.-i.; Kato, K.; Tokura, Y.; Oguri, K.; Sogawa, T. *Physical Review B* **2011**, *84*, 085458.

(66) Barone, V.; Hod, O.; Scuseria, G. E. *Nano Letters* **2006**, *6*, 2748–2754.

(67) Yang, L.; Cohen, M. L.; Louie, S. G. *Nano Letters* **2007**, *7*, 3112–3115.

(68) Prezzi, D.; Varsano, D.; Ruini, A.; Marini, A.; Molinari, E. *Physical Review B* **2008**, *77*, 041404.

(69) Chernov, A. I.; Fedotov, P. V.; Talyzin, A. V.; Suarez Lopez, I.; Anoshkin, I. V.; Nasibulin, A. G.; Kauppinen, E. I.; Obraztsova, E. D. *ACS Nano* **2013**, *7*, 6346–6353.

(70) Lim, H. E.; Miyata, Y.; Fujihara, M.; Okada, S.; Liu, Z.; Arifin; Sato, K.; Omachi, H.; Kitaura, R.; Irle, S., et al. *ACS Nano* **2015**, *9*, 5034–5040.

(71) Denk, R.; Hohage, M.; Zeppenfeld, P.; Cai, J.; Pignedoli, C. A.; Söde, H.; Fasel, R.; Feng, X.; Müllen, K.; Wang, S., et al. *Nature Communications* **2014**, *5*, 4253.

(72) Senkovskiy, B.; Pfeiffer, M.; Alavi, S.; Bliesener, A.; Zhu, J.; Michel, S.; Fedorov, A.; German, R.; Hertel, D.; Haberer, D., et al. *Nano Letters* **2017**, *17*, 4029–4037.

(73) Alavi, S. K.; Senkovskiy, B. V.; Pfeiffer, M.; Haberer, D.; Fischer, F. R.; Grueneis, A.; Lindfors, K. *2D Materials* **2019**, *6*, 035009.

(74) Fedotov, P. V.; Rybkovskiy, D. V.; Chernov, A. I.; Obraztsova, E. A.; Obraztsova, E. D. *The Journal of Physical Chemistry C* **2020**, *124*, 25984–25991.

(75) Lindenthal, S.; Fazzi, D.; Zorn, N. F.; El Yumin, A. A.; Settele, S.; Weidinger, B.; Blasco, E.; Zaumseil, J. *ACS Nano* **2023**, *17*, 18240–18252.

(76) Tepliakov, N. V.; Kundelev, E. V.; Khavlyuk, P. D.; Xiong, Y.; Leonov, M. Y.; Zhu, W.; Baranov, A. V.; Fedorov, A. V.; Rogach, A. L.; Rukhlenko, I. D. *ACS Nano* **2019**, *13*, 10737–10744.

(77) Tanaka, H.; Inoue, Y.; Mori, T. *ChemPhotoChem* **2018**, *2*, 386–402.

(78) Konishi, K.; Nomura, M.; Kumagai, N.; Iwamoto, S.; Arakawa, Y.; Kuwata-Gonokami, M. *Phys. Rev. Lett.* **2011**, *106*, 057402.

(79) Han, D.; Li, C.; Jiang, C.; Jin, X.; Wang, X.; Chen, R.; Cheng, J.; Duan, P. *Aggregate* **2022**, *3*, e148.

(80) Tan, L.; Yu, S.-J.; Jin, Y.; Li, J.; Wang, P.-p. *Angew. Chem. Int. Ed.* **2022**, e202112400.

(81) Jiang, J.; Ouyang, G.; Zhang, L.; Liu, M. *Eur. J. Chem.* **2017**, *23*, 9439–9450.

(82) Aboul-Enein, H. Y.; Bounoua, N.; Rebizi, M.; Wagdy, H. *Chirality* **2021**, *33*, 196–208.

(83) Niu, X.; Yang, X.; Li, H.; Liu, J.; Liu, Z.; Wang, K. *Mikrochim. Acta* **2020**, *187*, 1–18.

(84) Yang, S.-H.; Naaman, R.; Paltiel, Y.; Parkin, S. S. *Nat. Rev. Phys.* **2021**, *3*, 328–343.

(85) Evers, F.; Aharony, A.; Bar-Gill, N.; Entin-Wohlman, O.; Hedegård, P.; Hod, O.; Jelinek, P.; Kamieniarz, G.; Lemeshko, M.; Michaeli, K., et al. *Advanced Materials* **2022**, *34*, 2106629.

(86) Fernández-García, J. M.; Evans, P. J.; Filippone, S.; Herranz, M. Á.; Martín, N. *Acc. Chem. Res.* **2019**, *52*, 1565–1574.

(87) Vázquez-Nakagawa, M.; Rodríguez-Pérez, L.; Herranz, M. Á.; Martín, N. *Chem. Comm.* **2016**, *52*, 665–668.

(88) Suzuki, N.; Wang, Y.; Elvati, P.; Qu, Z.-B.; Kim, K.; Jiang, S.; Baumeister, E.; Lee, J.; Yeom, B.; Bahng, J. H., et al. *ACS Nano* **2016**, *10*, 1744–1755.

(89) Tepliakov, N. V.; Orlov, A. V.; Kundelev, E. V.; Rukhlenko, I. D. *The Journal of Physical Chemistry C* **2020**, *124*, 22704–22710.

(90) Kim, C.-J.; Sánchez-Castillo, A.; Ziegler, Z.; Ogawa, Y.; Noguez, C.; Park, J. *Nature Nanotech.* **2016**, *11*, 520–524.

(91) Stauber, T.; Low, T.; Gómez-Santos, G. *Nano Lett.* **2020**, *20*, 8711–8718.

(92) Wang, Y.; Yu, G.; Rösner, M.; Katsnelson, M. I.; Lin, H.-Q.; Yuan, S. *Phys. Rev. X* **2022**, *12*, 021055.

(93) Sánchez-Castillo, A.; Román-Velázquez, C.; Noguez, C. *Phys. Rev. B* **2006**, *73*, 045401.

(94) Wei, X.; Tanaka, T.; Yomogida, Y.; Sato, N.; Saito, R.; Kataura, H. *Nat. Commun.* **2016**, *7*, 1–9.

(95) Yokoyama, A.; Yoshida, M.; Ishii, A.; Kato, Y. *Phys. Rev. X* **2014**, *4*, 011005.

(96) Mahlmeister, B.; Mahl, M.; Reichelt, H.; Shoyama, K.; Stolte, M.; Würthner, F. *J. Am. Chem. Soc.* **2022**, *144*, 10507–10514.

(97) Fan, W.; Matsuno, T.; Han, Y.; Wang, X.; Zhou, Q.; Isobe, H.; Wu, J. *J. Am. Chem. Soc.* **2021**, *143*, 15924–15929.

(98) Segawa, Y.; Watanabe, T.; Yamanoue, K.; Kuwayama, M.; Watanabe, K.; Pirillo, J.; Hijikata, Y.; Itami, K. *Nat. Synth.* **2022**, 1–7.

(99) Beugeling, W.; Quelle, A.; Smith, C. M. *Phys. Rev. B* **2014**, *89*, 235112.

(100) Flouris, K.; Jimenez, M. M.; Herrmann, H. J. *Phys. Rev. B* **2022**, *105*, 235122.

(101) Quelle, A.; Beugeling, W.; Smith, C. M. *Solid State Commun.* **2015**, *215*, 27–33.

(102) Wang, X.; Zheng, X.; Ni, M.; Zou, L.; Zeng, Z. *Appl. Phys. Lett.* **2010**, *97*, 123103.

(103) Güçlü, A. D.; Grabowski, M.; Hawrylak, P. *Phys. Rev. B* **2013**, *87*, 035435.

(104) Caetano, E. W.; Freire, V. N.; dos Santos, S. G.; Albuquerque, E.; Galvao, D. S.; Sato, F. *Langmuir* **2009**, *25*, 4751–4759.

(105) Giustino, F., *Materials modelling using density functional theory: properties and predictions*; Oxford University Press: 2014.

(106) Dirac, P. A. M. *Proceedings of the Royal Society of London. Series A, Containing Papers of a Mathematical and Physical Character* **1929**, *123*, 714–733.

(107) Perdew, J. P.; Burke, K.; Ernzerhof, M. *Physical Review Letters* **1996**, *77*, 3865.

(108) Chelikowsky, J. R.; Troullier, N.; Saad, Y. *Physical Review Letters* **1994**, *72*, 1240.

(109) Giannozzi, P. et al. *Journal of Physics: Condensed Matter* **2009**, *21*, 395502.

(110) Giannozzi, P. et al. *Journal of Physics: Condensed Matter* **2017**, *29*, 465901.

(111) Soler, J. M.; Artacho, E.; Gale, J. D.; García, A.; Junquera, J.; Ordejón, P.; Sánchez-Portal, D. *Journal of Physics: Condensed Matter* **2002**, *14*, 2745.

(112) Slater, J. C.; Koster, G. F. *Physical Review* **1954**, *94*, 1498.

(113) Pereira, V. M.; Neto, A. C.; Peres, N. *Physical Review B* **2009**, *80*, 045401.

(114) Tepliakov, N. V.; Lischner, J.; Kaxiras, E.; Mostofi, A. A.; Pizzochero, M. *Phys. Rev. Lett.* **2023**, *130*, 026401.

(115) Perdew, J. P.; Burke, K.; Ernzerhof, M. *Physical Review Letters* **1996**, *77*, 3865.

(116) Pizzi, G. et al. *J. Phys. Condens. Matter* **2020**, *32*, 165902.

(117) Gunlycke, D.; White, C. T. *Physical Review B* **2008**, *77*, 115116.

(118) Castro Neto, A. H.; Guinea, F.; Peres, N. M. R.; Novoselov, K. S.; Geim, A. K. *Review of Modern Physics* **2009**, *81*, 109.

(119) Fock, V. *Zeitschrift für Physik* **1935**, *98*, 145–154.

(120) Lemus, R.; Frank, A.; Andrés, M.; Leyvraz, F. *American Journal of Physics* **1998**, *66*, 629.

(121) Kalosakas, G.; Lathiotakis, N. N.; Papagelis, K. *Materials* **2021**, *14*, 5042.

(122) Li, Y.; Jiang, X.; Liu, Z.; Liu, Z. *Nano Research* **2010**, *3*, 545.

(123) Sun, L.; Li, Q.; Ren, H.; Su, H.; Shi, Q.; Yang, J. *The Journal of Chemical Physics* **2008**, *129*, 074704.

(124) Cao, T.; Zhao, F.; Louie, S. G. *Physical Review Letters* **2017**, *119*, 076401.

(125) López-Sancho, M. P.; Muñoz, M. C. *Physical Review B* **2021**, *104*, 245402.

(126) Rizzo, D. J.; Veber, G.; Cao, T.; Bronner, C.; Chen, T.; Zhao, F.; Rodriguez, H.; Louie, S. G.; Crommie, M. F.; Fischer, F. R. *Nature* **2018**, *560*, 204.

(127) Rizzo, D. J.; Jiang, J.; Joshi, D.; Veber, G.; Bronner, C.; Durr, R. A.; Jacobse, P. H.; Cao, T.; Kalayjian, A.; Rodriguez, H.; Butler, P.; Chen, T.; Louie, S. G.; Fischer, F. R.; Crommie, M. F. *ACS Nano* **2021**, *15*, 20633–20642.

(128) Gröning, O.; Wang, S.; Yao, X.; Pignedoli, C. A.; Borin Barin, G.; Daniels, C.; Cupo, A.; Meunier, V.; Feng, X.; Narita, A., et al. *Nature* **2018**, *560*, 209.

(129) Lawrence, J.; Brandimarte, P.; Berdonces-Layunta, A.; Mohammed, M. S. G.; Grewal, A.; Leon, C. C.; Sánchez-Portal, D.; de Oteyza, D. G. *ACS Nano* **2020**, *14*, 4499.

(130) Jones, R. O. *Review of Modern Physics* **2015**, *87*, 897.

(131) Perdew, J. P.; Wang, Y. *Physical Review B* **1992**, *45*, 13244.

(132) Ceperley, D. M.; Alder, B. J. *Physical Review Letters* **1980**, *45*, 566.

(133) Perdew, J. P.; Zunger, A. *Physical Review B* **1981**, *23*, 5048.

(134) Pizzochero, M.; Tepliakov, N. V.; Mostofi, A. A.; Kaxiras, E. *Nano Letters* **2021**, *21*, 9332.

(135) Troullier, N.; Martins, J. L. *Physical Review B* **1991**, *43*, 1993.

(136) Son, Y.-W.; Cohen, M. L.; Louie, S. G. *Nature* **2006**, *444*, 347.

(137) Kundu, R. *Modern Physics Letters B* **2011**, *25*, 163.

(138) Pizzochero, M.; Čerņevičs, K.; Borin Barin, G.; Wang, S.; Ruffieux, P.; Fasel, R.; Yazyev, O. V. *2D Materials* **2021**, *8*, 035025.

(139) Panighel, M.; Quiroga, S.; Brandimarte, P.; Moreno, C.; Garcia-Lekue, A.; Vilas-Varela, M.; Rey, D.; Sauthier, G.; Ceballos, G.; Peña, D.; Mugarza, A. *ACS Nano* **2020**, *14*, 11120.

(140) Tan, Y.-Z.; Yang, B.; Parvez, K.; Narita, A.; Osella, S.; Beljonne, D.; Feng, X.; Müllen, K. *Nature Communications* **2013**, *4*, 2646.

(141) Le Lay, G.; Aufray, B.; Léandri, C.; Oughaddou, H.; Biberian, J.-P.; De Padova, P.; Dávila, M.; Ealet, B.; Kara, A. *Applied Surface Science* **2009**, *256*, 524.

(142) Padova, P. D.; Perfetti, P.; Olivieri, B.; Quaresima, C.; Ottaviani, C.; Lay, G. L. *Journal of Physics: Condensed Matter* **2012**, *24*, 223001.

(143) De Padova, P.; Quaresima, C.; Perfetti, P.; Olivieri, B.; Leandri, C.; Aufray, B.; Vizzini, S.; Le Lay, G. *Nano Letters* **2008**, *8*, 271.

(144) De Padova, P.; Kubo, O.; Olivieri, B.; Quaresima, C.; Nakayama, T.; Aono, M.; Le Lay, G. *Nano Letters* **2012**, *12*, 5500.

(145) Yuhara, J.; Shimazu, H.; Kobayashi, M.; Ohta, A.; Miyazaki, S.; Takakura, S.-i.; Nakatake, M.; Le Lay, G. *Applied Surface Science* **2021**, *550*, 149236.

(146) Hiraoka, R.; Lin, C.-L.; Nakamura, K.; Nagao, R.; Kawai, M.; Arafune, R.; Takagi, N. *Beilstein Journal of Nanotechnology* **2017**, *8*, 1699.

(147) Tao, L.; Cinquanta, E.; Chiappe, D.; Grazianetti, C.; Fanciulli, M.; Dubey, M.; Molle, A.; Akinwande, D. *Nature Nanotechnology* **2015**, *10*, 227.

(148) Pizzochero, M.; Bonfanti, M.; Martinazzo, R. *Physical Chemistry Chemical Physics* **2019**, *21*, 26342.

(149) Cappelletti, M.; Leccese, M.; Cococcioni, M.; Proserpio, D. M.; Martinazzo, R. *Molecules* **2021**, *26*, 3805.

(150) Yano, Y.; Mitoma, N.; Ito, H.; Itami, K. *The Journal of Organic Chemistry* **2020**, *85*, 4.

(151) Cai, J.; Pignedoli, C. A.; Talirz, L.; Ruffieux, P.; Söde, H.; Liang, L.; Meunier, V.; Berger, R.; Li, R.; Feng, X.; Müllen, K.; Fasel, R. *Nature Nanotechnology* **2014**, *9*, 896–900.

(152) Zhang, Y.; Zhang, Y.; Li, G.; Lu, J.; Lin, X.; Du, S.; Berger, R.; Feng, X.; Müllen, K.; Gao, H.-J. *Applied Physics Letters* **2014**, *105*, 023101.

(153) Kawai, S.; Saito, S.; Osumi, S.; Yamaguchi, S.; Foster, A. S.; Spijker, P.; Meyer, E. *Nature Communications* **2015**, *6*, 8098.

(154) Cloke, R. R.; Marangoni, T.; Nguyen, G. D.; Joshi, T.; Rizzo, D. J.; Bronner, C.; Cao, T.; Louie, S. G.; Crommie, M. F.; Fischer, F. R. *Journal of the American Chemical Society* **2015**, *137*, 8872.

(155) Kawai, S.; Nakatsuka, S.; Hatakeyama, T.; Pawlak, R.; Meier, T.; Tracey, J.; Meyer, E.; Foster, A. S. *Science Advances* **2018**, *4*, 7181.

(156) Tang, W.; Sanville, E.; Henkelman, G. *Journal of Physics: Condensed Matter* **2009**, *21*, 084204.

(157) Tepliakov, N. V.; Ma, R.; Lischner, J.; Kaxiras, E.; Mostofi, A. A.; Pizzochero, M. *Nano Letters* **2023**, *23*, 6698–6704.

(158) Lieb, E. H. *Physical Review Letters* **1989**, *62*, 1201.

(159) Zhang, Y.; Yang, W. *Physical Review Letters* **1998**, *80*, 890.

(160) Becke, A. D. *Physical Review A* **1988**, *38*, 3098.

(161) Lee, C.; Yang, W.; Parr, R. G. *Physical Review B* **1988**, *37*, 785.

(162) Miehlich, B.; Savin, A.; Stoll, H.; Preuss, H. *Chemical Physics Letters* **1989**, *157*, 200.

(163) Wu, Z.; Cohen, R. E. *Physical Review B* **2006**, *73*, 235116.

(164) Geim, A. K.; Grigorieva, I. V. *Nature* **2013**, *499*, 419–425.

(165) De Groot, R. A.; Mueller, F. M.; Engen, P. G. v.; Buschow, K. H. J. *Physical Review Letters* **1983**, *50*, 2024.

(166) Hu, X. *Advanced Materials* **2012**, *24*, 294–298.

(167) Soriano, D.; Fernández-Rossier, J. *Physical Review B* **2012**, *85*, 195433.

(168) Pizzochero, M.; Leenaerts, O.; Partoens, B.; Martinazzo, R.; Peeters, F. M. *Journal of Physics: Condensed Matter* **2015**, *27*, 425502.

(169) Raza, H.; Kan, E. C. *Physical Review B* **2008**, *77*, 245434.

(170) Roslyak, O.; Gumbs, G.; Huang, D. *Philosophical Transactions of the Royal Society A: Mathematical, Physical and Engineering Sciences* **2010**, *368*, 5431.

(171) Yazyev, O. V.; Katsnelson, M. I. *Physical Review Letters* **2008**, *100*, 047209.

(172) Pisani, L.; Chan, J. A.; Montanari, B.; Harrison, N. M. *Physical Review B* **2007**, *75*, 064418.

(173) Thomann, H.; Dalton, L. K.; Grabowski, M.; Clarke, T. C. *Physical Review B* **1985**, *31*, 3141.

(174) Pizzochero, M.; Tepliakov, N. V.; Lischner, J.; Mostofi, A. A.; Kaxiras, E. *Nano Letters* **2024**, *24*, 6521–6528.

(175) Zhang, Y.; Feng, X.; Zheng, Z.; Zhang, Z.; Lin, K.; Sun, X.; Wang, G.; Wang, J.; Wei, J.; Vallobra, P., et al. *Applied Physics Reviews* **2023**, *10*, 011301.

(176) Razzhivina, M. E.; Rukhlenko, I. D.; Tepliakov, N. V. *The Journal of Physical Chemistry Letters* **2023**, *14*, 4426–4432.

(177) Baimuratov, A. S.; Tepliakov, N. V.; Gun'Ko, Y. K.; Shalkovskiy, A. G.; Baranov, A. V.; Fedorov, A. V.; Rukhlenko, I. D. *Chirality* **2017**, *29*, 159–166.

(178) Rukhlenko, I. D.; Tepliakov, N. V.; Baimuratov, A. S.; Andronaki, S. A.; Gun'ko, Y. K.; Baranov, A. V.; Fedorov, A. V. *Sci. Rep.* **2016**, *6*, 1–8.

(179) Mazzeo, G.; Ghidinelli, S.; Ruzziconi, R.; Grandi, M.; Abbate, S.; Longhi, G. *ChemPhotoChem* **2022**, *6*, e202100222.

(180) Tepliakov, N. V.; Baimuratov, A. S.; Baranov, A. V.; Fedorov, A. V.; Rukhlenko, I. D. *J. Appl. Phys.* **2016**, *119*, 194302.

(181) Guo, Z.; Gong, Z.; Dong, H.; Sun, C. *Physical Review B* **2009**, *80*, 195310.

(182) Tepliakov, N. V.; Vovk, I. A.; Shlykov, A. I.; Leonov, M. Y.; Baranov, A. V.; Fedorov, A. V.; Rukhlenko, I. D. *J. Phys. Chem. C* **2019**, *123*, 2658–2664.

(183) Wakabayashi, M.; Yokojima, S.; Fukaminato, T.; Shiino, K.-i.; Irie, M.; Nakamura, S. *J. Phys. Chem. A* **2014**, *118*, 5046–5057.

(184) Fukunaga, T. M.; Sawabe, C.; Matsuno, T.; Takeya, J.; Okamoto, T.; Isobe, H. *Angew. Chem. Int. Ed.* **2021**, *60*, 19097–19101.